Development of Integrated Electronics for Readout of High Frequency Micro/Nano-mechanical Resonator

Tang, Meng

Publication date:
2011

Document Version
Publisher's PDF, also known as Version of record

Development of Integrated Electronics for Readout of High Frequency Micro/Nano-mechanical Resonator

Meng Tang

Institut for Mikro- og Nanoteknologi

Danmarks Tekniske Universitet

A thesis submitted for the degree of

Doctor of Philosophy

January 2011

I would like to dedicate this thesis to my loving Zhimi. I hope one day he will read it and enjoy himself.

Acknowledgements

This thesis has been written as a partial fulfillment of the requirements for obtaining the Ph.D-degree at the Technical Iniversity of Denmark (DTU). The Ph.D project has been carried out at DTU Nanotechnology in the period from the 1st of May 2007 to the 7th of January 2011.

This Ph.D project has been conducted in the DyNEMS group in the NanoSystems Engineering (NSE) division supervised by:

Associate Professor
Zachary James Davis

This work has been funded by the Danish Research Council for Technology and Production (FTP).

First and foremost I would like to thank Zach for offering me the opportunity to join this fantastic MEMS field from a total electronic background. Zach's patient instruction and ever optimistic attitude has been greatly inspiring.

Secondly I also would like to thank Professor Anja Boisen. Anja creates a fun and inspiring work environment with all professional and passionate members in her Nanoprobes group.

I am thankful for Jan Hales and Alberto Cagliani. Their hard work in cleanroom is a great support of this Ph.D work.

I also would like to thank Prof. G. Abadal from University Automatic Barcelona for his support and instruction with the fantastic lab equipment there.

Prof. Xinxin Li and Lin He hosted my five months stay in the Shanghai Institute of Microsystems and Information Technology, Chinese

Society of Academy, where I got the great opportunity to experience a different research environment and to work with these interesting people.

I am thankful for the various support from the scientist and students at DTU Nanotech and DANCHIP.

I am deeply grateful for the support from family and friends.

Kongens Lyngby, January 7. 2011

Meng Tang
Department of Micro- and Nanotechnology
Technical University of Denmark
2800 Kongens Lyngby
Denmark

Abstract

Micro sized bulk type resonators have been developed through the last five years for application within the electronics industry for cheap low power and integratable alternative for both passive and active components. However, this type of bulk resonator can also be applicable for bio/chemical sensors where due to the minute size and mass of the resonators, small amounts of absorbed mass can be detected. A bulk disk resonator working in a dynamic in-plane mode is used for mass detection. In this case the MEMS resonator is vibrating close to its resonant frequency and any mass absorbed or deposited on the surface induces a frequency shift due to the mass change. Bulk resonators have demonstrated a high resolution and areal resolution compared with other popular mass sensor devices, and was thus the focus in this Ph.D work.

After analyzing the mechanical and electrical behavior of the bulk resonators, a full electrical model was deduced for further design and simulation. The model is a motional model with series resistance inductance and capacitance (RLC) paralleled with an extra parallel capacitor. The parallel capacitor brings in the deviation of measured resonant frequency and also introduces more frequency noise. Therefore, compensation techniques were used to cancel the effect of the parallel capacitor. Two interesting compensation techniques were conducted, the tuneable capacitor and the identical devices pair. Both compensation methods proved to experimentally decrease the frequency noise.

This thesis work also introduced a novel measurement technique called the pulse mode, where the resonator device was not excited continuously such as in a traditional frequency sweep measurement, instead,

the resonator is excited for a short time and afterwards set into free vibrating around its resonant frequency. Its capability of measuring the resonant frequency, Q-factor and feedthrough/parasitic capacitor at the same time is verified both theoretically and experimentally in air at a high speed. Furthermore, excitation of the devices does not need any complicated form of feedback. This technique shows a great potential for mass sensing in liquid mediums where measuring several parameters will have a huge impact. Initial experiments were also conducted for humidity sensing. The disk resonator showed a high sensitivity and a future possibility for real application.

In order to facilitate the integration of the MEMS resonator and the readout electronics, an active filter tuned oscillator circuitry was designed and simulated with CMOS 0.18 μm technology. The behavior of the circuitry was verified with Labview simulink. However due to the short time, the PhD work didn't include the total physical layout, fabrication or testing of the chip. This work will be followed by cooperative partners.

Dansk Resumé

Micro strrelse bulk type resonatorer er blevet udviklet gennem de sidste fem r til anvendelse inden for elektronikbranchen til lav strm og billige alternativer til bde passive og aktive komponenter. Dog kan denne type bulk resonator ogs bruges til bio / kemiske sensorer hvor, da p grund af den minut strrelse og masse af resonatorer, kan sm mngder af absorberet masse blive detekteret. En bulk resonator, der arbejder i en dynamisk in-plane vibrations tilstand bruges til masse detektion. I dette tilflde vibrere MEMS resonatoren tt p sin resonansfrekvens og eventuelle masse absorberes eller deponeres p overfladen og inducerer en frekvens skift p grund af masse ndringer. Bulk resonatorer har vist en hj masse oplsning og arealoplsning sammenlignet med andre populre massemler enheder, og var dermed i fokus i denne Ph.D arbejde.

Efter at have analyseret de mekaniske og elektriske opfrsel af den bulk resonatorer, var en fuld elektrisk model udledte for yderligere design og simulation. Modellen er baseret p en elektrisk model med serie modstand induktans og kapacitans (RLC) i parallel med en ekstra parallel kondensator. Igennem analysen ser vi at den parallelle kondensator bringer afvigelse af mlteresonans frekvens og ogs indfrer mere stj. Derfor blev kompensations teknikker, der anvendes til at annullere effekten af den parallelle kondensator undersgt. To interessante kompensation teknikker blev udfrt, tuneable kondensator og den identiske par. Begge kompensationen metoder vist sig at eksperimentelt mindske frekvensstjen.

Denne afhandling har ogs indfrt en ny mlemetode kaldet "pulsed mode", hvor resonator enheden ikke bliver eksiteret kontinuert som i

en traditionel frekvens sweep mling, men i stedet bliver resonatoren eksisteret for en kort tid og derefter forladt i fri bevgelser omkring sin resonansfrekven. Metodens evne til at mle resonans frekvens, Q-faktor og den parallel kondensator p samme tid er verificeret bde teoretisk og eksperimentelt i luft ved hj hastighed. Hertil kommer, at metoden ikke har brug for nogen kompliceret form for feedback som gre den meget letter at indfr i forhold til andre metoder og derfor viser denne teknik et stort potentiale for masse mlinger i flydende medier, hvor en simple metode for mling flere parametre vil have en enorm indflydelse. Indledende fugtigheds mlinger blev ogs udfrt og det viste sig at den bulk disk resonatoren har en hj flsomhed og en fremtidig mulighed for reel anvendelse.

For at lette integrationen af MEMS resonatoren sammen med udlsning elektronik, var en aktiv filterindstillet oscillator kredslb designet og simuleret med CMOS $0.18\mu m$teknologi. Opfrslen af kredslb blev efterprvet med LabVIEW Simulink. Men p grund af for korte tid, er den samlede fysiske indretning, fabrikation eller afprvning af chippen ikke blevet net. Dette arbejde vil blive fulgt op af samarbejdspartnere.

Contents

List of Figures

Chapter 1

Introduction

1.1 Motivation

Micro Electro Mechanical Systems(MEMS) was theoretically predicted in 1959 by Richard Feynman [1]. Decades of research within semiconductor device fabrication technologies finally realized the first MEMS pressure sensor by IBM in 1970s. Nowadays, new MEMS technologies (and even Nano Electro Mechanical Systems (NEMS) [2] are being developed every day. Compared to the similar fabrication technology such as Integrated Circuitry (IC), MEMS processing is more complicated due to its combination of mechanical features. However, these mechanical features in turn introduce extensive applications: sensor [3], actuators [4], accelerometers [5], switches [6] and so on.

As the most popular application, MEMS sensors can cover a very wide scope such as temperature, humility, pressure, flow, motion and so on. In addition, with appropriate chemical functionalization, they can also be employed for detection of different chemical entities such as CO, CO_2, alcohols, explosion or biological entities such as antibody, bacteria, enzyme. One of the outstanding advantages of the MEMS bio/chemical sensors is that they can detect sufficiently low quantities of bio/chemical species which can lead to early detection of disease [7, 8]. As a result, current research in this field is focused on maximizing the detection sensitivity [9, 10].

This Ph.D project is one part of the project 'high frequency resonators for

liquid based bio/chemical diagnostics and monitoring application', which is committed to the MEMS sensing applications, in particular mass sensing. The goal of the whole project is to develop a bulk mode, high frequency, mechanical resonator based high sensitivity sensor for bio/chemical detection in air and eventually aqueous environments . The main principle of the sensor is to measure the mass changes of the resonator due to absorption of bio/chemical species.Other Ph.D projects are responsible for fabrication of the MEMS device while this Ph.D thesis is focused on the high frequency electrical readout for the sensor.

1.2 Mass Sensors

Various resonant mass sensors have been commercially utilized for decades and novel technologies continue the grow of this family. Normally, the resolution (Δm) or areal resolution ($\frac{\Delta m}{Area}$) are usually selected to evaluate the efficiency of different mass sensors. Below, commonly applied mass sensors are introduced and their performances are compared afterwards.

1.2.1 QCM

Quartz Crystal Microbalance (QCM) as shown in Fig.(1.1)introduced by Saurbrey [11] in 1959, has been commonly implemented in mass sensing [12, 13]. QCM is a Bulk Acoustic Wave (BAW) resonator composed of piezoelectric AT-cut [14] quarts crystal sandwiches between a pair of electrodes. The advantage is that it has nearly zero frequency drift with temperature around room temperature [15]. The resonant frequency is normally below 100 MHz with high Quality(Q) factor (up to 10000). In order to improve the resolution, the thickness of QCM has to be decreased, however, this will make the QCM devices fragile and furthermore the electrodes will then constitute a large part of the effective mass thus will largely impair the resolution [16].

1.2.2 FBAR

The development of micro fabrication has enabled the fabrication of the piezoelectric layer between the two metal electrodes as thin as 1 μm shown in Fig.(1.2).

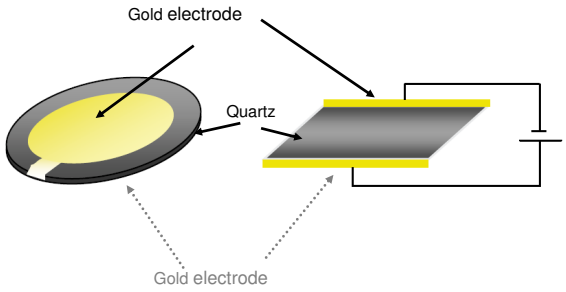

Figure 1.1: Schematic drawing of a QCM (a) top view (b) cross sectional view from products of the company Qsense. The top and bottom gold electrodes are placed on a piezoelectric material and applied a drive. The most commonly used piezoelectric material for QCM is single crystalline quartz.

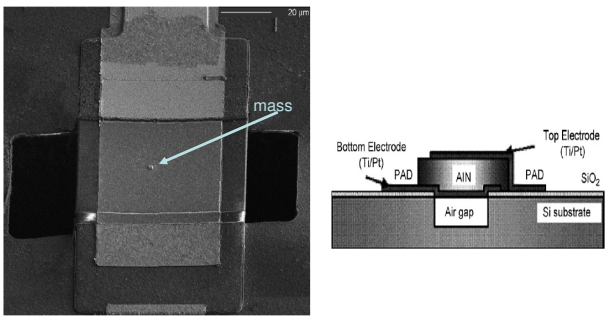

Figure 1.2: Schematic drawing of the (a) top view (b) cross sectional view of FBAR [17]. In this specific case the membrane is 1 μm thick with a surface area of 50 $\times$ 70 μm^2, giving a sensitivity of 10 ag/Hz.

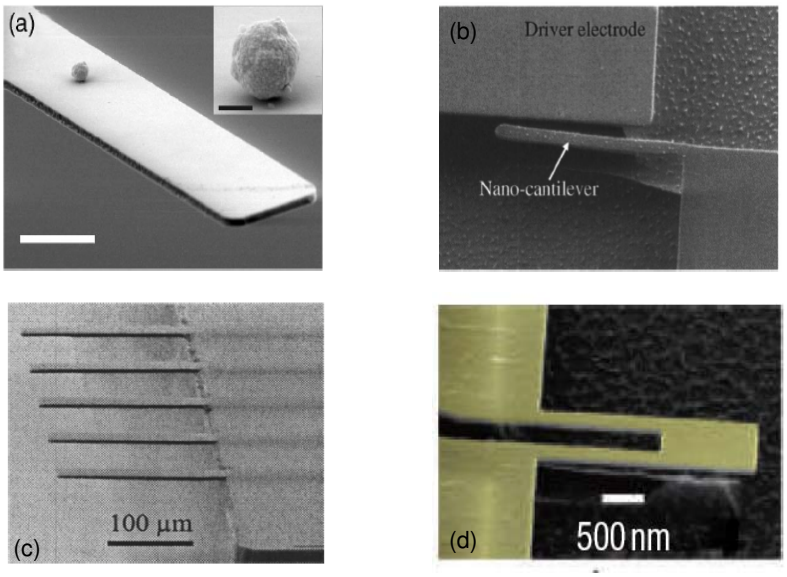

Figure 1.3: Scanning Electron Microscopy (SEM) image of typical MEMS mass sensors (a) micro cantilever with gold particle on top [19] (b) Aluminum nano cantilever using UV lithography technique with lateral and vertical dimensions under 100 *nm* [20] (c) micro cantilever array fabricated in the polymer SU-8 [21] (d) nano cantilever with very high frequency more than 100 MHz and a mass resolution less than 1 attogram [22].

This new device called Thin-film acoustic resonators (FBARs) are able to acquire resonant frequency roughly from 100 MHz up to 10 GHz. Therefore,they are more popular in RF and wireless communication application. FBAR have demonstrated a much higher areal resolution [17] (up to three order of magnitude) than that of QCM. However, the Q factor of FBAR is very low (< 1000 in air), therefore the resolution is not superior [18] to QCM.

1.2.3 Cantilever

Cantilever mass sensors shown in Fig.(1.3) can be categorized according to their operation modes, referred to as static and dynamic mode. In the static mode the cantilever detects the surface stress change induced by the immobilized molecules. The static mode sensor is a more mature technology, however the main disadvantage with this techniques is its dependence on strong molecular interaction to induce surface stress. Therefore, the alternative dynamic mode operation has been more and more explored. In this mode the cantilever is vibrating close to its resonant frequency and detects the resonant frequency shift due to the mass change induced by the mass absorbed or deposited on the surface.

The cantilever structure is proper for extreme miniaturization due to it simple geometry and mass resolutions in the attogram regime have been achieved in air [23, 24, 25, 26] at a resonant frequency of up to $100MHz$. The significant disadvantage of cantilever mass sensors is they have a spatially non-uniform mass sensitivity [19]. The mass sensitivity is at its maximum when the added mass is placed at the free end of the cantilever while the sensitivity is zero when the added mass is placed to the fixed end of the cantilever. Therefore, if the cantilever sensor is exploited for detecting small amounts of target particles, not enough to generate a uniform distribution of particles on the cantilever, complex methods are needed to locate the mass loading [27, 28]. In addition, improving the mass resolution of cantilever requires a scaling down the cantilever dimension which will contribute to an even smaller sensing area thus impairing the areal resolution.

1.2.4 In Plane Bulk Resonator

In bulk resonator the acoustic wave is propagating in the bulk rather than the surface (SAW–Surface Acoustics Wave). QCM and FBAR are also bulk resonator, and the only special point is they use the piezoelectric material as bulk layer. The other three interesting bulk resonators are Bulk Disk Resonator (BDR) as shown in Fig.(1.4(a)) , Bulk Rectangular Resonator shown in Fig.(1.4(b)) and Longitudinal Bulk Acoustic Resonator (LBAR) shown in Fig.(1.4(c)). The resonators have an in-plane mode motion in contrary to out of plane flexural mode such as cantilever, expanding and contracting around its resonant frequency. Any mass

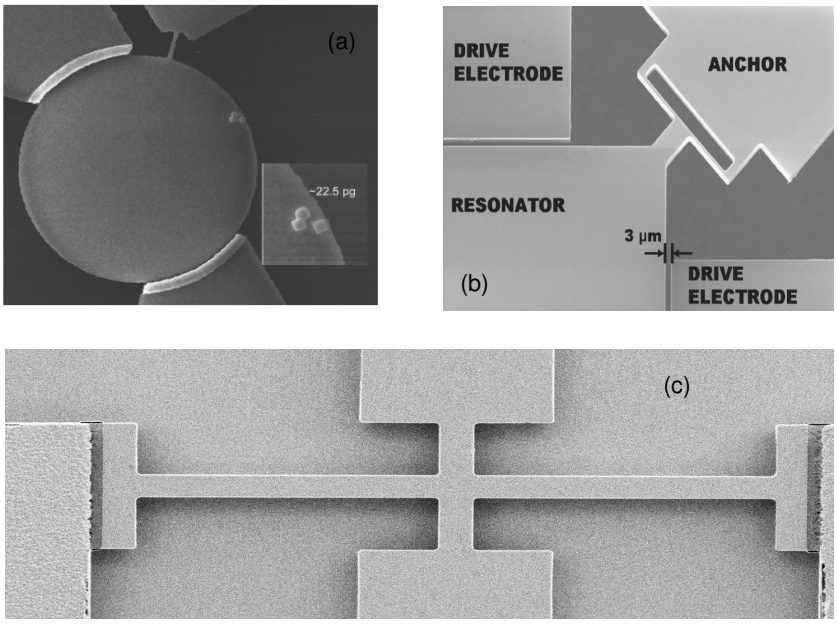

Figure 1.4: SEM image of (a) Bulk disk resonator with one anchor and two electrodes, with Pt/C/Ga composite deposited at the edge. The disk diameter 60 μm [29]. (b) one of the corner of the bulk rectangular resonator, showing the T anchors tow of the four drive electrodes located on each side of the resonator. The length of each side of rectangular resonator is 2 mm [30]. (c)longitudinal bulk acoustic cantilever resonator with anchoring at the beam center, with length 30 μm and width 2.5 μm[31].

	f MHz	Q	Δm g	$\frac{\Delta m}{Area}$ g/cm^2
QCM [15, 16]	< 100	10000	$10f$	$10f$
FBAR [18]	790	$100 - 150$	$1f$	$0.1p$
NanoCan [26]	190	5000	$30z$	$12p$
BDR [29, 35]	68	4000	$0.7a$	$0.2p$
BRR [30]	2	15000	$4p$	$100p$
LBAR [31]	51	3000	$0.5a$	$0.6p$

Table 1.1: Resolution and areal resolution of different MEMS devices. QCM is a relatively mature technique and succeed in commercialization, therefore the given value of QCM is from typical product measured in air. The given value of FBAR is the state of the art measurement results from liquid environment. The given value of Nano Cantilever is conducted in vacuum. Due to the limit of literature for liquid application of the rest devices,the given value of BDR/BRR/LBAR are the state of the art measurement results in air.

load on the surface of the resonator will induce a total mass change and therefore the resonant frequency change. The bulk disk resonant frequency scales inversely with its radius, yielding a resonant frequency from 10 MHz to 10 GHz with $Q-$factor up to 10^5 [32, 33, 34]. The bulk rectangular resonator is quite similar with bulk disk resonator but with the rectangular shape. LBAR is even more simple. This device consists of two suspended cantilevers anchored in the middle by the thin arms to the rigid support structure [35]. The device is operating in a longitudinal extensional mode, where the two cantilevers are moving in an in-plane anti phase motion.

Table.(1.1) lists the important features of different mass sensor technologies. Compared to QCM, FBAR and BRR, bulk disk resonator and LBAR provide a much smaller resolution, more than three order of magnitude. Although Nano Cantilever is able to supply an even smaller value in resolution, it is not competitive in resolution per area, since it has a nano-scale sensing area. LBAR is still beam shape and thus has a low sensing area compared to the disk shape. Therefore we are especially interested in the bulk disk resonator. As a summary, the advantages of bulk disk resonators and LBAR are they can supply the comparable high sensitivity and mass resolution as compared to cantilever and meanwhile maintain a relatively larger area. Therefore, they can provide a high areal mass

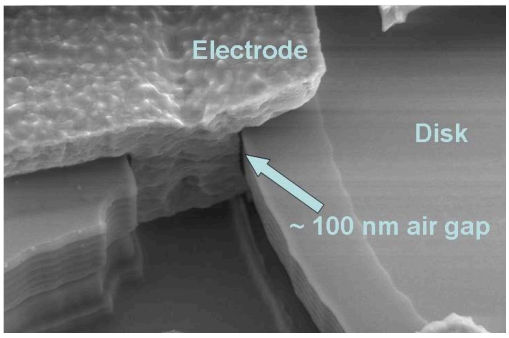

Figure 1.5: SEM image of the capacitive readout with a narrow gap separating the disk and the electrodes and defining the electro-mechanical transduction [35].

resolution. In addition, the in-plane mode rather than the flexural type as with cantilever is independent on the location of the mass loading. All these features suggest the bulk disk resonator a suitable candidate for mass sensing applications. The detailed analysis will be given in Chapter 2. This thesis worked mainly on these two types of device LBAR and bulk disk resonator.

1.3 Readout Technology

Below we analyze the commonly used readout technologies for bulk resonator applications.

1.3.1 Capacitive Readout

The capacitive readout requires extra electrodes that surround the resonator sensor to form the pair of conductors separated by a gap(insulator)– capacitor as shown in Fig.(1.5). This method is based on measuring the changes of the capacitance induced by the change of gap distance which is the result of resonator vibration [33]. The detailed analysis will be given in the following chapters. The

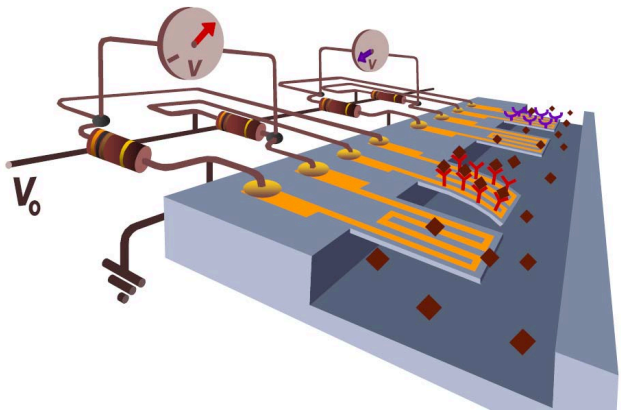

Figure 1.6: A schematic image of a micro mechanical sensor showing the integrated piezoresisitive readout with the Au resistor on top.[40]

disadvantage of this method is the capacitive change is very small therefore the current change it generates is also very limited. The challenges rely on the readout circuitry to measure the tiny capacitive current.

1.3.2 Piezoresistive Readout

Apart from the capacitive readout, the mechanical motion of the resonator can also be detected through the piezoresistive effect of piezoresisitive layer on top of the sensor Fig.(1.6)[36, 37, 38, 39]. This layer exhibits remarkable piezoresisitive response which generates a resistive change caused by any stress change due to the surface bending. The disadvantage of this technique is that the current flowing through the surface will result in an additional dissipation of heat and associated to thermal drifts.

1.3.3 Piezoelectric Readout

The piezoelectric effect is defined as the appearance of an electric potential across certain faces of a crystal when it is subjected to mechanical deformation. It is

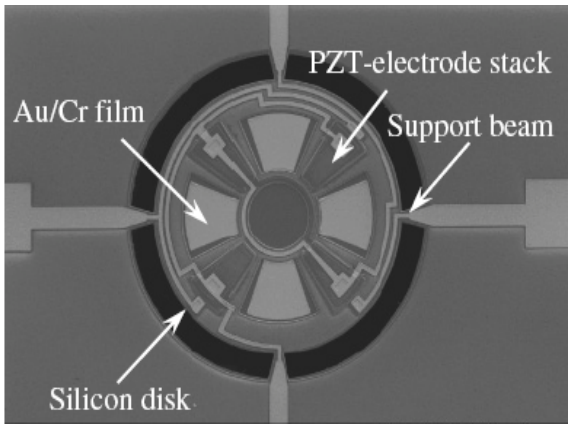

Figure 1.7: SEM image of the disk resonator with integrated piezoelectric PZT-electrode stack [41].

quite similar to the piezoresistive readout, the difference is it generates electricity rather than resistance. J.Lu et al. succeeded in the piezoelectric readout on a bulk disk resonator as shown in Fig.(1.7). This technical also has the problem of energy dissipation on the surface and requires additional consideration to minimize. The technology is also more complicated in fabrication.

As a conclusion, all of the three techniques are good candidates for disk resonator. This thesis only focused on the capacitive readout since it is a simple and mature technique and has been successfully implemented in our group for years, while the other two techniques require extra processing of the resonator, therefore will be interesting in future research.

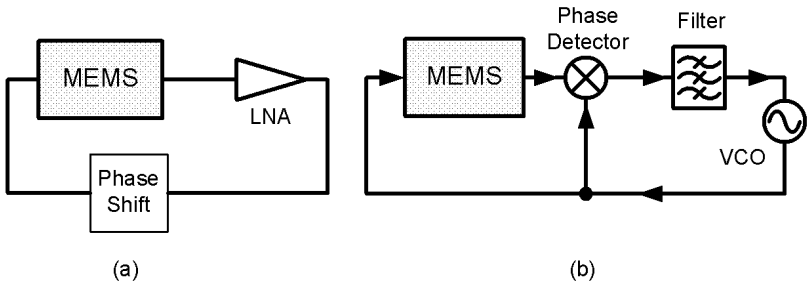

Figure 1.8: (a)Self-sustain oscillator circuitry (b)Phase locked loop circuitry.

1.4 Readout Circuitry

Theoretical calculations of the resonant frequency f_0 is:

$$f_0 = \frac{1}{2\pi}\sqrt{\frac{k}{m}} \tag{1.1}$$

where m is the effective mass and k is the effective stiffness (detailed modeling will be illustrated in Chapter 2. The minimum detectable mass is [42]:

$$\delta m \approx -\frac{2m}{f_0}\delta f. \tag{1.2}$$

where δf is the minimal detectable frequency and is determined by the resolution of the readout electronics. Thus it is important to look at current methods of measuring the resonant frequency of resonant sensors.

1.4.1 Oscillator

The most common readout circuitry resorts to the self-sustained oscillator circuitry as shown in Fig.(1.8(a)). In motion, the mechanical resonator produces a motional current (induce by capacitive change) at one electrode. This current is sensed and fed back to the other electrode to generate an electrostatic force. The gain (unity) and phase (360°) criterion [43] are satisfied by the amplifier and phase shift block. Stable mechanical vibration of the MEMs element can be achieved and maintained with DC power supply to the loop circuit [44].

M.L.Roukes's and C T.-C. Nguyen's groups succeed in realization of the MEMS/NEMS based oscillator circuitry [45, 46, 47]. From 2004, Nguyen's group started to work on the disk resonator based reference oscillator [48, 49, 50].The disadvantage of oscillator circuitry is the measured frequency is sensitive to temperature and power supply variation. However, the oscillator circuitry is relatively simple compared to the other solution such as phase locked loop, and therefore is still widely used. In this Ph.D thesis, we also focused some energy on the oscillator circuitry as a start for our sensor. The challenge is to amplify the weak current at high frequency from mechanical device and meanwhile to eliminate the influence of parallel capacitive noise.

1.4.2 Phase Locked Loop

Another popular frequency tracking circuitry with low phase noise is the phase locked loop shown as in Fig.(1.8(b)). It mainly consists of a Voltage Control Oscillator (VCO), Filter and a Phase Detector. The generated sinusoidal signal from the output of VCO drives the MEMS resonator and produces an output with a phase shift due to the mismatch of the VCO frequency and the MEMS resonant frequency. The phase shift is detected by the subtraction of the MEMS output and the original VCO output. After the filter, the output voltage proportional to the phase shift in turn determines the output frequency of the VCO. Thus, at positive phase shift, the circuit automatically tunes the frequency of VCO to a lower value while at negative phase shift, tunes to a higher value of frequency of VCO. Until finally, the output frequency of the VCO and the resonant frequency are the same (synchronization in phase), the close loop is then locked and produce

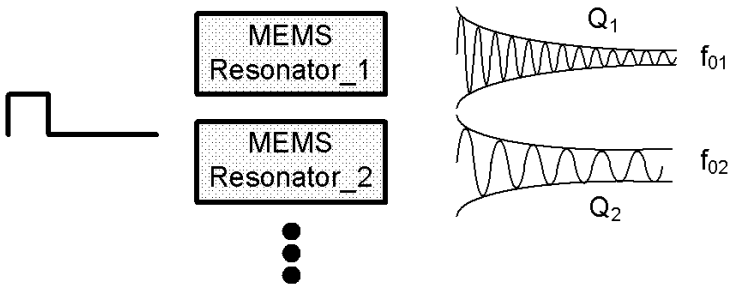

Figure 1.9: Pulse mode excitation and transient analysis of output frequency and Q factor.

a stable output frequency from the VCO [51].The PLL circuit normally exhibits a low phase noise and thus stable frequency output.

However, using a feedback loop in general employs complex circuitry, which is a great challenge to achieve for bulk mode resonators with high frequency and large motional impedance. Furthermore, an Oscillator or PLL can only measure the fundamental frequency of a single resonator at one time.

1.4.3 Pulse Mode

In order to circumvent these short comings, an alternative choice is a straight forward non loop readout mechanism based on pulsed excitation and transient analysis as shown in Fig.(1.9). The merits are:

- The resonant frequency, damping time constant (Q-factor) and parallel capacitance can be monitored simultaneously and at a high speed (less than 1s), giving more information about the sensors environment;

	Complexity	Frequency Stability	Measures Parameter
Oscillator	medium	medium	f_0
PLL	complex	high	f_0
Pulse	simple	low	f_0, Q, C

Table 1.2: Comparison of the advantages and disadvantages of the three readout circuitry.

- The approach is flexible and no complicated loop circuitry is required;
- A single pulse stimuli is able to drive multiple sensors with different resonant frequencies simultaneously without introducing extra loops. This is interesting for mass sensing because the reference resonator and the sensing resonator can be excited by a unique signal.

M. Rodahl et. al. have succeeded applying the pulse excitation on QCM devices [52, 53]. However, disk resonator has a much higher resonant frequency (up to $66MHz$) and much lower output current (down to $1\mu A$), which largely increases the difficulty to implement the method. In this Ph.D thesis, we introduce and demonstrate measurements with sinusoidal burst pulse excitation for a bulk disk resonator.

Table. (1.2) lists the advantages and disadvantages of the three readout methods. The most outstanding feature of pulse mode is its capability of measuring simultaneously the resonant frequency, the Q factor and the parallel capacitor while the oscillator and PLL circuitry can only measure the resonant frequency. However, the pulse mode method has a relatively high frequency noise compared to the other two. Not taking the circuitry complexity, the ideal solution is to use either the oscillator or PLL circuitry to measure the resonant frequency first and then open the loop to conduct the pulse mode method. The detailed the introduction and design will be in chapter 5.

1.5 Thesis Overview

The rest of the thesis is outlined as follow:

- **Chapter 2 - MEMS Theory:** Here we describe the basic structure of

the MEMS bulk disk resonator and longitudinal bulk acoustic cantilever and detailed illustrate their working mechanics, respectively. There is an analysis of the different motional modes and the equivalent mechanical and electrical model are presented. Finally the excitation mechanism is also characterized.

- **Chapter 3 - Measurement Theory:** Four fundamental measurement configurations and their corresponding equivalent electrical motional models are discribed. An additional focus is required on the extra parallel capacitor upon the motional model. The source and the influence of the particular parallel capacitor are analyzed. The compensation technique of parallel capacitor is demonstrated and the independence of pulse mode measurement on the parallel capacitor is highlighted. Finally, comparison of various popular pulse signals are described.

- **Chapter 4 - Measurement** The measurement setup for both frequency sweep and pulse mode time transient response are demonstrated. Compensated results with both tunable capacitor and identical resonator pair are presented. Through pulse mode, measured resonant frequency, Q factor and the parallel capacitor are listed. A Labview programme with real time measurement function has been implemented. Finally, measured results with humidity variation based on the pulse configuration are demonstrated.

- **Chapter 5 Integrated Oscillator** An integrated oscillator circuitry based on the bulk disk resonator is designed with CMOS $0.18\mu m$ technology. It is composed with a low noise differential amplifier, parallel capacitor compensation block and a hysteresis comparator. Detailed analysis and computation are conducted on the Barkhausen's oscillation criterion. Simulation results with Cadence and verification of by Matlab simulink are demonstrated. Finally the physical layout of the oscillator circuitry is also displayed.

- **Conclusion and Outlook** The thesis is concluded and outlook of both the circuitry and sensor is also included.

Chapter 2

Resonator Theory and Modeling

The present chapter deals with the MEMS bulk resonator theory and background for both disk and longitudinal cantilever shape. The bulk disk resonator has two basic vibration modes, radial contour mode or called breathing mode and wine glass mode. Finite element modeling (FEM) graphs are used to indicate the two vibration modes, which are results of different anchoring techniques, anchoring at the center and disk edge, respectively. The equivalent mechanical model for both disk resonator and LBAR is a classical mass-spring-damper system, which is introduced to characterize the mechanical displacement of the resonator. The equations for corresponding resonant frequency, effective mass, effective spring constant are determined by the geometry and material property of the device. An equivalent electrical series RLC model is also able to deduced from both the mechanical model and the electromechanical coupling effect. Based on the mechanical and electrical model, the frequency and time transient responses of the displacement and the generated current by displacement are thus with no difficulty to obtain. All the disk and LBAR devices are fabricated by Ph.D student Alberto Caliani with facility in DTU nanotech and Danchip. Detailed fabrication process can be found in [29, 31].

2.1 MEMS Resonator Theory

2.1.1 Disk Resonators

Disk shaped resonators were first introduced by Nguyen *et al.* [32, 54] for its capability of attaining high frequency while retaining relatively large dimensions. The disk resonator consists of a disk suspended above the substrate. Electrodes surround the perimeter of the disk separated from the disk by a narrow gap that defines the capacitive, electromechanical transducer of this device. In principle the vibration of the resonator entirely within the plane of the device with ideally no out of plane motion or rotation motion around the centroid. There are two different types of in plane vibration modes, radial contour mode and wine glass mode [55].

2.1.1.1 Radial Contour Mode

In this case the disk is supported by a central stem as shown in Fig.(2.1(a))[32], and the disk expands equally in all the lateral surface, promoting an infinitesimal nodal point in the disk center. This anchoring configuration generates the bulk radial contour resonance mode as shown in Fig.(2.1(c)).

2.1.1.2 Wine Glass Mode

The central stem can also provide a called wine glass mode. This mode consists on the expansion and contraction of the contour shape of the disk, conforming four quasi nodal points on the structure, forming two alternate and perpendicular ellipses per cycle of vibration as shown in Fig.(2.1(d)). This mode can also appear by anchoring the disk through one or more beams on the edge of the disk shown in Fig.(2.1(b))[34].

2.1.2 Longitudinal Bulk Acoustic Resonators(LBAR)

The longitudinal bulk acoustic resonator (LBAR) is also a commonly used bulk resonator structure, which was firstly proposed by Mattila *et al.* [56]. As shown in Fig.(2.2(a)), the beam is anchored at the center and the electrodes are at the

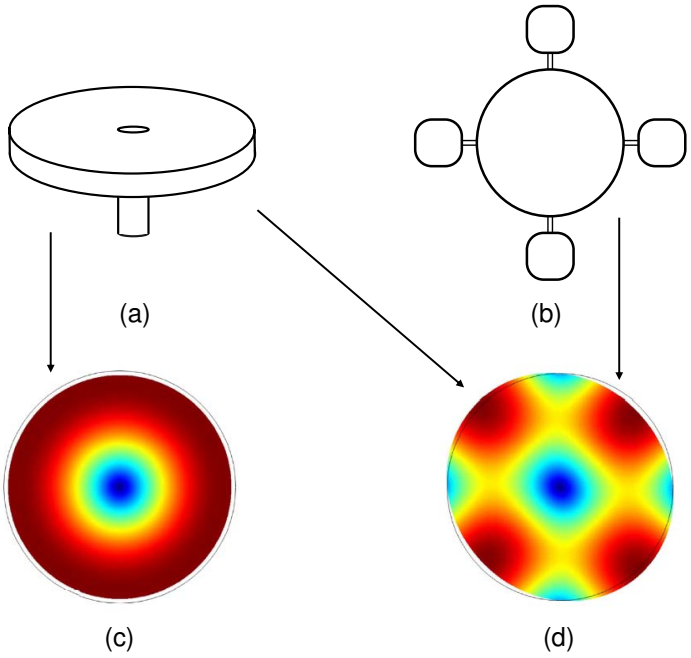

Figure 2.1: Schematic of disk resonator with (a) a single anchor at the center (b)one or more anchors connected to the edge of the disk through a single beam. Finite element modeling (FEM) plot of (c) the radial contour mode displacement (d) the wine glass mode displacement.red= max displacement, blue= minimal displacement.

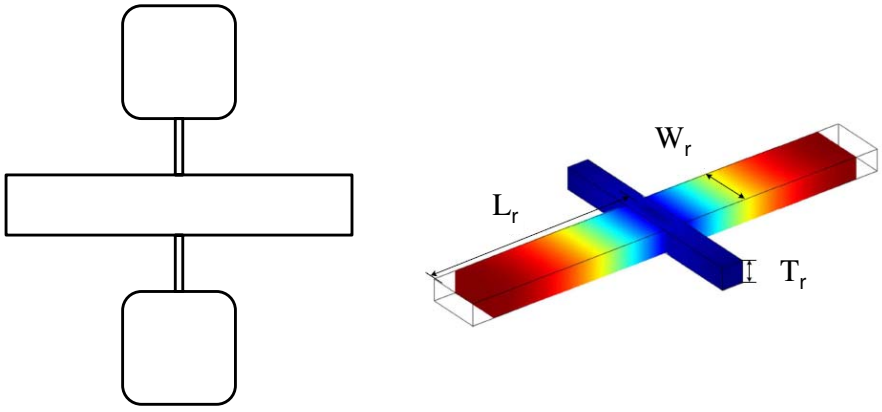

Figure 2.2: (a)Longitudinal Bulk Acoustic Resonators with tow anchors at the center of beam where L_c, W_r and T_r indicate the length, width and the thickness of the beam. (b)Finite element modeling (FEM) plot of the LBAR lateral extensional mode

two ends and are separated from the beam by the capacitive gap. The resonator vibrates on the lateral length extensional mode.Fig.(2.2(b)) shows the FEM simulation displacement of the first mode.

2.2 Equivalent Mechanical Model

The bulk resonators, no matter disk shape or longitudinal shape, can be represented by a lumped element equivalent mechanical model as that depicted in Fig.(2.3). This model composed of a rigid body mass connected to a stationary base through spring and damper elements. The resonant frequency of the

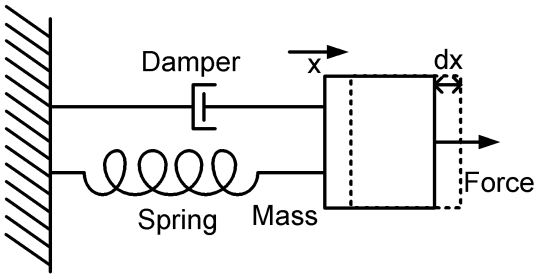

Figure 2.3: Equivalent mass-spring-damper lumped mechanical model

resonator is defined as:

$$f = \frac{1}{2\pi}\sqrt{\frac{k}{m}} \tag{2.1}$$

where k is the effective stiffness and m is the effective mass. Furthermore the value of the damping element c is:

$$c = \frac{\sqrt{km}}{Q} \tag{2.2}$$

In most cases, the Q of the resonator is difficult to predict theoretically, so the damping element is typically determined empirically. The mass and stiffness will depend on the geometry and mode shape of the mechanical resonator.

2.2.1 Disk Radial Contour Mode

The mechanical resonance frequency for the radial contour mode of a disk is governed mainly by its material properties and radius. A numerical solution for f_0 is [57]:

$$\frac{J_0(\frac{\zeta}{\xi})}{J_1(\frac{\zeta}{\xi})} = 1 - \sigma \tag{2.3}$$

Where

$$\zeta = 2\pi f_0 R\sqrt{\frac{\rho(2+2\sigma)}{E}} \tag{2.4}$$

$$\xi = \sqrt{\frac{2}{1-\sigma}} \tag{2.5}$$

Where R is the radius of the disk; E, σ and ρ are the Young's modulus, Poisson's ratio and density of its structural material, respectively; and $J_i(y)$ is the Bessel function of the first kind of order i. For Poly-Silicon:

$$\begin{aligned} E &= 160GPa \\ \sigma &= 0.22 \\ \rho &= 2.23e^{-15}kg/\mu m^3 \end{aligned}$$

while the effective mass is defined as [32]:

$$m = \frac{2\rho\pi t}{J_1(hR)^2}\int_0^R xJ_1(hx)^2\partial x \tag{2.6}$$

x is the displacement, t is the thickness and

$$h = \sqrt{\frac{\omega_0^2\rho}{\frac{2E}{2+2\sigma}+\frac{E\sigma}{1-\sigma}}} \tag{2.7}$$

2.2.2 Disk Wine Glass Mode

The frequency equation is in this case written as [34, 58, 59]:

$$[\frac{J_1(\frac{\zeta}{\xi})}{J_2(\frac{\zeta}{\xi})} - 2 - q][2J_1(\zeta) - 2 - q] = (nq - n)^2 \tag{2.8}$$

where ζ and ξ are the same as in radial contour mode equations, and

$$q = \frac{\zeta^2}{2n^2 - 2} \tag{2.9}$$

disk mode	frequency(MHz)	Mass(kg)
radial contour	74.449	10.8×10^{-12}
wine glass	66.665	3.8×10^{-12}

Table 2.1: Theoretical Resonant Frequency and Effective Mass

n is integral and is the mode number. The solutions to Bessel function appears in both the radial contour mode and the wine glass mode are periodic, so that the frequency of the nth mode corresponds to the nth solution. The fundamental mode is most important but higher order modes are also important in some cases. The resonant frequencies of the radial contour mode and the wine glass mode are quite close for the same dimension and material.While the effective mass is [61]:

$$m = \frac{\rho\pi t \int_0^R [\frac{G}{2x}J_1(G) - \frac{G}{2x}J_3(G) + \frac{2}{R}\frac{B}{A}J_2(G\xi)]^2 x dx}{[\frac{G}{2x}J_1(\frac{\zeta}{\xi}) - \frac{G}{2x}J_3(\frac{\zeta}{\xi}) + \frac{2}{R}\frac{B}{A}J_2(\zeta)]^2} \tag{2.10}$$

where

$$G = \frac{\zeta}{\xi}\frac{x}{R} \tag{2.11}$$

The calculated values for the first mode are listed in Table(2.1) with PolySilicon and the radius $R = 30\mu m$.

The frequency and effective mass of the two modes with the same geometry and material are quite close to each other. However the equations for frequency models neglect the second order effects due to the thickness and finite anchor dimensions to avoid prohibitory complex analytic formulation [35]. Thus assuming singular nodal point, zero thickness and infinite Q. Therefore the calculated results and the real values of the device will be a little bit different.

2.2.3 LBAR

The LBAR's resonant frequency of the nth mode are [31]:

$$f_{0n} = \frac{2n-1}{4L_c}\sqrt{\frac{E}{\rho}} \tag{2.12}$$

And the effective mass is more simple compared to disk resonator:

$$m = \frac{\rho W_r t_r L_c}{2} \tag{2.13}$$

2.3 Excitation Mechanism

As illustrate Fig.(2.3), when a force is applied on the mass element, the mass-spring-damper system start to move, while the movement form is determined by the features of the force. The following analysis and simulation are based on the theoretical values of a bulk disk resonator with for 30 μm radius 2.7 μm thickness and 120 nm gap distance disk resonator vibrating in a wine glass mode with $m = 9 \times 10^{-12}$ kg and $k = 1.546$ MN/m.

2.3.1 Continuous Excitation and Frequency Sweep

When the force is a sinusoidal excitation, according to the Newton second law:

$$m\frac{d^2x}{dt^2} + c\frac{dx}{dt} + kx = F_{AC}\sin\omega_s t \tag{2.14}$$

which can be rewritten as:

$$\frac{d^2x}{dt^2} + \frac{\omega_0}{Q}\frac{dx}{dt} + \omega_0^2 x = \frac{F_{AC}\sin\omega_s t}{m} \tag{2.15}$$

where

$$\omega_0 = \sqrt{k/m} \tag{2.16}$$

is the undamped angular frequency and

$$Q = \sqrt{km}/c \tag{2.17}$$

is the quality factor. The steady-state solution for Eqn.(2.15) [62] is:

$$x_{ss}(t) = \frac{F_{AC}}{mZ_m\omega_s}\sin(\omega_s t + \phi) \tag{2.18}$$

where

$$Z_m = \sqrt{(\frac{\omega_0}{Q})^2 + \frac{1}{\omega_s^2}(\omega_0^2 - \omega_s^2)^2} \tag{2.19}$$

and

$$\phi = arctan(\frac{1}{Q}\frac{\omega_s\omega_0}{\omega_s^2 - \omega_0^2})|_{\omega_0 \approx \omega_s} \approx \frac{\pi}{2} \tag{2.20}$$

are the amplitude and phase of the mass motion, respectively.

Fig.(2.4) shows the magnitude and phase curve as as a function of the frequency sweep with the input force magnitude $F_{AC} = 2 \times 10^{-6}$ N. When excitation frequency is exactly the same frequency as the resonant frequency, the magnitude of the output is then at its largest:

$$|x_{ss}| = \frac{QF_{AC}}{k} \tag{2.21}$$

It is determined by the resonant frequency and also the Q factor. By using a higher Q factor resonator, the magnitude of the vibration is increased and the bandwidth is decreased. While as the excitation frequency deviate from the resonant frequency, the output magnitude drop quickly. The frequency bandwidth is less than 100 kHz for Q factor around 4000.

2.3.2 Burst Excitation and Time Transient

The alternative excitation to the frequency sweep is the burst mode [52, 53] which utilize a single excitation frequency close to the resonant frequency, and the excitation stops at a certain time. In this case not only the steady state is interesting but also the full time transient response is examined.

2.3.2.1 During Excitation

During the excitation, the system fits the same equation as in Eqn.(2.14), and the time transient solution for the equation is found to be:

$$x_e(t) = (K_1 \sin \omega_d t + K_2 \cos \omega_d t)e^{-at} + x_{ss}(t) \tag{2.22}$$

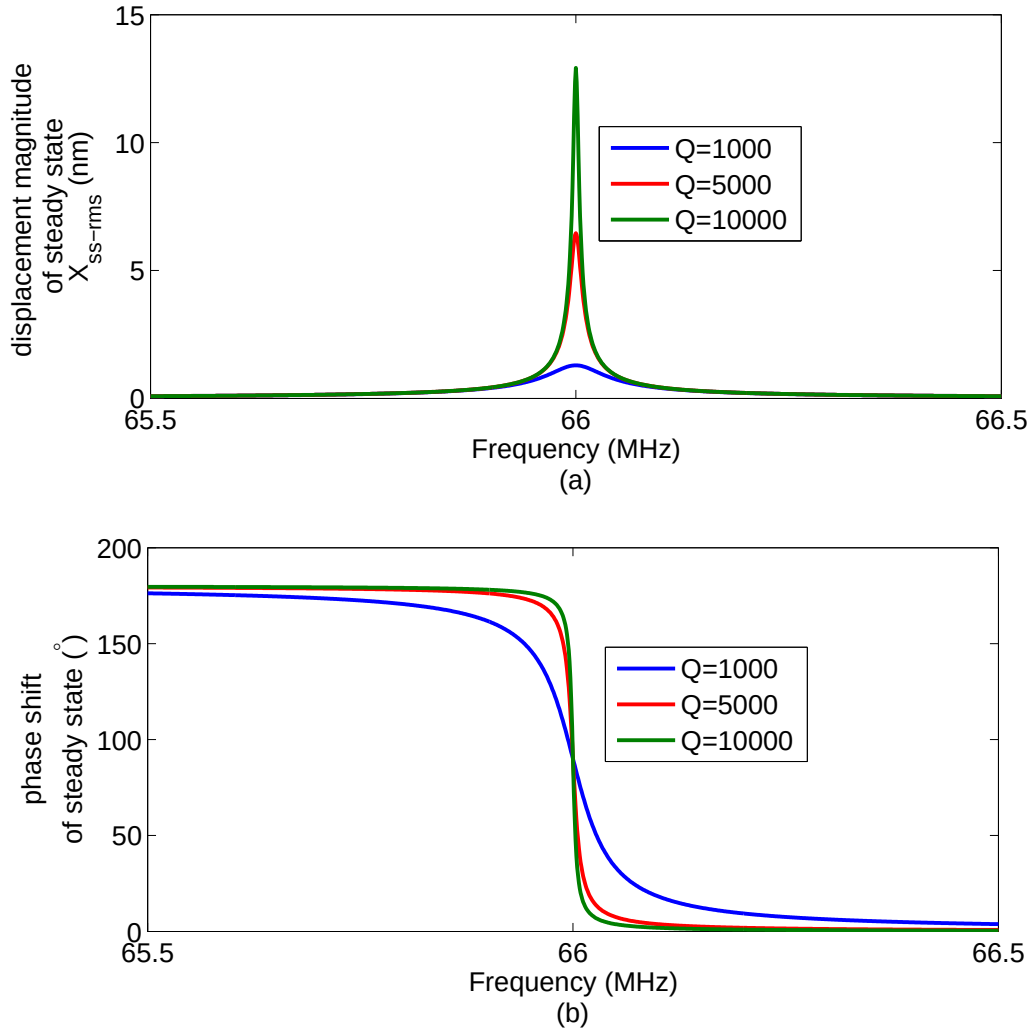

Figure 2.4: Simulation results of the steady state (a) vibration magnitude (b) phase under sinusoidal excitation, when sweeping the frequency around resonance for Q factor 1000, 5000 and 10000, respectively.

where

$$\omega_d = \omega_0\sqrt{1-(\frac{1}{2Q})^2} \tag{2.23}$$

is the damped radial frequency (which is very close to the undamped radial frequency when Q factor is large), and $a = \omega_0/(2Q)$. K_1 and K_2 can be calculated from initial boundary conditions of displacement:

$$x_e(0) = 0 \tag{2.24}$$

and velocity

$$v = \frac{dx_e}{dt}|_{t=0} = 0 \tag{2.25}$$

and thus are:

$$K_1 = -\frac{F_{AC}}{2m\omega_s\omega_d} \approx -\frac{F_0}{2m\omega_0^2} = -\frac{F_{AC}}{2k} \tag{2.26}$$

$$K_2 \approx \frac{QF_{AC}}{m\omega_0^2} = \frac{QF_{AC}}{k} \tag{2.27}$$

Therefore, Eqn.(2.22) can be rewritten as:

$$x_e(t) = \frac{F_{AC}}{k}[-Q\cos\omega_s t + (-\frac{1}{2}\sin\omega_d t + Q\cos\omega_d t)e^{-at}] \tag{2.28}$$

where $a = \omega_0/2Q$.

Some important features are described as follows.

- **Time Constant:** $\tau = 2Q/\omega_0 \approx 20\,\mu$s is determined by the mechanical system itself rather than the input signal. The high Q mass spring damper system needs a long time to approach steady state compared to the resonant period which is approximately $0.02\,\mu$s.

- **Bandwidth at Steady State:** Fig. (2.5)shows the transient response of displacement under the same excitation force, but with input frequency differing from the resonant frequency by 0 Hz, 1 kHz, 10 kHz and 100 kHz, respectively. The excitation time is long enough to ensure that the resonator reaches its steady state. It is seen from the figure that the amplitude of the steady state displacement is largely determined by the input frequency. Due

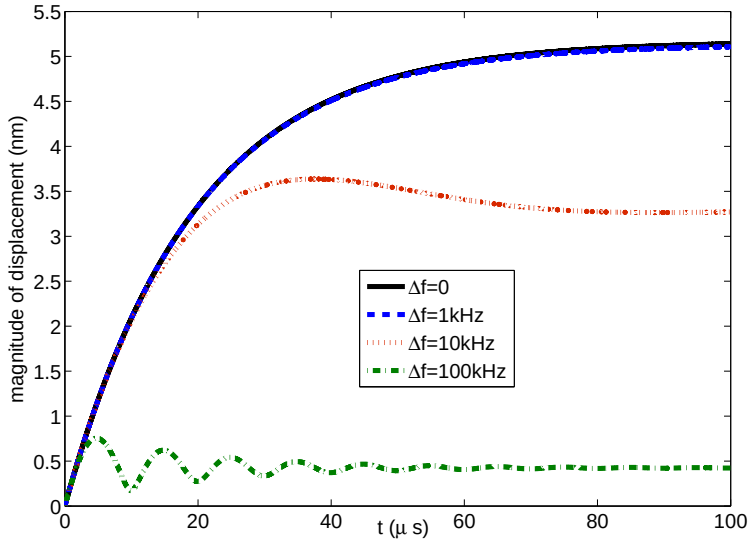

Figure 2.5: Simulation results of the transient response of the vibration magnitude during sinusoidal excitation with frequencies differ from resonant frequency by $0MHz$, $1kHz$, $10kHz$ and $100kHz$, respectively. The excitation time last for $100\mu s$, and the resonator reaches its steady state.

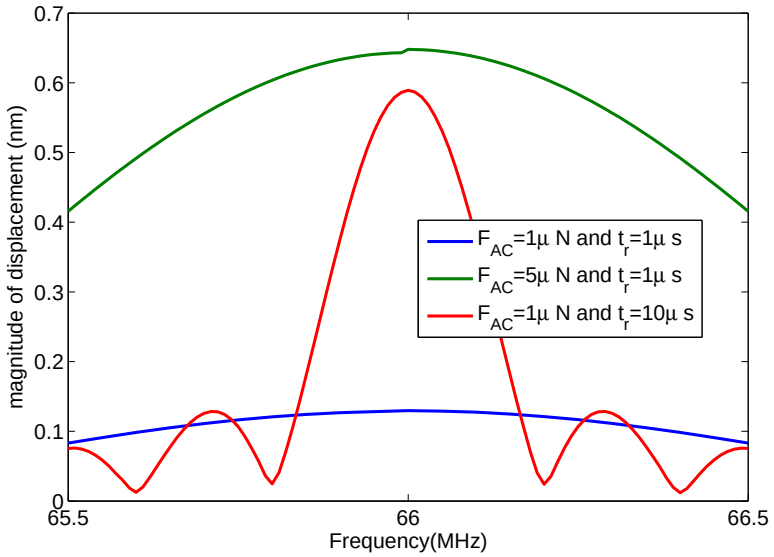

Figure 2.6: Simulation results of the magnitude of displacement at the end of excitation time t_r with excitation frequencies sweep. Q factor is 4000.

to the high quality factor, a small frequency deviation of the input excitation frequency from the resonant frequency will generate a huge difference of displacement magnitude. 10 kHz difference leads to 40 percentage magnitude decrease while 100 kHz difference leads to 90 percentage magnitude decrease. Therefore, the bandwidth of steady state is only around 10 kHz.

- **Steady State Displacement:** For large excitation voltages, when the excitation frequency is quite close to the resonant frequency (within 1 kHz), the disk generates a steady state displacement (up to 12 nm when $F_{AC} = 2 \times 10^{-6}$ N), which can be large enough (compared to gap distance 120 nm) to induce non-linear effects and the linear equivalent mechanical model will not be applicable at this moment.

- **Excitation Force:** The transient response of the displacement is proportional to the amplitude of the excitation force F_{AC} as shown in Fig.(2.6) blue and green line with the same excitation time.

- **Bandwidth at Linear Region:** As shown in Fig.(2.6) with short excitation time (blue and green line 1 μs), the resonator is far away from the steady state and the bandwidth is almost 1 MHz around the resonant frequency 66 MHz. However with long excitation time (red line 10 μs), the magnitude of the displacement is highly increased while the bandwidth shrink to about 200 kHz. In order to maintain the large bandwidth at linear region so we can use a single excitation signal to drive the different resonators. The best solution is to minimize the excitation time and to maximize the excitation force (green line).

As a summary, the most efficient way to excite the resonator is (1) decreasing the excitation time and (2) increasing the excitation force in order to achieve the largest vibration within a broader bandwidth. The large bandwidth permits to excite sensing resonators with different resonant frequencies. By varying the excitation time, the bandwidth can be adjusted to fit the requirement of these mass sensing applications.

2.3.2.2 Free Vibration

After the force is released at time t_r, the system starts free vibration. It doesn't matter when t_r happens with respect to a specific point in the cycle, since the energy in the system is almost conserved.

$$\begin{aligned} E &= \frac{1}{2}mv^2 + \frac{1}{2}kx^2 && (2.29)\\ &= \frac{F_0^2}{2k}[Q(1-e^{-at_r})\sin\omega_d t_r\cos\omega_d t_r && (2.30)\\ &+ \frac{1}{4}e^{-2at_r} + Q^2(1-e^{-at_r})^2(\sin^2\omega_d t_r) && (2.31)\end{aligned}$$

since $Q(1-e^{-at_r}) \gg 1$, components with $\sin\omega_d t_r$ or $\cos\omega_d t_r$ can be neglected thus.

$$E \approx \frac{F_0^2}{2k}Q^2(1-e^{-at_r})^2 \tag{2.32}$$

Which is independent on $\omega_d t_r$. We can safely assume $\omega_d t_r = 2n\pi$ to simplify the calculation, where n is an integer value.

The free vibration satisfies the differential equation:

$$\frac{d^2x}{dt^2} + \frac{\omega_0}{Q}\frac{dx}{dt} + \omega_0^2 x = 0 \tag{2.33}$$

and the transient response for free vibration is

$$x_f(t) = e^{-at}(K_3\sin\omega_d t + K_4\cos\omega_d t) \tag{2.34}$$

where the decaying time constant $\tau = 1/a = 2Q/\omega_0$ is the same as the excitation time constant and is independent on the release time. The initial conditions are:

$$x_f(0) = x_e(t_r) \tag{2.35}$$

$$\frac{dx_f}{dt}|_{t=0} = \frac{dx_e}{dt}|_{t=t_r} \tag{2.36}$$

Therefore,

$$K_3 = \frac{F_{AC}}{2k}(1-e^{-at_r}) \tag{2.37}$$

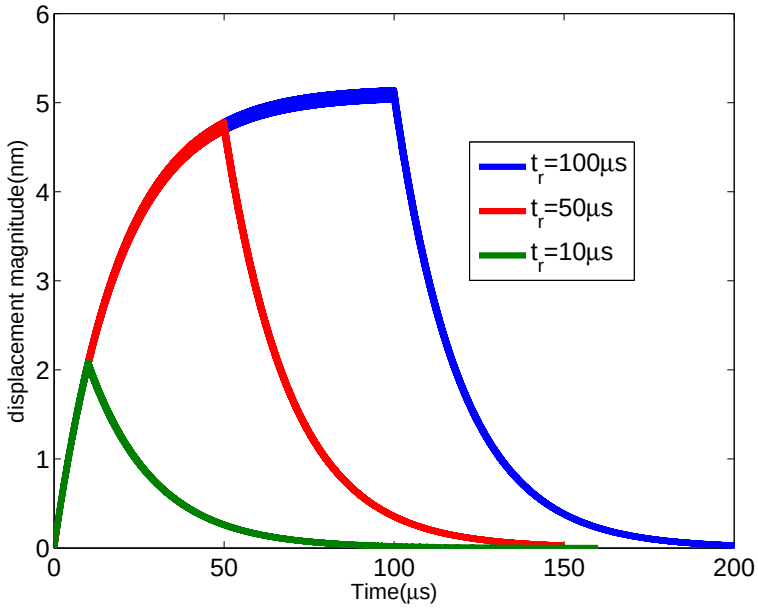

Figure 2.7: Full time transient response with different excitation duration

$$K_4 = -\frac{QF_{AC}}{k}(1 - e^{-at_r}) \tag{2.38}$$

Eqn.(2.34) can be rewritten as:

$$x_f(t) = \frac{F_{AC}}{k}e^{-at}(1 - e^{-at_r})(\frac{1}{2}\sin\omega_d t - Q\cos\omega_d t) \tag{2.39}$$

It is seen from the equation that the amplitude of the free vibration is larger when the excitation lasts longer for the same damping constant as is shown in Fig. (2.7).

2.4 Equivalent Electrical Model

The equivalent mechanical mass-spring-damper system can be transferred directly into equivalent electrical behavior presented by an equivalent series inductor-resistor-capacitor circuit as shown in Fig.(2.8) [32]. The values of the series l_x,c_x

and r_x are:

$$l_x = m \tag{2.40}$$
$$c_x = \frac{1}{k} \tag{2.41}$$
$$r_x = c \tag{2.42}$$

An electrostatic actuation is achieved by applying a voltage across the capacitive gap which results in an electrostatic force. The electrostatic force is then given by [63]:

$$F = \frac{1}{2}\frac{\partial C_f}{\partial x}V^2 \tag{2.43}$$

while V is the cross voltage and C_f is the feedthrough capacitance between the overlap area of disk and w is the effective width at the coupling area.The capacitive gap introduces the electromechanical coupling coefficient η defined as the ratio of the electrostatic force and voltage. The electromechanical coupling thus transfers the output from the disk to the electrodes, and generates the whole series RLC model seen from the input output electrode:

$$\begin{aligned} C_x &= \frac{\eta^2}{k} \\ L_x &= \frac{m}{\eta^2} \\ R_x &= \frac{\sqrt{km}}{Q\eta^2} \end{aligned} \tag{2.44}$$

With the equivalent electrical model for MEMS resonator, it is easier to simulate the electrical measurement and also to design the readout circuitry.

2.4.1 Frequency Response for Equivalent Electrical Model

The whole resonator device performs as a voltage controlled current source:

$$i_{out} = \frac{v_{in}}{R_x + j\omega L_x + 1/j\omega C_x} \tag{2.45}$$

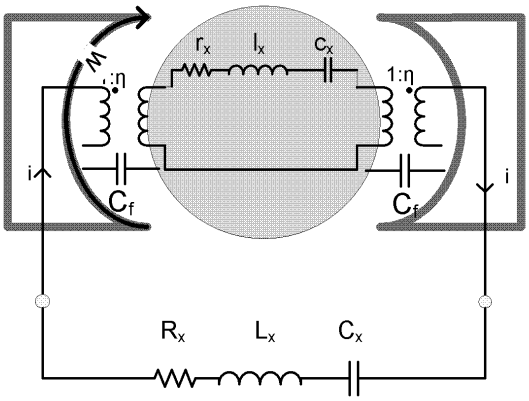

Figure 2.8: Equivalent circuit for disk electrical model

2.4.2 Time Transient Response for Equivalent Electrical Model

In mechanical model,the position x,velocity dx/dt and the drive force $F(t)$ are corresponding to the charge q, current dq/dt, and the cross voltage $V(t)$. The differential equation for mechanical model (2.14) then can be converted to in electrical equation:

$$L_x \frac{d^2q}{dt^2} + R_x \frac{dq}{dt} + q/C_x = V_{AC} f(t) \tag{2.46}$$

where V_{AC} is the amplitude of the input sinusoidal voltage and is equal to F_{AC}/η and q is the charge.The current solution for steady state, time transient response during excitation and time transient response during free vibration are:

$$i_{ss}(t) = V_{AC} C_x \omega_0 Q \sin \omega_s t \tag{2.47}$$

$$i_e(t) \approx V_{AC} C_x [-Q\omega_s \sin \omega_s t + (\frac{1}{2}\omega_s \cos \omega_d t + \omega_d Q \sin \omega_d t) e^{-at}] \tag{2.48}$$

$$i_f(t) \approx -V_{AC} C_x Q \omega_d (1 - e^{-at_r}) e^{-at} \sin \omega_d t \tag{2.49}$$

the approximation is made since $a = \omega_0/(2Q) \ll Q\omega_d$ and $Q \gg 1$.

2.5 Summary

As a summary for this chapter, we displayed the configuration of disk and LBAR resonators. We demonstrated the FEM simulation graph of the two mode for disk resonator -the contour mode and the wine glass mode- caused by the different anchoring position -single anchor in the center and one or more anchors at the edge. We have also introduced the equivalent mass spring damper model and deduced the mechanical equation for these values. With the mechanical model, we were able to calculate the time transient displacement for pulsed force excitation. At last, the equivalent electrical model was also described which will be used in the next chapter to analyze different readout and measurement methods.

Chapter 3

Measurement Theory

As is stated in Chapter 2, the MEMS resonators are driven by the electrostatic force from the electromechanical coupling. The effect of coupling and the feedthough capacitance of the whole device depend on the configuration of the measurement setup. The four commonly used measurement configurations is displayed in this chapter, with the corresponding equivalent electrical model. They have their own advantages and disadvantages under the inspection of the complexity of the setup, the efficiency of grounding the parallel capacitance and the improvement of the output. The influence of the parallel capacitor on both frequency domain and time domain measurement setup is demonstrated based on the resulting frequency noise and deformation of time transient output during excitation. Two compensation techniques are displayed. Finally, possible pulse excitation inputs are examined.

3.1 Measurement Configurations

3.1.1 One Port Measurement

The one port direct measurement scheme is depicted in Fig. (3.1(a)) [32]. The two electrodes are connected as a single input electrode, with input AC signal couple to a DC bias from a bias-T, while output signal is measured directly from the disk. Therefore, the two feedthough capacitors from both of electrodes are connected in parallel, contribute a doubled size of total feedthough capacitor $2C_f$. The applied voltage is then $V_{DC} + V_{AC}cos(\omega_0 t)$ at resonant frequency ω_0, and the

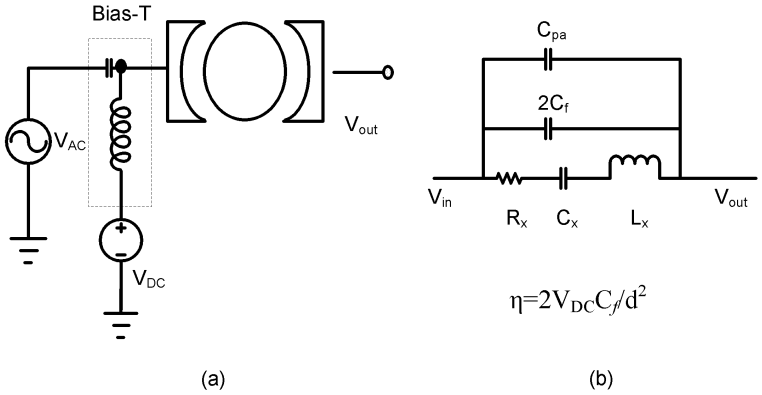

Figure 3.1: One port measurement (a)setups (b) full small signal circuit model

actuator force is then:

$$\begin{aligned} F &= \frac{1}{2}\frac{2\partial C_f}{\partial x}(V_{DC} + V_{AC}\cos\omega_0 t)^2 \\ &= \frac{\partial C_f}{\partial x}(V_{DC}^2 + \frac{V_{AC}^2}{2} + 2V_{AC}V_{DC}\cos\omega_0 t + \frac{V_{AC}^2}{2}\cos 2\omega_0 t) \end{aligned} \tag{3.1}$$

where $V_{AC} << V_{DC}$. The effective electrostatic force at resonant frequency is then:

$$F_{AC} = 2\frac{\partial C_f}{\partial x}V_{DC}V_{AC} \tag{3.2}$$

According to the equation for capacitor:

$$C_f = \frac{\epsilon_0 wt}{d+x} \tag{3.3}$$

ϵ_0 is the permittivity of free space and equals to $8.854^{-12}F/m$.

$$\frac{\partial C_f}{\partial x} = -\frac{\epsilon_0 wt}{(d+x)^2} \approx -\frac{C_f}{d^2} \tag{3.4}$$

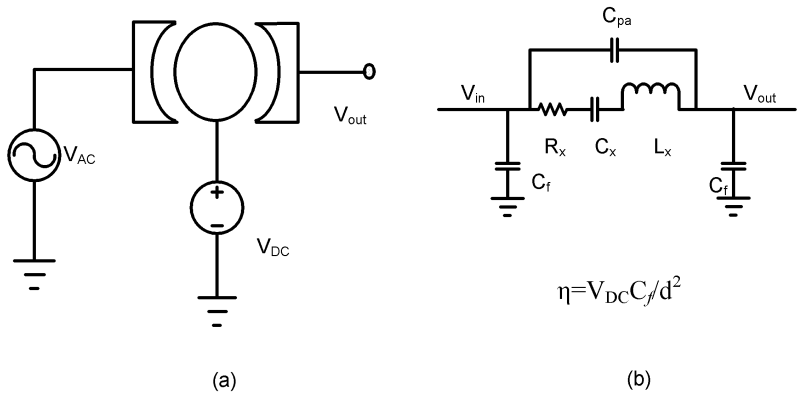

Figure 3.2: Two port measurement (a)setups (b) full small signal circuit model

therefore, the electromechanical coupling coefficient is:

$$\eta = 2V_{DC}\frac{C_f}{d^2} \tag{3.5}$$

The series RLC model as shown in Fig.(3.1(b)). There is also an extra parasitic capacitor C_{pa} in parallel with the series model, due to the fringing coupling, which is described in more details in Section 2.1.

3.1.2 Two Port Measurement

The two port measurement scheme is shown in the Fig. (3.2(a)) [32]. The DC bias is applied directly to the disk without the need for a Bias-T. The AC input signal is applied to one of the electrodes and the output is detected from the other. Thus, DC, AC input and output are separated. The coupling coefficient in two port setup is only half of the one in one port setup, since the input voltage is only excited upon a single electrode.The effective force of resonant frequency

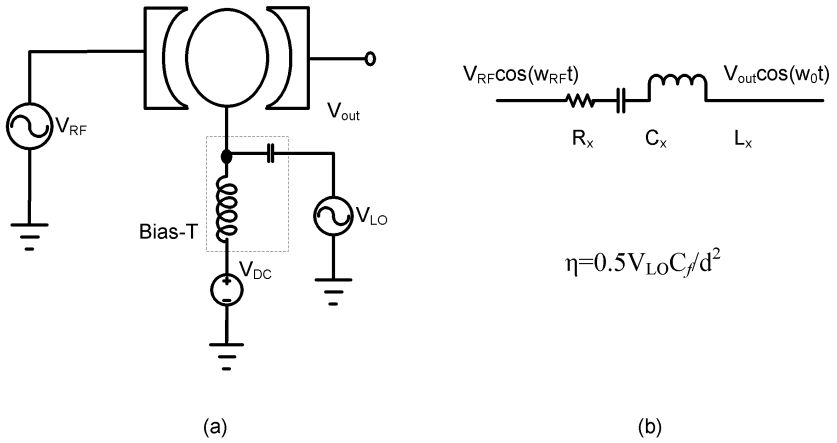

Figure 3.3: Mix measurement (a)setups (b) full small signal circuit model

is then:

$$F_{AC} = \frac{\partial C_f}{\partial x} V_{DC} V_{AC} \tag{3.6}$$

and the electro mechanical coupling coefficient η for two port setup is then:

$$\eta = V_{DC} \frac{C_f}{d^2} \tag{3.7}$$

In two port measurement, the electromechanical couplings are only from one side, therefore the coupling coefficient is only half of the one from the one port measurement. However since the input and output electrodes are separated, and the disk is connected with bias which in small signal model is virtually grounded, the two feedthrough capacitors are then grouped though the disk as shown in Fig.(3.2(b)). In the two port measurement, the same parasitic capacitor as in one port setup exists in parallel with the series model.

3.1.3 Mix Measurement

The mix measurement [64] scheme is shown in the Fig.(3.3(a)). The DC bias is coupled with a local oscillator $V_{LO}cos\omega_{LO}t$ though a bias-T, and is applied to the disk while the input signal $V_{RF}cos\omega_{RF}t$ is applied to one of the electrodes. The output is traced from the other electrode. When the frequency difference of ω_{LO} and ω_{RF} is the resonant frequency ω_0, the mixing effect of corresponding electrostatic force at resonant frequency is then:

$$F_{AC} = \frac{1}{2}\frac{\partial C_f}{\partial x}V_{LO}V_{RF} \tag{3.8}$$

and the electromechanical coupling coefficient is then:

$$\eta = \frac{1}{2}V_{LO}\frac{C_f}{d^2} \tag{3.9}$$

In mix measurement, the coupling effect also comes from a single electrode as in two port measurement, but the difference in the coupling coefficient is proportional to V_{LO} rather than V_{DC}, while small signal V_{LO} is much smaller than V_{DC}. Therefore, the coupling effect in the mix measurement is much weaker. However, the parallel capacitor in the mix measurement is almost zero as shown in Fig.(3.3(b))since the input and output signal are in different frequencies ω_{RF} and ω_0 respectively , and they are far away from each other.

3.1.4 Differential Measurement

The differential measurement scheme needs four electrodes as shown in Fig. (3.4(a)) [65]. The DC bias is applied directly on the disk, and a differential AC signal is applied on two orthogonally oriented electrodes and the AC output which are 180° shifted due to the wine glass mode shape, are collected on the two other electrodes. In this configuration, the corresponding electrostatic force is the same as in one port scheme since two electrodes are used as the input coupling. Furthermore, the output is also collected from two electrodes, therefore is double

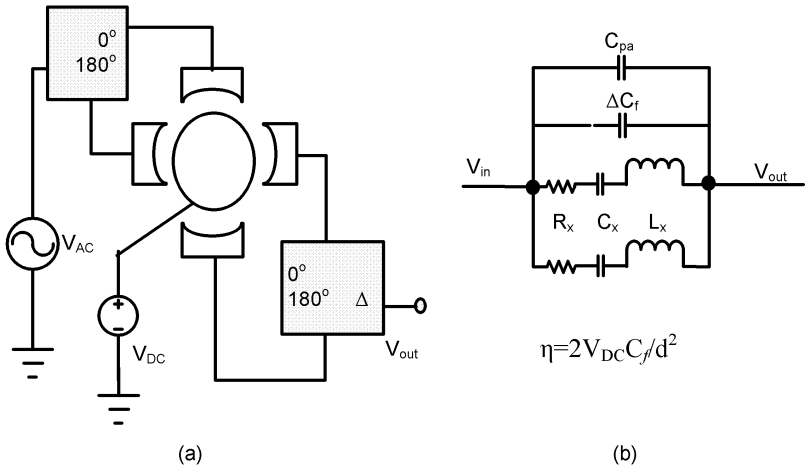

Figure 3.4: Differential measurement (a)setups (b) full small signal circuit model

of the one port measurement output as shown in Fig. (3.4(b)).

$$F_{AC} = 2\frac{\partial C_f}{\partial x} V_{DC} V_{AC} \cos \omega_0 t \tag{3.10}$$

and the electromechanical coupling coefficient is then:

$$\eta = 2V_{DC}\frac{C_f}{d^2} \tag{3.11}$$

In the differential measurement setup, the effect of feedthrough capacitor from one of the electrode pair subtracts each other, leaving only the difference ΔC_f in parallel with the motional series RLC circuit rather than the total feedthrough capacitor C_f. ΔC_f comes from the error of the fabrication process and is much smaller than C_f. As the same as in one port and two port measurement, the parasitic capacitor is also exist in the differential setup.

The features of the different measurement techniques are summarized in Table (3.1).

technique	electrodes	set up	coupling effect	C_p
one port	2	medium	strong	large
two port	2	simple	medium	small
mix	2	complex	weak	smallest
differential	4	complex	strong	medium

Table 3.1: Features of frequency sweep measurement techniques

3.1.5 Source of Parasitic Capacitor

The extra parasitic capacitor C_{pa} [66] connected in parallel with series RLC model is mainly from three aspects as shown in Fig. (3.5):

- The capacitance through the substrate via the bond pads. Better grounding of the substrate is therefore extremely important.
- The capacitance between the input and output probes. This capacitance can be largely reduced with the RF Ground-Signal-Ground probes, by shielding the contact pads shown in Appendix A.
- The bonding pad capacitor

Normally C_{pa} is also much smaller than the feedthough capacitor C_f.

3.2 Influence of Parallel Capacitor

3.2.1 Parallel Capacitor on Frequency Response

3.2.1.1 Frequency Noise

An example frequency response with and without the influence of parasitic capacitors are shown in Fig. (3.6) and Fig. (3.7), respectively. The parallel feedthough capacitor creates a parallel-resonance frequency given by [67]:

$$f_p = f_0\sqrt{1+\frac{C_x}{C_p}} \tag{3.12}$$

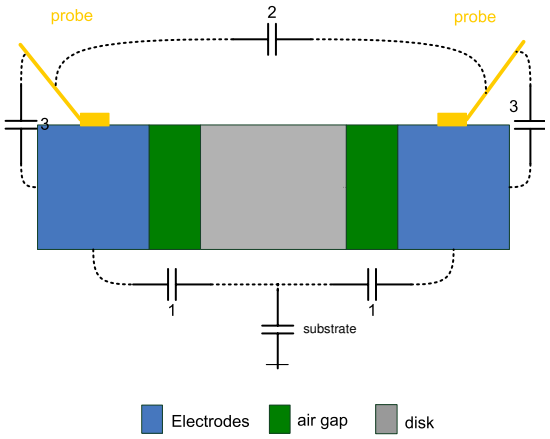

Figure 3.5: Side view of the measurement setup for disk resonator.

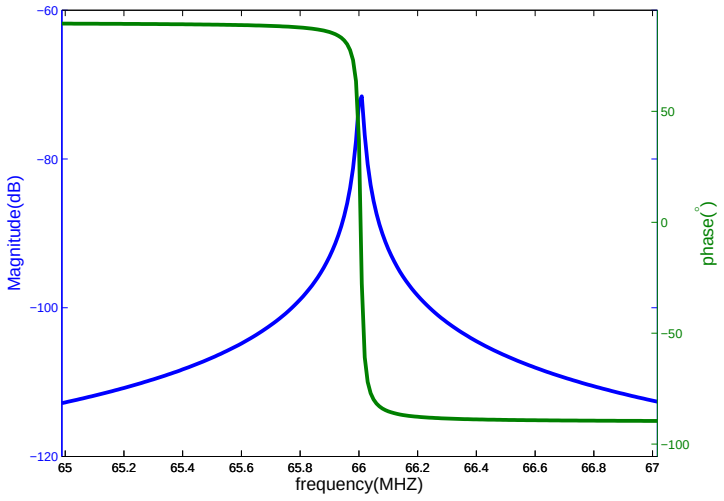

Figure 3.6: Frequency response of pure motional series RLC model.

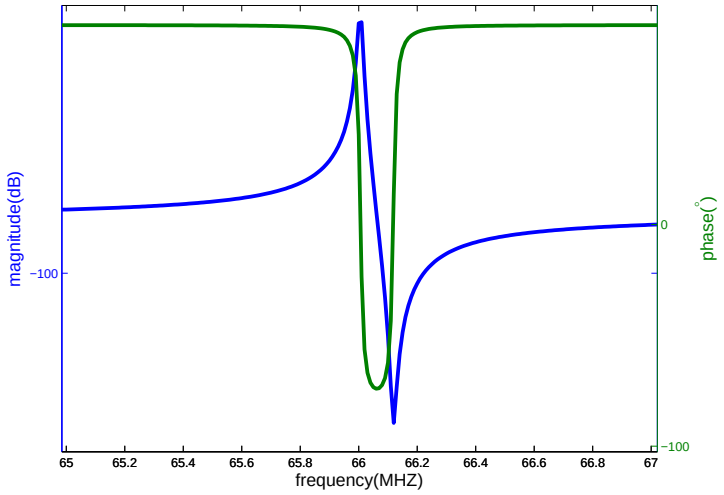

Figure 3.7: Frequency response of full model including the parallel capacitor.

since C_p is usually much bigger than C_x. this value thus is quite close to the series resonant frequency f_0. However,the parallel capacitor still distorts the measured signal by introducing an anti-resonance at the frequency response as in Fig. (3.7), therefore it does not only make it difficult to deduce the precise response of the pure mechanical movement, but also increases the frequency noise, which is defined as:

$$\Delta f = \frac{\Delta\phi}{\partial\phi/\partial f} \tag{3.13}$$

where $\Delta\phi$ is the phase noise and $\Delta\phi/\Delta f$ is the phase gradient. The phase noise is determined by the measurement setup:

- Noise from the equipment: analyzer, DC power supply and so on.
- Noise from cables and probes.
- Stable touching of the probe legs on the surface of the electrodes.
- Environment temperature and moisture.

On the contrary, the phase gradient is determined by the MEMS device itself.

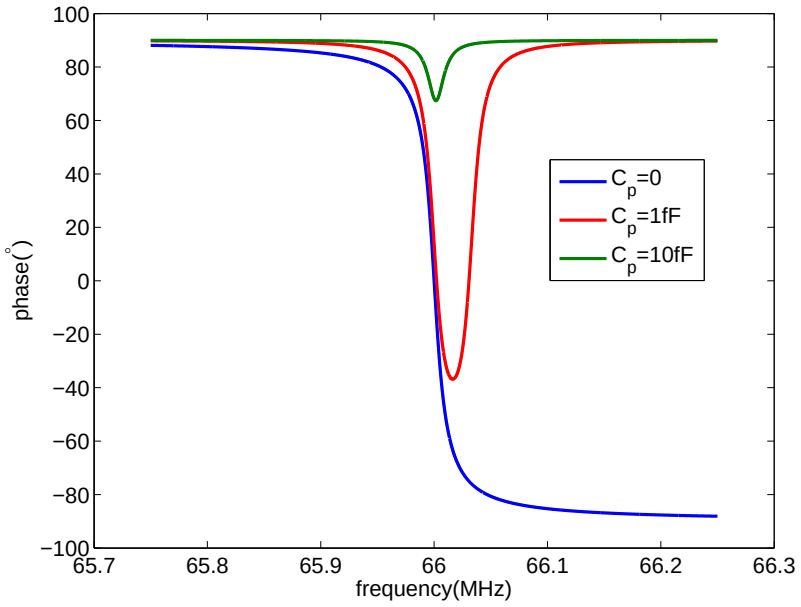

Figure 3.8: Frequency response for different parallel capacitor.

For pure motional series RLC model, the phase is:

$$\phi = arctan(Q\frac{\omega^2 - \omega_0^2}{\omega\omega_0}) \tag{3.14}$$

while the phase for the whole device including the parallel capacitor is:

$$\phi_p = arctan(\frac{C_x Q^2\omega_0^2(-\omega^2 + \omega_0^2) + C_p(\omega^2\omega_0^2 + Q^2(\omega^2 - \omega_0^2)^2)}{C_x Q\omega\omega_0^3}) \tag{3.15}$$

Fig.(3.8) shows the phase around the resonant frequency, when the motional capacitor is 1 aF, Q factor 4000 and the resonant frequency $66MHz$. The parallel capacitor is 0 (for only motional model) and 1 fF, 10 fF for real system. It is seen that the larger the parallel capacitor, the smaller the phase shift.

The phase gradient for motional model is given as:

$$\frac{\partial\phi}{\partial\omega} = \frac{Q\omega_0(\omega^2 + \omega_0^2)}{\omega^2\omega_0^2 + Q^2(\omega^2 - \omega_0^2)^2} \tag{3.16}$$

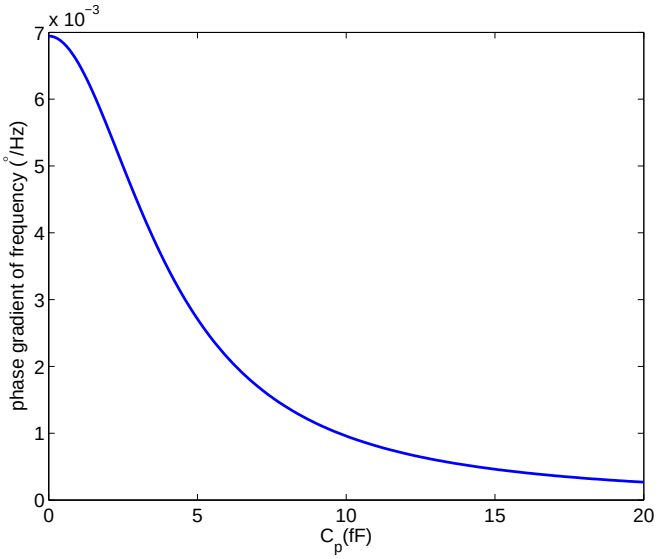

Figure 3.9: Phase gradient change at parallel resonant frequency VS parallel capacitor.

$$= \frac{2Q}{\omega_0}|_{\omega=\omega_0}$$

and after including the parallel capacitor the phase gradient at parallel resonant frequency is then:

$$\frac{\partial \phi_p}{\partial \omega} = \frac{C_p/C_x + 2Q^2}{(C_p/C_x)^2 + (C_p/C_x) + Q^2} \frac{Q}{\omega_0} \tag{3.17}$$

Fig.(4.2) shows the larger the parallel capacitor, the smaller the phase gradient at resonance. Therefore, according to Eqn.(3.13), under a certain amount of phase noise, the larger the frequency gradient, the smaller the frequency noise. At the same time, for mass sensor, since

$$\Delta m \approx -2m(\Delta f / f_0) \tag{3.18}$$

the mass resolution Δm is also determined from frequency noise. Therefore, a smaller parallel capacitor is required for sensitive mass detection.

3.2.1.2 Compensation techniques

As summarized in Table (3.1), the mix measurement has the lowest parallel capacitor, however it is not efficient for coupling, which means the output motional current generated is also very low with the same input power as other measurement techniques. The differential measurement and two port measurement also have low parallel capacitors, but the differential measurement needs four electrodes which increase the difficulty of fabrication and the two port measurement is less efficient than one port measurement in coupling. Therefore, one port measurement technique is still very commonly used.

In order to decrease the influence of the large parallel capacitor, two compensation techniques are widely used [68] as shown in Fig. (3.10). The idea is also coming from the differential measurement, that is differential input or output. The first one is with tunable capacitor. The differential inputs are applied to the MEMS device and a tunable capacitor C_c respectively while the two outputs are connected together. Therefore, the effect of the parallel capacitor C_p in the MEMS device can be subtracted by tuning the capacitor C_c until the anti-peak totally disappear. The second one is using two identical devices, one is charged with DC bias therefore perform as a normal resonator, while the other is without DC charge therefore perform as a single capacitor. The two differential outputs achieve the function of subtraction. Obviously, the second technique is more precise than the first one, since the two devices are identical, and the two parallel capacitors are very close to each other.

3.2.2 Parallel Capacitor in Burst Mode

During the excitation, the parallel capacitor contributes to an extra current component $\omega_s C_f V_{AC} \sin \omega t$ in together with the motional current from the RLC model; while at the shut down point, the parallel capacitor discharges the current to ground with the time constant $R_{Load} C_f$, which is much smaller than the time constant of the mechanical motion part τ. Therefore, the parallel component disappears almost instantaneously, leaving only the mechanical motion component. Therefore, the pulse measurement technique is totally unrelated to the parallel capacitor. Fig. (3.11) shows the total output current with different values of

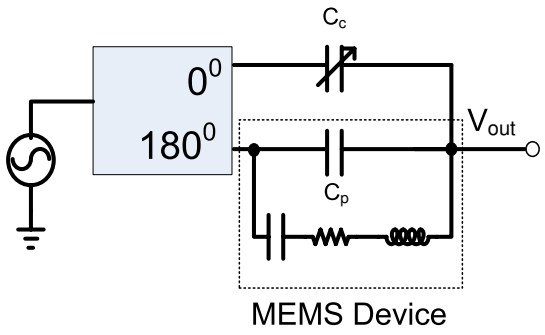

(a)

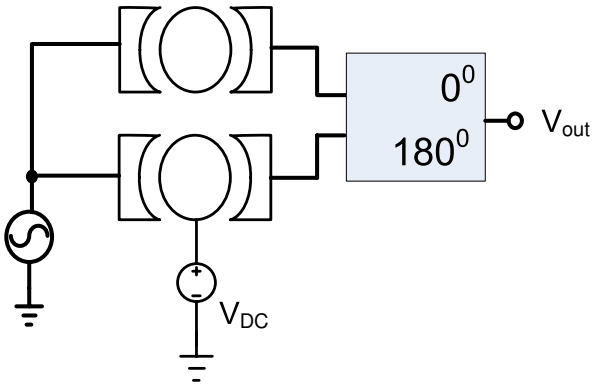

(b)

Figure 3.10: Parasitic compensation (a) with tunable capacitor (b) with uncharged identical device

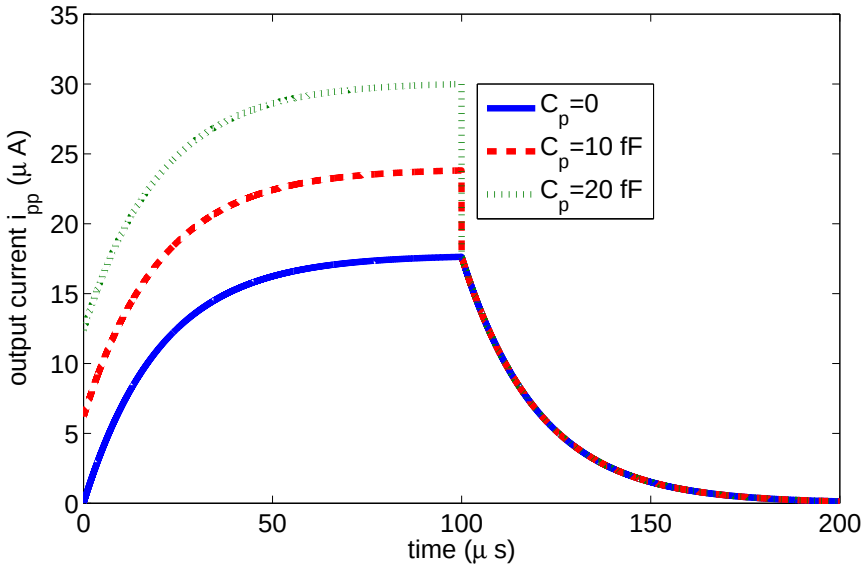

Figure 3.11: Simulation result are the magnitude of the output current with C_f equal to 0, 10 fF and 20 fF, respectively. Excitation lasts 100 μs and afterwards is released, using $V_{AC} = 1.5\,\mathrm{V}$ and $V_{DC} = 16\,\mathrm{V}$.

parallel capacitor. With larger parallel capacitor, the output level during the excitation is larger, while the output during the free vibration is totally identical to others with different size of parallel capacitor.

3.3 Other Pulse Excitation

The ideal excitation signal for MEMS resonator should have the following features:

- First, the excitation input should supply enough power at the resonant frequency, therefore the output response is large enough to be sensed.
- Second, the excitation input should has a flat and wide bandwidth, so that the detectable range of the frequency shift and therefore the mass change is wide as well. Furthermore, if the bandwidth is wide enough to reach the higher harmonic frequencies, more vibration modes can be excited

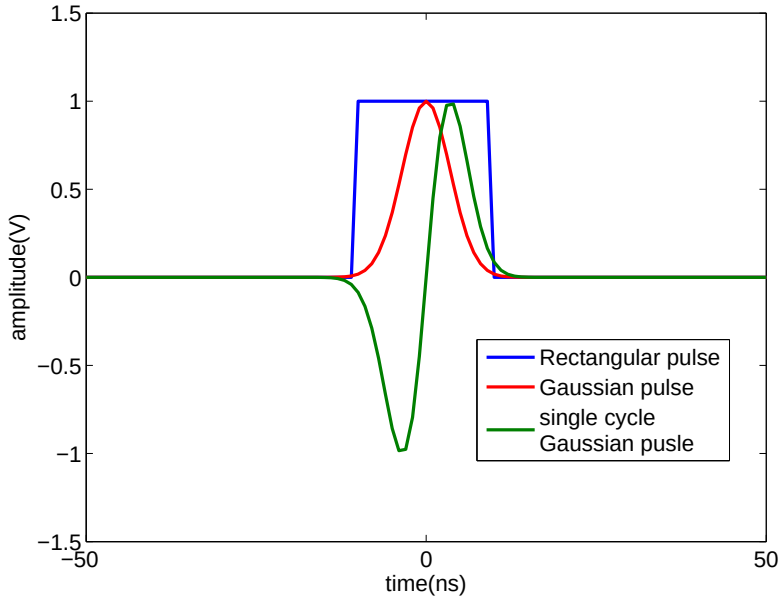

Figure 3.12: Time signal of Rectangular, Gaussian and single cycle Gaussian pulses

simultaneously.

Therefore, we also would like to try with other kind of excitation signals for example the most commonly used rectangular pulse, Gaussian pulse and single cycle Gaussian pulse. The Gaussian pulse is defined as [69]:

$$x_1(t) = A_1 e^{(-t/t_d)^2} \tag{3.19}$$

The first derivative of Gaussian pulse called as single cycle given by

$$x_2(t) = A_2 t e^{-(t/t_d)^2} \tag{3.20}$$

where t_d is the duration of the pulse and A_n are the amplitudes.Fig.(3.12) shows the time signal shape of the three types of pulse single.

Fig. (3.13) shows the power spectrum [70] of the three pulse signals.All the amplitude of the singles are $1V$. As is seen, the rectangular pulse and Gaussian pulse demonstrate a low pass window, which means the power of there two pulse

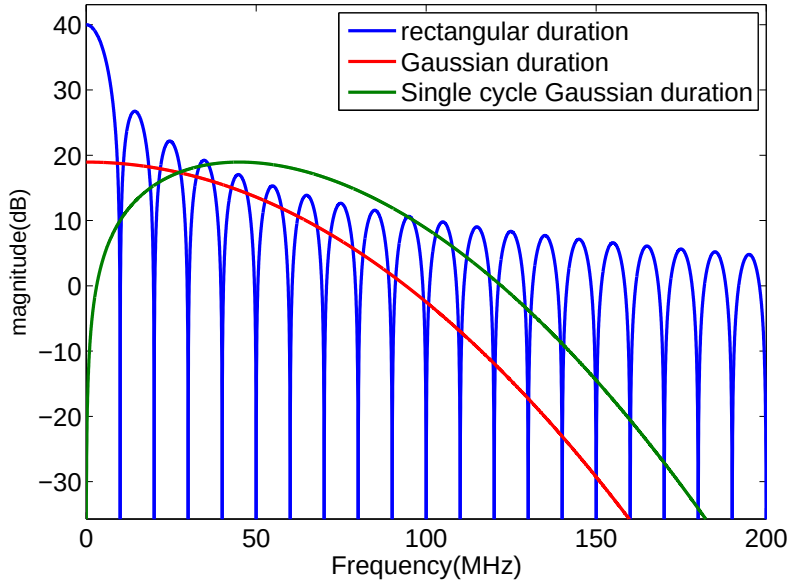

Figure 3.13: Power spectrum of rectangular Gaussian and single cycle Gaussian pulse signals

singles concentrate on the low frequency part. However, the single cycle Gaussian pulse contributes a bandpass window, where the frequency response moves towards a higher frequency center. Both the Gaussian and single cycle Gaussian pulse generate a wider bandwidth than the rectangular pulse. As we all know, the smaller the pulse time duration, the wider the frequency band, and the lower the whole magnitude level. By tuning the duration time, the largest magnitude at our interested frequency range (60 MHz) can be only 20 dB compared to the power spectrum of sinusoidal burst single shown in Fig. (3.14) 60 dB. Therefore in order to gain the same size of vibration as sinusoidal burst input, the other input should has a amplitude of 100 V which will kill the device due to the feedthrough effect.

As a result, for 66 MHz high frequency MEMS resonator, the small output mechanical vibration and the big capacitive feedthrough effect determine that the other types of pulse signals are not applicable in this case, and the only option is the sinusoidal burst.

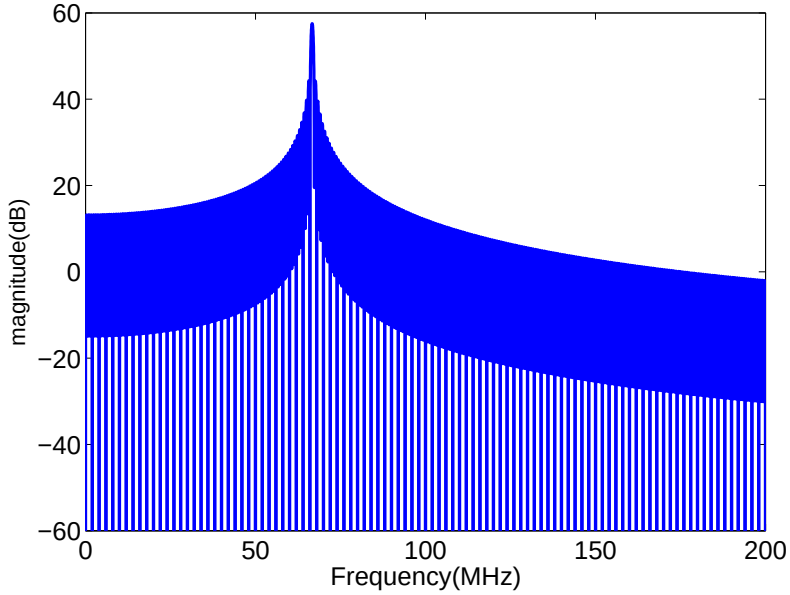

Figure 3.14: Power spectrum of sinusoidal signal

3.4 Summary

In this chapter, we compared the four measurement setup. The one port and two port configurations are widely used for their simply setup. While mixing and differential configurations are more efficient for illuminating the parallel capacitor and driving the resonator respectively. In frequency sweep measurement, parallel capacitor largely increases the frequency noise which is fatal for mass sensing application. Therefore we considered the two compensation technique, tunable capacitor and identical resonator pair. However, in our proposed pulse mode measurement setup, parallel capacitor disappears immediately at the release of excitation small signal, therefore has no impact. Other pulse signals besides the sinusoidal burst one are not suitable for MEMS bulk disk resonator since they have a low stimulation efficiency at resonance and the conclusion is the sinusoidal excitation is the only candidate.

Chapter 4

Measurement

In this chapter, in order to prove the theoretical predictions of Chapter 3, different measurement methods are conducted on both the disk and LBAR resonators. First the frequency sweep method is utilized to measure the resonant frequency and Q factor of disk resonator with one port and two port configurations. Then two methods are employed with both the tunable capacitor and identical disk devices pair. Afterwards, the pulse mode is also applied on a disk resonator for measuring the resonant frequency, Q factor and parallel capacitor measurement simultaneously. The measured results are compared with the results from frequency sweep setup. Finally, a Labview programme and a controllable gas setup has been developed, continuously tracing these three parameters and humidity sensing is demonstrated with pulse mode on both disk and LBAR devices.

4.1 Device Layout

The disk resonator is fabricated using polysilicon on a 5 μm thick PECVD oxide layer. Fig.(4.1(a)) presents the perspective schematic of the disk resonator which consists of a disk suspended above the substrate with a single anchor. Two electrodes surround the perimeter of the disk are separated from the disk by a narrow air gap that defines the capacitive electromechanical transducer of the device. The LBAR shown in Fig.(4.1(b)) is fabricated using the same process but with the longitudinal shape. The geometry and corresponding mechanical

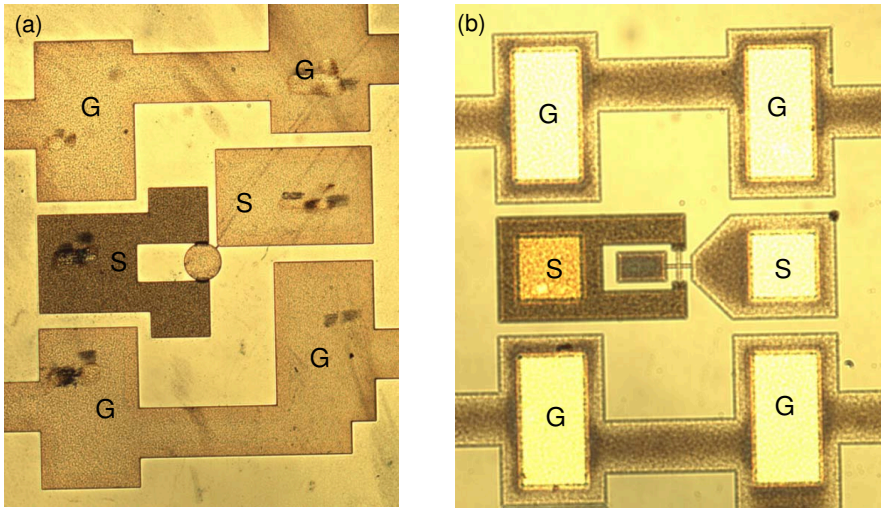

Figure 4.1: SEM image of device used for measurement (a) disk resonator (b) LBAR. Fabricated by Phd student Alberto Cagliani from DTU nanotech.The signals electrodes (S) are shielded from both sides by grounding pads (G).

Disk	R	W	t	d	f_0	Q
	$30\,\mu$m	$31\,\mu$m	$2.7\,\mu$m	120 nm	66 MHz	4000
LBAR	L	W	t	d	f_0	Q
	$70\,\mu$m	$2.5\,\mu$m	$2.7\,\mu$m	120 nm	30 MHz	4000

Table 4.1: Parameters of disk resonator and LBAR .For disk R is the radius of the disk and W is the effective coupling area, For LBAR L is the length and W is the width of the beam. t is the thickness, d is the gap distance, f_0 is the resonant frequency and Q is the approximate Q-factor.

parameters of the disk and LBAR devices used for measurement are listed in Table(4.1) and the measurement facilities used are shown in Appendix A.

4.2 Frequency Measurement

The frequency response is conducted with a network analyzer which does a frequency sweep and measures the gain and phase within the frequency domain. Fig. (4.2) shows the measured frequency response of the disk resonator for one port and two port setup. The results are quite consistent with the theoretical prediction. The measured results from the two port setup demonstrated more noise since the two port setup generates a lower signal than one port setup. On the other hand, the parallel capacitor of the two port setup is smaller than the one port setup, therefore, the frequency interval between peak and anti peak introduced by the parallel capacitor is also larger. However, in both cases, the parallel capacitors are too large and cover the motional output (peak antipeak heights are only around 1dB). The compensation technique is necessary in these two measurement setup to improve the frequency noise.

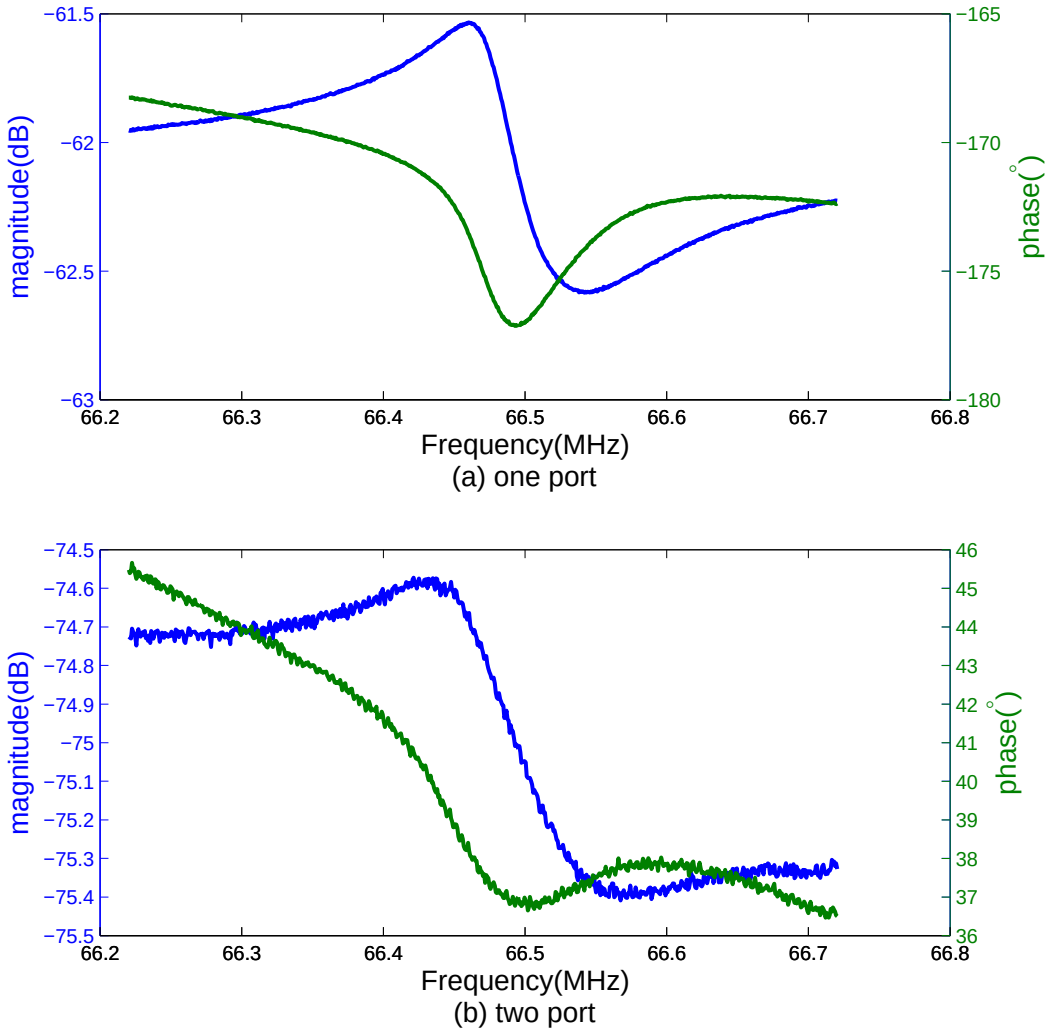

Figure 4.2: The measured frequency response of the bulk disk resonator (a) one port setup (b) two port setup

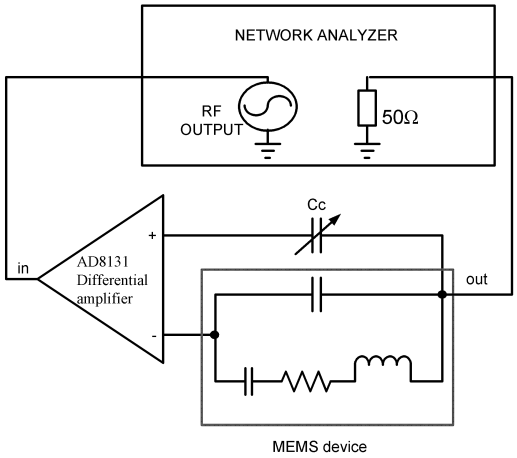

Figure 4.3: The frequency sweep measurement setup with tunable capacitor compensation employing a differential amplifier.

4.3 Parallel Capacitor Compensation Measurement

4.3.1 Tunable capacitor

As shown in Fig. (4.3) [71], a fully differential amplifier is used to generates two outputs with the same amplitude but 180° phase shifted, one output is connected to the MEMS part, while the other is connected to the tunable capacitor C_c. By tuning the capacitor, the transmission curve is changed. When C_c is tuned towards the parallel capacitor C_p, the anti resonance starts to decrease. If C_c is larger than C_p, making the whole system inductive and the anti resonance comes at the left side of the transmission curve. When C_c is exactly equals to C_f, the anti resonance totally disappears. However, the tunable capacitors on the market do not have a high enough resolution (on the order of fF), therefore, the cancelation is not always precise with this configuration. Fig.(4.4) shows the best compensated results. Before compensation, the peak height is only around

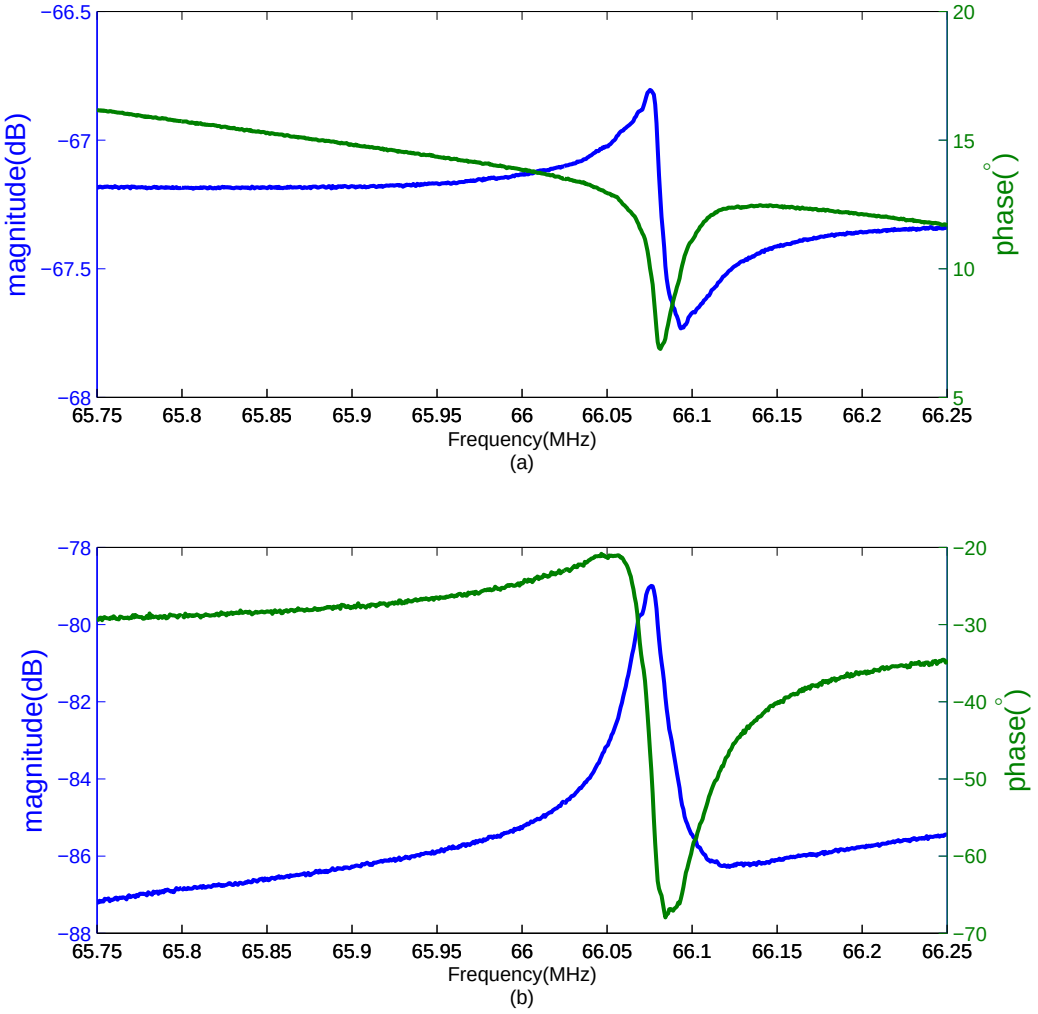

Figure 4.4: The frequency response of the bulk disk resonator showing the gain and phase around resonant frequency (a) without compensation and (b)with tunable capacitor compensation

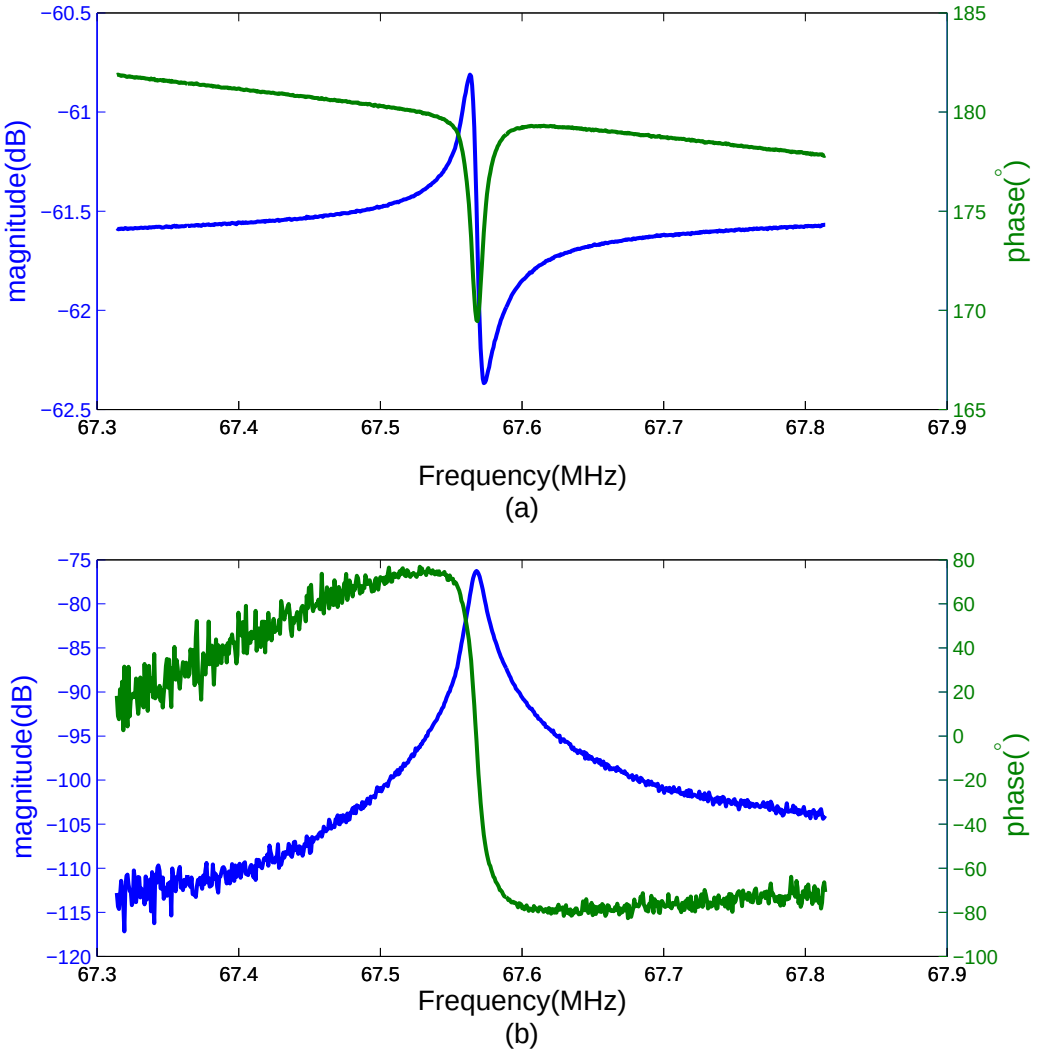

Figure 4.5: The frequency response of the bulk disk resonator showing the gain and phase around resonant frequency (a) single device without compensation (b)with two resonators where one has a DC bias and the other does not.

	parameters	$\delta\phi$	$\delta\phi/\delta f$	δf
device 1	no compensation	$0.25\,^\circ$	$8 \times 10^{-4}\,^\circ$/Hz	300 Hz
	capacitor comp	$0.5\,^\circ$	$4.5 \times 10^{-3}\,^\circ$/Hz	100 Hz
device 2	no compensation	$0.25\,^\circ$	$2.5 \times 10^{-3}\,^\circ$/Hz	100 Hz
	identical comp	$0.25\,^\circ$	$0.25\,^\circ$/Hz	1 Hz

Table 4.2: Phase noise $\delta\phi$, phase gradient $\delta\phi/\delta f$ and frequency noise δf of the no compensation, capacitor compensation and identical pair compensation.

1 dB while after compensation, the peak height is increased to 7 dB.

4.3.2 Two MEMS devices

Fig. (4.5) shows the measured results with two identical MEMS disk resonators, with one device DC charged and the other without DC charging. The compensated results are even better than the tunable capacitor compensation. The anti resonance is totally canceled leaving only the single resonance peak and the phase shift at resonance is linear which is important for the accuracy of measured resonant frequency.

4.3.3 Comparison of frequency noise

Table (4.2) compares the results of no compensation, capacitor compensation and identical device pair compensation. The device used for each compensation technique is slightly different from each other. In the capacitor compensation setup, the phase gradient $\frac{\delta\phi}{\delta f}$ is five times of the value without compensation. In the identical compensation setup, the increase of phase gradient is even more, up to 100 times of the value without compensation. In addition the phase noise $\delta\phi$ doesn't changes during identical pair compensation while it doubles during the capacitor compensation when extra electronics are included in the setup. The over all frequency noise δf is one third after the capacitor compensation while it is one hundredth after the identical device pair compensation. Therefore, the identical pair compensation is more efficient therefore is better for oscillator readout circuitry.

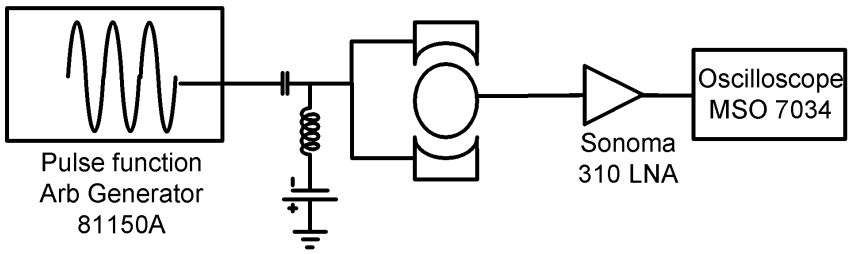

Figure 4.6: The burst mode measurement setup.

4.4 Sinusoidal Pulse

4.4.1 Measurement setup

The burst mode setup is shown in Fig. (4.6), where a pulse function arbitrary generator ($81150A$) is used to generate the sinusoidal burst signals. We use the one port measurement setup which has the largest parallel capacitor, therefore, the benefit of burst mode is more outstanding. The burst excitation is coupled to the two parallel input electrodes surrounding the resonator, which results in an effective excitation voltage $2V_{AC}$. The output signal is directly measured at the disk where a Sonoma 310 Low Noise Amplifier is utilized to amplify the weak output signal. The input impedance of the amplifier is 50Ω and the gain is very flat $32dB \pm 1.5\,\mathrm{dB}$ over a wide range $9kH - 1GHz$. The output voltage is then measured with an oscilloscope MSO 7034.

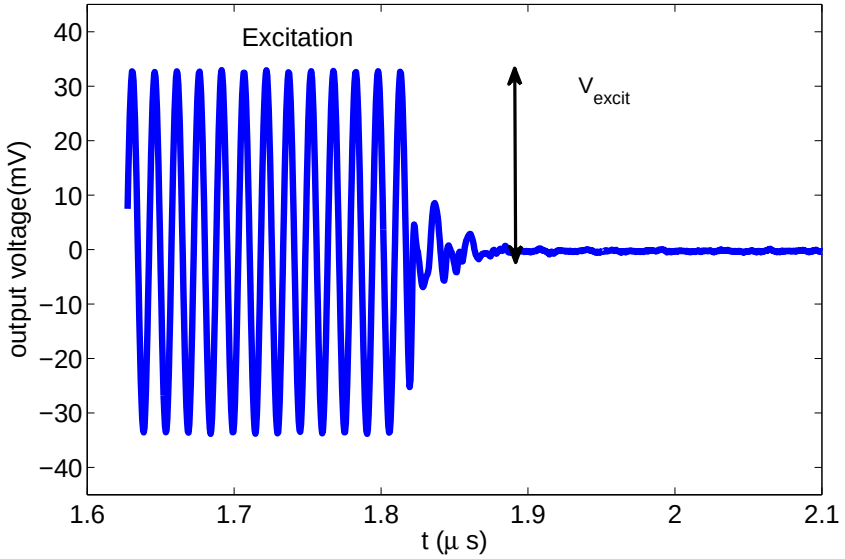

Figure 4.7: The transient response during the burst mode technique.

4.4.2 Measured Time Transient Response

Fig. (4.7) and Fig. (4.8) shows the measured time transient response around the shut down point with $V_{DC} = 0V$ and $V_{DC} = 16V$, respectively. When the device has no DC charge, there is almost no response after the shut down of the AC excitation. On the other hand, when the device has a DC charge, the vibration during the excitation is large enough and lasts for a long time after the shut down of the AC excitation. As shown in Fig.(4.8) during free vibration, the disk vibration generates a considerable output current. With these data, resonant frequency, the parallel capacitor and Q factor can be measured simultaneously.

4.4.2.1 Resonant Frequency

The resonant frequency is measured by measuring the period of the output signal during the free vibration. In this case the average period is calculated to be 15.244 ns which give us a frequency of 65.6 MHz.The frequency error is within 500 Hz. It is important to highlight that even though the excitation frequency differs from the resonant frequency, the free vibration output signal will always

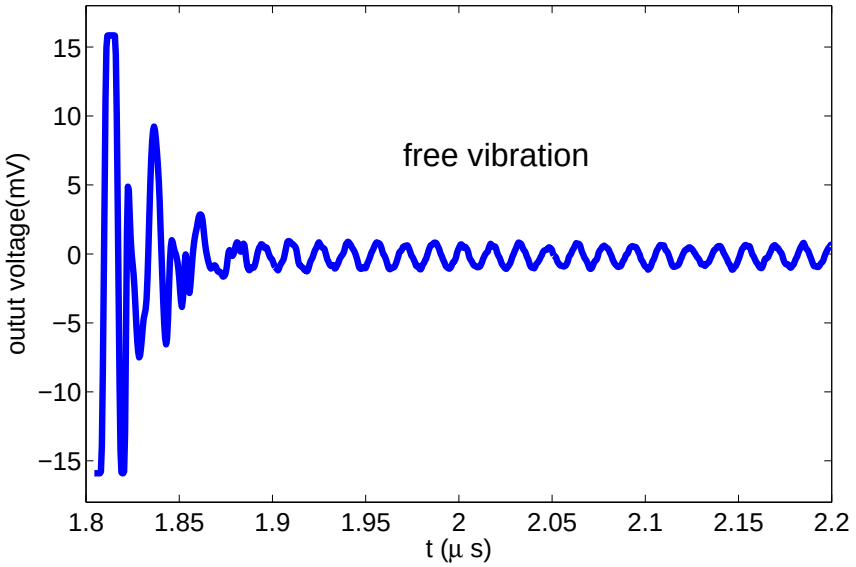

Figure 4.8: zoom in of time transient response around shut down point.

resonate at the resonator's resonant frequency.

4.4.2.2 Measured Parallel Capacitor

When the device is with DC charge,the voltage difference of the output at the end of excitation and at the start of free vibration totally comes from the contribution of the parallel capacitor.

$$V_{AC}\frac{R_L}{\omega_s C_f} = \frac{V_{excit} - V_{free}}{10^{32/20}} \tag{4.1}$$

where V_{excit} and V_{free} are magnitude of the time transient output voltage at the end of excitation and the beginning of free vibration; R_L is the loading resistance of oscilloscope, which is 50Ω. The calculated value of parasitic capacitor is $23fF$ which is quite consistent with the estimated theoretical value of 18 fF, the extra 5 fF is the parasitic capacitance.

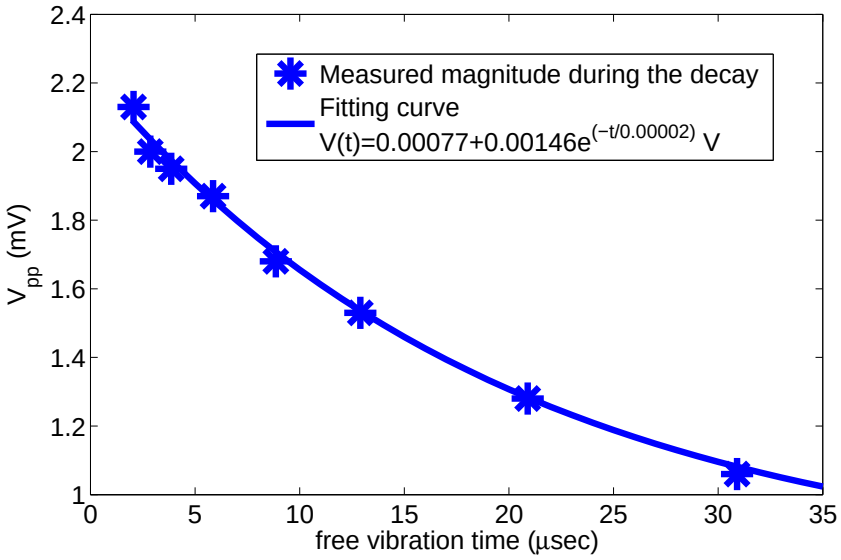

Figure 4.9: Measurement results of the decayed output voltage amplitude during free vibration when the excitation signal released at $1.8\mu s$.

4.4.2.3 Q Factor

Fig. (4.9) shows the decayed output voltage during free vibration when the excitation signal released at $1.8\mu s$. The time constant and the Q-factor deduced from the fitting curve is:

$$\begin{aligned} \tau &= 0.00002s \\ Q &= \tau\omega_0/2 \approx 4200 \end{aligned} \tag{4.2}$$

The Q factor is quite close to the value 4300 measured in the frequency setup method with Network analyzer, proving the accuracy of the technique.

4.4.2.4 Excitation Duration VS Vibration Amplitude

Fig.(4.10) plots the magnitude of the output voltage at shut down point versus excitation frequency for an excitation duration time of $1.5\,\mu$s and $7.5\,\mu$s excitation time duration, respectively. It is consistent with the theoretical predictions in Fig.(2.6). After a long excitation time of $7.5\,\mu$s, the magnitude of output

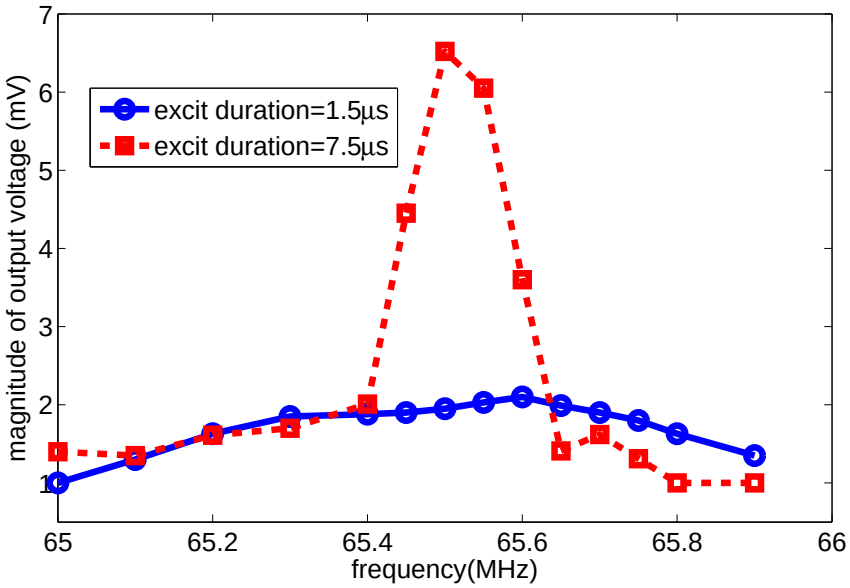

Figure 4.10: Measured output voltage magnitude at the end of short $1.5\mu s$ and long $7.5\mu s$ excitation duration, with change of excitation frequency.

voltage at the resonance 65.5 MHz is about 7 mV, when the excitation frequency differs from the resonant frequency by 100 kHz, the magnitude of the output voltage decreases by almost half, and by 200 kHz the signal is only 1/6 the original value. Therefore, the long time excitation technique can be only applicable for really small frequency changes. However, when the excitation duration time is short 1.5 μs, the magnitude of the output voltage is quite flat with excitation frequency. Within 500 kHz frequency deviation of excitation frequency from resonant frequency, the magnitude drop is within 50 percent out of 2 mV at the resonance, which is still a measurable value of our setup. The bandwidth (500 kHz) is the maximum range for a possible mass sensing applications.

4.4.2.5 Resonant Frequency VS Vibration Amplitude

Fig.(4.11) blue points plot the measured magnitude of the output voltage as a function of the excitation duration time at the disk's resonant frequency of $65.6MHz$ and AC voltage of $1.5V$. Compared to the theoretical curve (red one), the measured output voltage decrease at longer excitation time. It is a direct

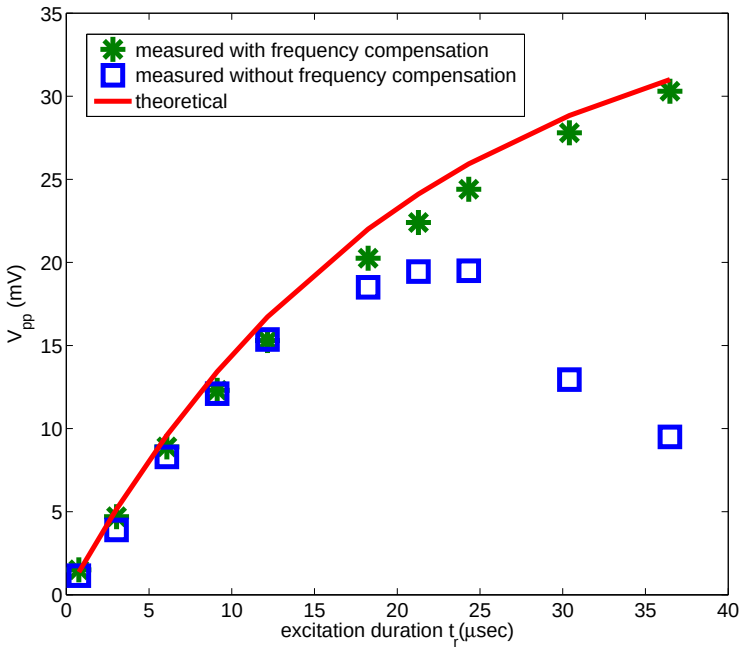

Figure 4.11: Measured output voltage magnitude at the end of excitation with change of excitation duration with and without frequency compensation

result of an odd-ordered nonlinearity in the capacitively transduced resonator's equation of motion, called electrostatic spring softening [72, 73]. The theoretical prediction in Fig.(2.5) shows that the vibration displacement of the disk is in the range of 6 nm at this moment, thus the electrostatic force gradient increases, lowering the effective spring constant and thus the resonant frequency of the disk resonator. When the disk resonator's resonant frequency deviates from the excitation frequency the magnitude of the vibration drops as is seen in the measurements.

In order to prove this theory the excitation frequency is tuned at each measurement to reach the highest output as shown in Fig. (4.11) green points. This curve matches the theoretical prediction in Chapter 2 Eqn.(2.39) much better than before, since we are compensating for the frequency drop due to spring softening. Furthermore, by plotting the corresponding excitation frequency, as in Fig. (4.12) the excitation frequency is seen to decrease as expected. The electro-

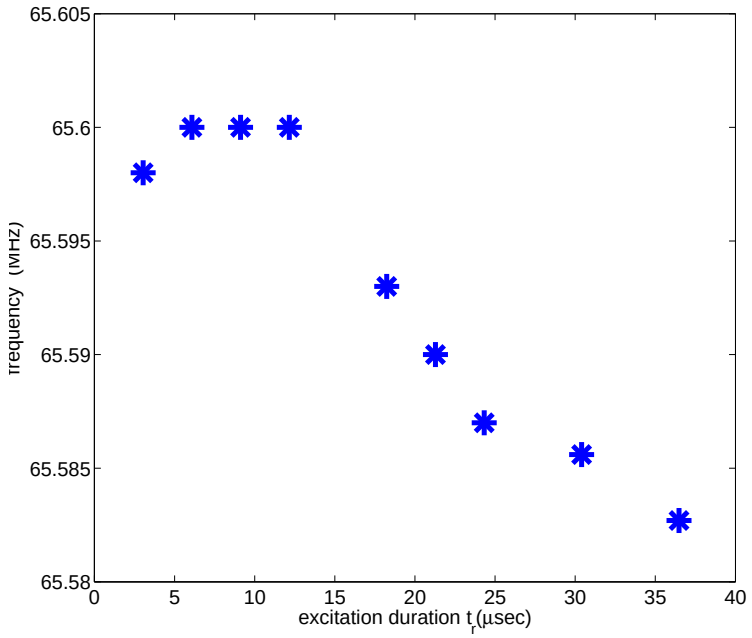

Figure 4.12: Corresponding resonant frequency used to reach the highest output voltage during the frequency compensation

static spring softening happens around 20 μs excitation duration, corresponding to a displacement of 6nm as in Fig.(2.5)). Therefore the most efficient excitation method is to use a short excitation duration time (1.5μs) and increase the AC voltage to reach the largest displacement within the linear region.

Fig. (4.13) shows the output voltage magnitude at the end of excitation with the change of AC amplitude under the same small excitation duration time of 1.5μs. The output voltage is proportional to the AC amplitude V_{AC} within the 300kHz bandwidth as expected, and the output voltage can be increased up to 7mV.

All the measured results prove the theoretical prediction of the pulse mode method. The next step is to continuously trace the resonant frequency, Q factor and parallel capacitor in real time.

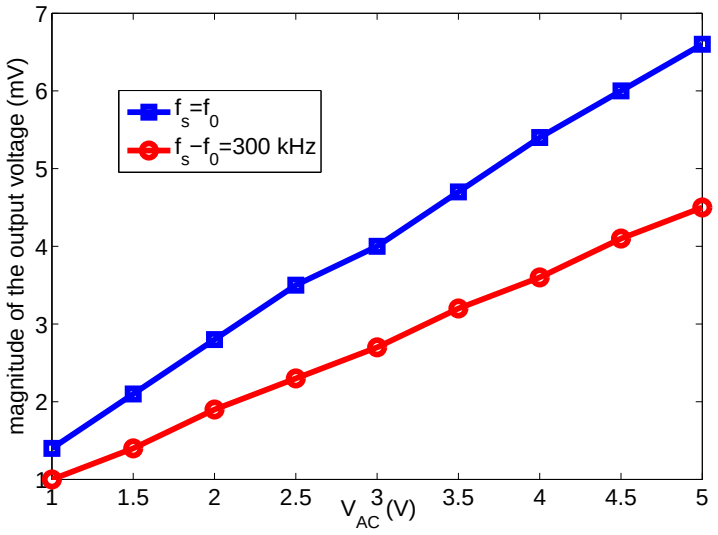

Figure 4.13: Measured output voltage magnitude at the end of excitation as a function of excitation amplitude. The excitation duration time is $1.5\mu s$

4.5 Data Acquisition and Processing with Labview

An automatic data acquisition and processing system can be achieved by Labview programme as shown in Fig.(4.14). The resonator is excited with the sinusoidal signal:

$$v_{ac} = V_{ac} \sin(\omega_s t) \tag{4.3}$$

for M cycles therefore the excitation time is:

$$t_{excite} = 1/f_s * M \tag{4.4}$$

as shown in Fig.(4.15). The oscilloscope measuring time (base time) is set to be t_s, therefore the whole data sequence is divided into evenly distributed sections with every section lasting t_s. The section number is:

$$n = t_f/t_s \tag{4.5}$$

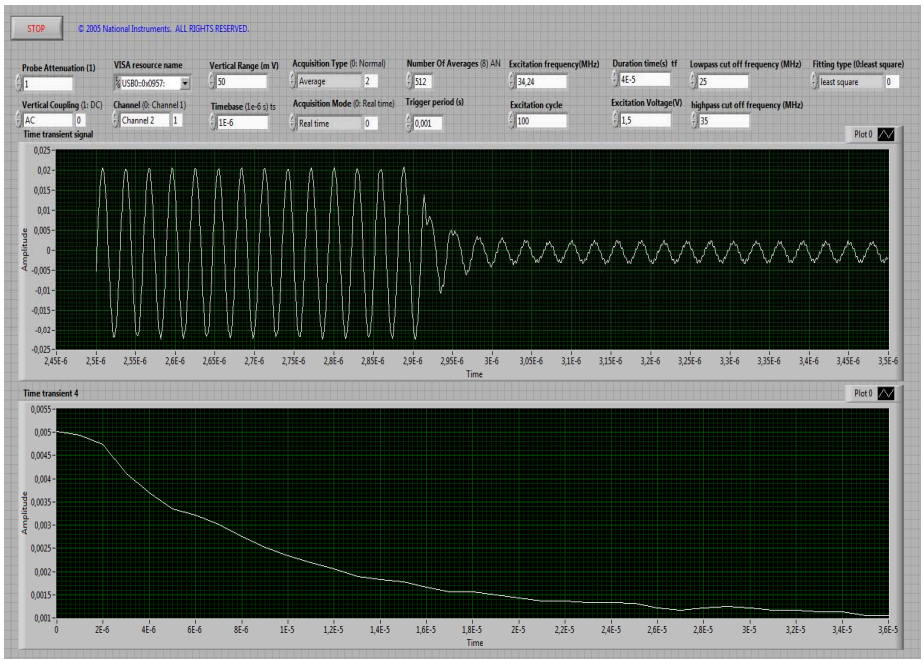

Figure 4.14: Front panel of the Labview programme for data acquisition. Indicate the control of the excitation signal, the acquisition type and time. The first graph shows the time transient response of every t_s while the second graph shows the amplitude decay curve during the whole free vibration time. The detailed programme is in Appendix B.

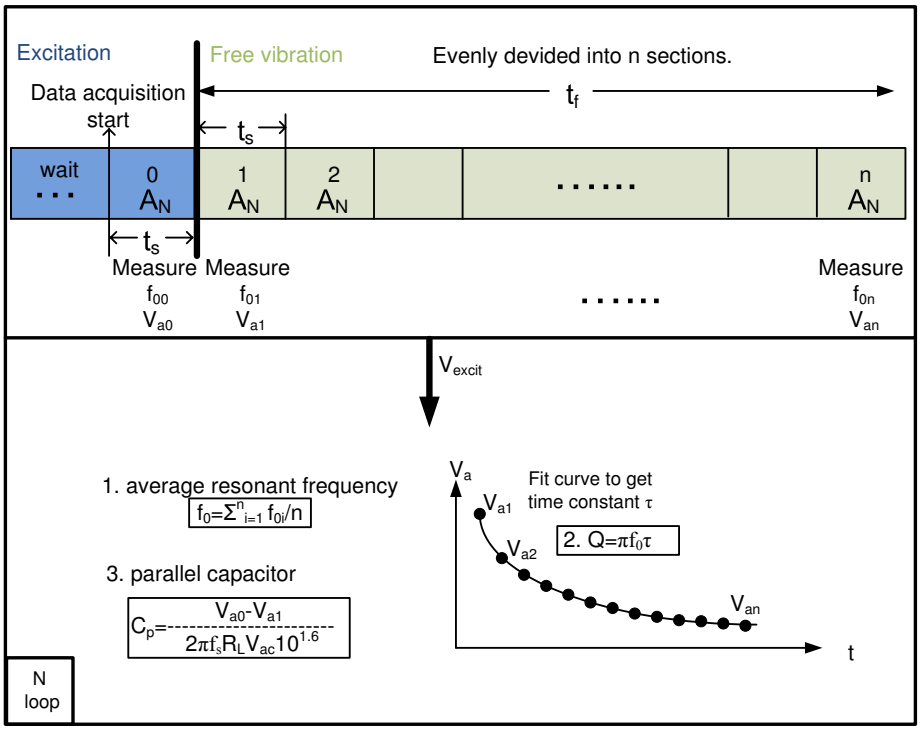

Figure 4.15: Data acquisition flow showing the excitation time, the free vibration time and oscilloscope measurement time base t_s. The free vibration time t_f and the average number per section A_N. The acquired data is going through further processing to calculate the resonant frequency, the Q factor and the parallel capacitor in real time.

where t_f is the whole free vibration time. The oscilloscope data acquisition type is set to 'average' which averages A_N points during each section. In order to calculate the parallel capacitor and thus the voltage drop at the shut down point, the last measurement before free vibration is also included which starts from time point $t_{excit} - t_s$. In every t_s, the programme records the measured curve and computes the frequency f_{0i} and the largest voltage amplitude V_{ai} of the section i.

After all the data acquisition, the measured frequency and voltage are going through further processing. First, the final resonant frequency f_0 is the average of all the measured frequency during free vibration

$$f_0 = \sum_{i=1}^{n} f_{0i}/n \tag{4.6}$$

Second, the measured amplitude sequence is imported into a curve fitting programme to find the time constant τ where:

$$Q = \pi f_0 \tau \tag{4.7}$$

Finally, the parallel capacitor is calculated using the Eq.(4.1).

The whole process is put together into a loop and repeated until stopped manually. The loop iteration is well controlled so the time interval can be tuned in different situation. Normally, we would like the system work continuously, so the time interval is zero. However, when the expected change of the output is very slower depending on the measurement, and it is not necessary to measure so often, we can then set the time interval to a larger number.

Here three parameters are important to highlight: t_s, A_N and t_f.

- The smaller the time interval t_s, the more accurate the acquired data but the larger the time consumption.
- The larger the average number, the more stable the acquired data, however the larger the time needed.
- The longer the free vibration time t_f the more data we can process, the more precise the Q factor. However, the data acquired at the very end is

Parameters/Features	speed	accuracy f	accuracy Q
t_s	proportional	inverse	inverse
A_N	inverse	proportional	proportional
t_f	inverse	inverse	proportional

Table 4.3: Parameters VS Features.

becoming smaller and smaller which influences the accuracy of frequency. Furthermore, it adds more time.

So there is a compromise between precision and speed shown in Table.(4.3).

After many times of experiment with resonators, by tuning the three data acquisition parameter values, the measured noise of resonant frequency and Q factor are shown in Fig.(4.16). Taking also the speed into consideration, we decided to use the t_s 1 μs, A_N 512 and t_f 10 μm. Then we are able to gain a frequency noise of 1 kHz for 66 MHz disk and 500 Hz for 30 MHz LBAR and a speed of 5 second per loop. The frequency noise measured from the frequency sweep method is 500 Hz for 66 MHz disk and 250 Hz for 30 MHz LBAR for a bandwidth of 100 Hz. The reason why for pulse mode measurement, the frequency noise is doubled is (1) the pulse setup introduces more electronic equipment thus increases the phase noise, (2) in order to increase the speed the accuracy of the frequency is sacrificed and (3) lack of a narrow band filter for data processing. The Q factor is dependent on the exponential curve fitting function that a small amplitude fluctuation will induce a large change in time constance thus the Q factor. Therefore, it displays more noise compared with the frequency. With this setup parameter, the Q factor noise is around $2-5$ percent.

Now we are able use this setup for real sensing application. An initial experiment is humidity sensing.

4.6 Humidity Sensing

The idea of humidity sensing is quite simple, to monitor the resonant frequency, Q factor and the parallel capacitor under the same room temperature and pressure but different humidity. A gas setup is necessary to control the humidity.

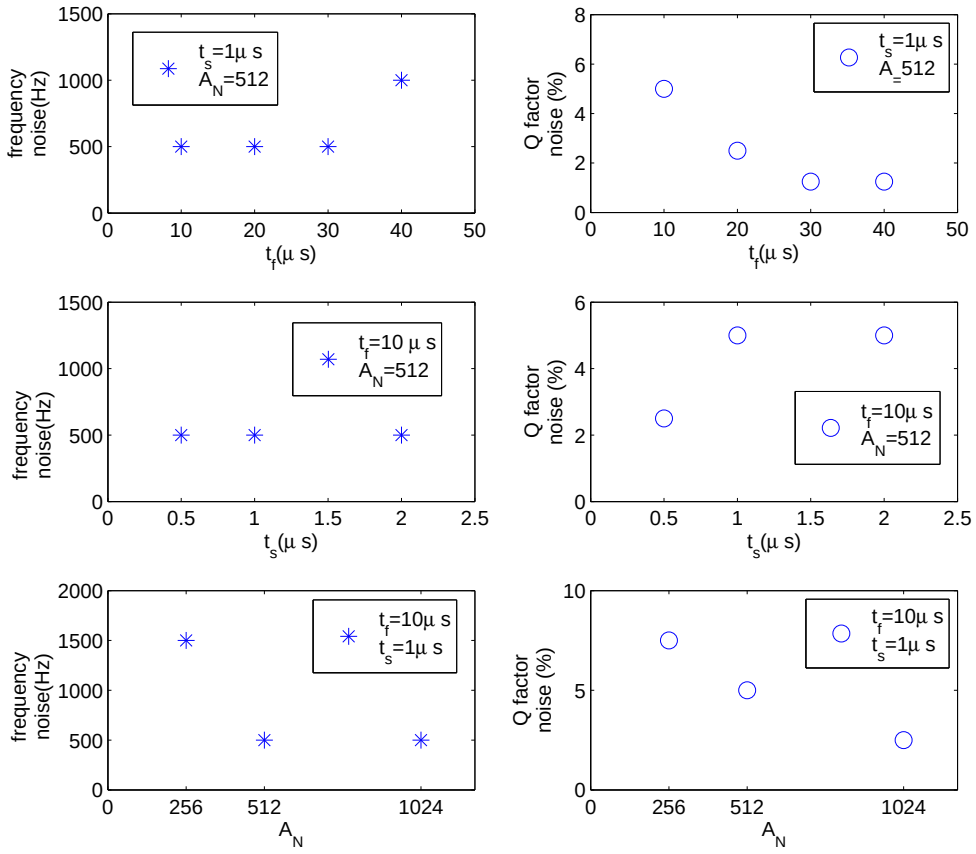

Figure 4.16: Measured frequency and Q factor noise according to different data acquisition parameters values of t_f, t_s, and A_N.

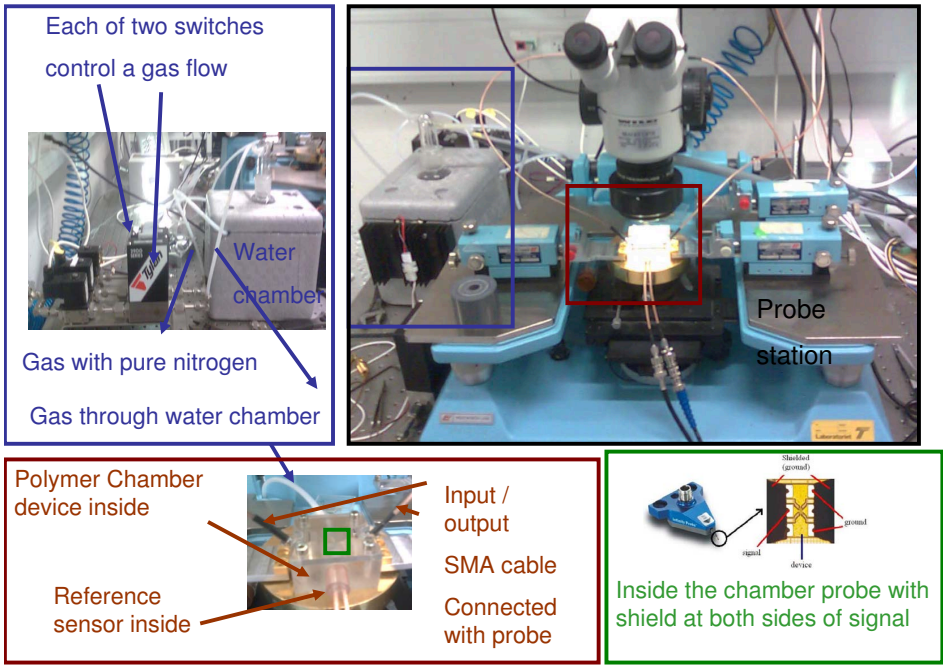

Figure 4.17: Gas system for the humidity sensing of MEMS resonators, including a controllable gas flow and a small polymer chamber to maintain the humidity from the room environment. This gas setup is built by Master student Jacob Rasmussen.

4.6.1 Gas System Setup

The gas system shown in Fig.(4.17). It consists of two valve, one of which is pure nitrogen and the other one is water flow as shown in Fig.(4.18). There is a switch inside each valve, so that we can determine how much the switches are opened thus tune the ratio of the flow from the two valve. Therefore, we can control the humidity. A polymer chamber is also included in this system to isolate the small area around the resonator and the probes from the room environment. Meanwhile we put a capacitive humidity sensor inside the chamber as a reference humidity sensor.

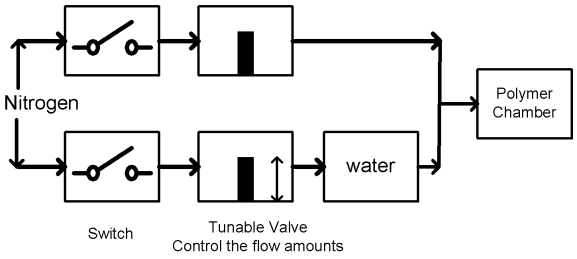

Figure 4.18: Gas flow diagram demonstrating the two switches and valves, one of which is used to control the amount of nitrogen and the other to control the gas through water chamber.

4.6.2 Measurement Results

Fig. (4.19) and Fig. (4.20) respectively shows the LBAR and the disk resonant frequency, Q factor and the parallel capacitor plot of time with the humidity quick jump between the highest and lowest value.

Resonant Frequency

The LBAR resonator responded quickly and linearly according to the humidity change. When the relative humidity changed between almost zero percent to 80 percent, the total resonant frequency change is around 4 kHz. However, disk resonator appeared a shift to a higher frequency with time. The possible reason could be from the surface cleaning. Because of the special back side etching of disk, the surface of the disk can contain some gold residues which are removed with the water vapor during the drop in humidity. Therefore, the total mass of disk is decreased and vibrating at a higher resonant frequency. The frequency change for disk is around 100 kHz at the maximum for a humidity change from 0-80 percent. The resulting humidity sensitivity is thus around $\sim$ 0.8 percent which is very high.

Q Factor

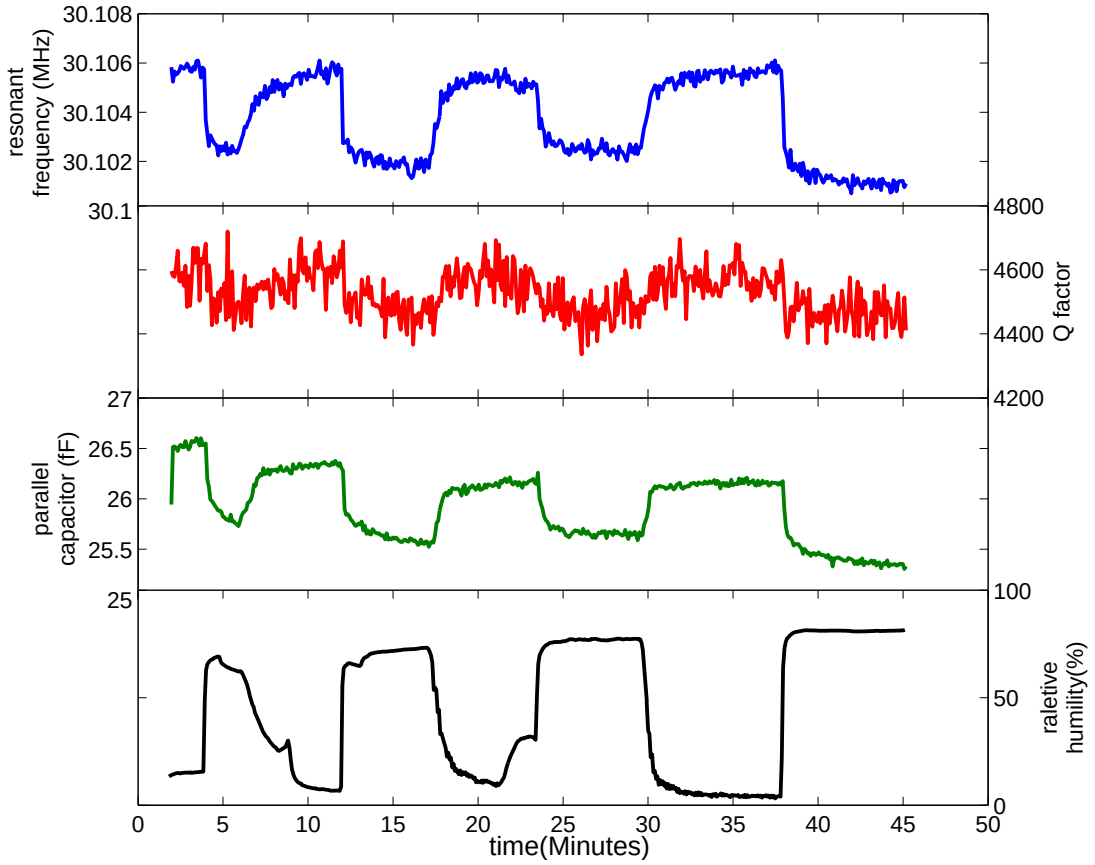

Figure 4.19: Pulse mode measured real time LBAR resonant frequency (Blue line), Q factor (Red line) and parallel capacitor (Green line) with the humidity change (Black line). The humidity changes quickly between 6 percent to 80 percent.

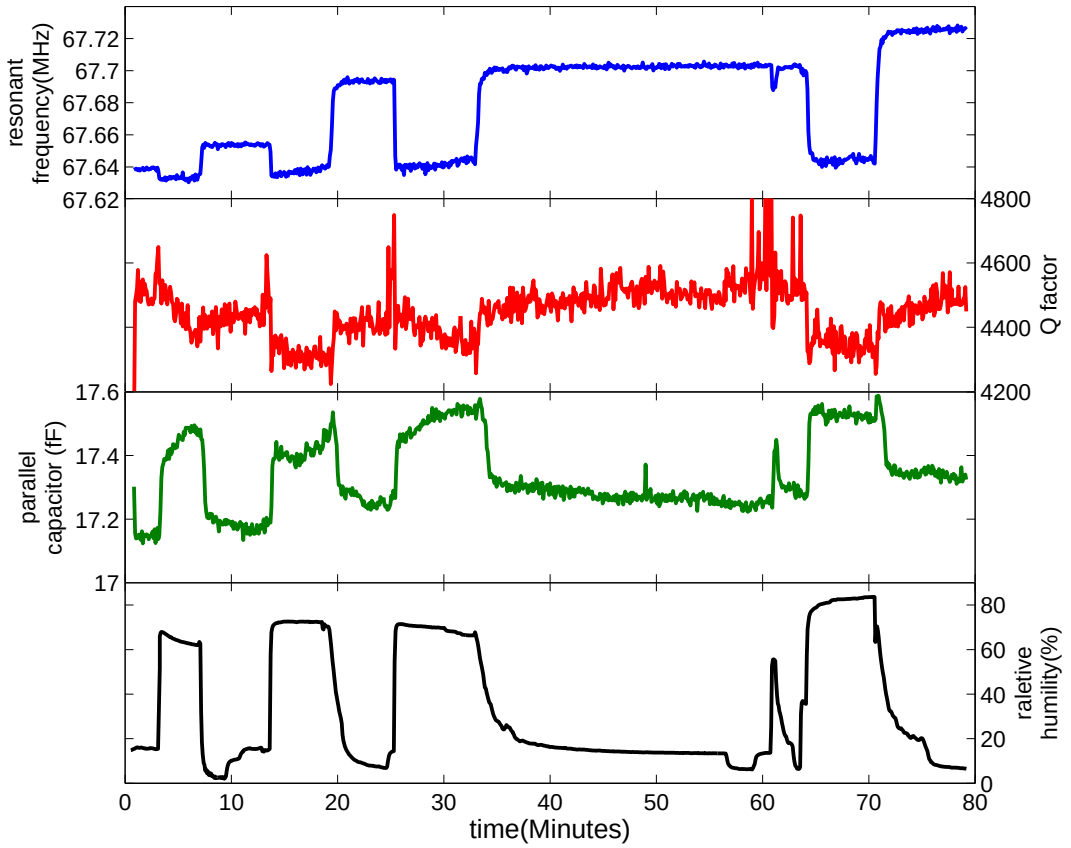

Figure 4.20: Pulse mode measured real time disk resonant frequency (Blue line), Q factor (Red line) and parallel capacitor (Green line) with the humidity change (Black line). The humidity changes quickly between 2 percent to 83 percent.

Due to the acquisition problem stated in last section, measured Q factor for both the LBAR and disk displayed a large noise but still it demonstrated a trend when the humidity increased the Q factor decreased which makes sense due to the more damping. The total change of Q factor is around 10 percent for LBAR and 5 percent for disk. The noise of the measured Q factor can be improved by using a better algorithm for exponential fitting for example calculating the slope at a fixed time.

Parallel Capacitor

The most interested phenomenon is that the measured parallel capacitors of LBAR and disk resonator demonstrate different tendency to humidity change. When humidity increased the parallel capacitor of LBAR decreased while the parallel capacitor of the disk resonator increased. As is stated in Chapter 3, the total parallel capacitor is:

$$C_p = C_f + C_{parasitic} \tag{4.8}$$

while the feedthrough capacitor is:

$$C_f = \frac{\epsilon_0 \epsilon_r w t}{d + x} \tag{4.9}$$

where ϵ_r is the relative permittivity. Table(4.4) lists for both LBAR and disk the total parallel capacitor C_p from measurement, the feedthrough capacitors C_f calculated with the device geometry and the parasitic capacitor $C_{parasitic}$ as subtraction result of the former two values.

The feedthrough capacitor of LBAR is much smaller than the disk, because it has a smaller coupling area w. While the parasitic capacitor of LBAR is much larger than disk. The possible explanation relies on the special layout of LBAR shown in Fig.(4.1(b)). The anchoring pad which is at the same time connected to the output pad is surrounded by the two input pads, therefore, the electric field is very strong in between and thus contributes to a higher parasitic capacitor. While disk resonator doesn't have this problem since the input and output pads are separated far away from each other.

When the humidity increased, two independent and competing processes are

(fF)	C_p	C_f	$C_{parasitic}$
LBAR	26	5	21
Disk	17.5	12.5	5

Table 4.4: Capacitors of LBAR and Disk resonators

occurring. The water vapor starts to fill the gap, increasing the relative permittivity ϵ_r and thus increasing the feedthrough capacitor; on the other hand, the increasing relative permittivity at the surrounding area deceases the electric filed E according to the Maxwell equation $\bigtriangledown E = \rho/\epsilon_0\epsilon_r$ (ρ is the charge density)[74] thus decreasing the parasitic capacitor. Therefore, whether the total parallel capacitor increased or decreased depends on the ratio of the feedthrough and parasitic capacitor. The LBAR has a larger parasitic capacitor and the decrease of this capacitor seemed to dominate the increase of the feedthrough capacitor hence the total parallel capacitor decreases. The situation is just opposite in the disk resonator hence the total parallel capacitor decreases.

4.7 Summary

In this chapter, various measurement methods are successfully tested on disk and LBAR resonators. Frequency sweep measurement setup is built mainly with network analyzer. Both one port and two port measurement are conducted with disk resonator and the two port measurement shows a decrease in both signal and the parallel capacitor. Compensation structures with both tunable capacitor and identical disk pair have been applied with frequency sweep measurement and the identical disk pair shows a perfect compensation effect so that anti resonance is totally canceled. This is extremely important for precise measurement of the resonant frequency for example with self sustain loop circuitry where we saw an improvement in the frequency noise by a factor of 100. Afterwards, pulse mode measurement setup has been built mainly with a signal generator and oscilloscope. The time transient response of the outputs are used to calculate the resonant frequency, the Q factor and the parallel capacitor. The measured results are compared to the results from frequency sweep method and they are

quite consistent to each other, proving the accuracy of the pulse mode method. A Labview programme has been designed to continuously trace the three measured parameters which indicates a possibility of real time application. A gas setup with polymer chamber and gas valves has been built up to well control the flow of water vapor thus the relative humidity. Both disk and LBAR resonators have been used for humidity sensing with pulse mode. The LBAR show consistent frequency and parallel capacitor changes whereas the disk resonator shows increasing frequency shifts with time, probably due to the surface contamination. Overall the disk devices performed best with relative shifts of 100 kHz with a humidity change of 80 percent, leading to a humidity resolution of ~ 0.8 percent, which is extremely good given that no polymer sensing layer has been implemented. Finally, differences in the measured parallel capacitance has been noted and a possible explanation has been given.

Chapter 5

Oscillator Circuit

In this chapter, an active filter tuned oscillator is designed for disk resonator. The oscillator's self-sustain configuration allows the continuously readout of the resonant frequency of the resonator. It consists of a parallel capacitor compensation circuitry, a multi-stage high gain high frequency amplifier, and a hysteresis comparator. The oscillator circuitry is designed and simulated with CMOS 0.18 μm technology. The behavior of the whole oscillator system is verified with Labview simulink. The physical layout of the circuitry is also displayed.

In the frequency response measurement setup, network analyzer is a must. This equipment requires a complicated circuitry which generates a range of frequencies, therefore is large size, expensive and impossible to be integrated into a small product in real application. However, in the time transient response measurement setup, signal with only one frequency is necessary. An integrated oscillator circuitry can achieve the single frequency synthesis.

5.1 Oscillator Overview

The basic structure of a sinusoidal oscillator consists of an amplifier and a frequency selective network connected in a positive feedback loop as shown in block diagram form in Fig.(5.1)[43]. In our case, the frequency selective network is MEMS resonator. The input, output, and feedback signals are x_s, x_o and x_f,

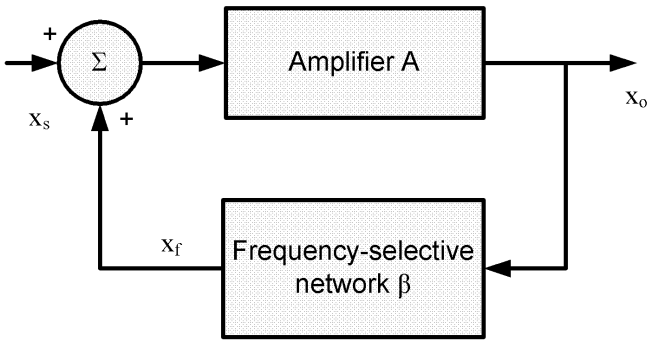

Figure 5.1: The basic structure of a sinusoidal oscillator.

respectively.

$$(x_s + x_f)A(s) = x_o \tag{5.1}$$

$$x_f = x_o\beta \tag{5.2}$$

Thus the transfer function with feedback is given as:

$$\frac{x_o}{x_s} = A_f(s) = \frac{A(s)}{1 - A(s)\beta(s)} \tag{5.3}$$

If at a specific frequency f_0 the loop gain $A\beta$ is equal to unity, the denominator of the Eqn.(5.3) will be zero which means the at this frequency, the circuit will have a finite output for zero input signal. Such a circuit is by definition an oscillator. The transfer function of the feedback loop of Eqn.(5.3) to provide sinusoidal oscillations of frequency ω_0 is:

$$L(j\omega_0) \equiv A(j\omega_0)\beta(\omega_0) = 1 \tag{5.4}$$

Barkhausen criterion: *at ω_0 the phase of the loop gain should be zero and the magnitude of the loop gain should be unity.*[43]

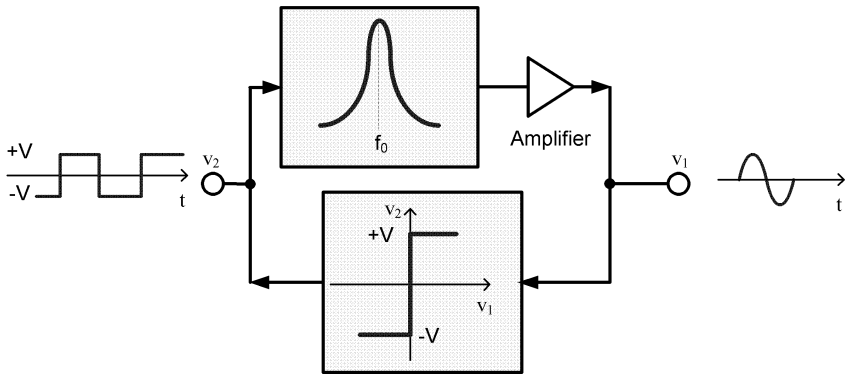

Figure 5.2: Block diagram of the active filter tuned oscillator.

To meet this oscillation criterion, there are a lot of oscillator types such as LC oscillator[75], Pierce oscillator [67] and so on. Among these, the simplest structure called the Active Filter Tuned oscillator is very suitable for our MEMS resonator.

5.2 Active-Filter Tuned Oscillator

Fig. (5.2) shows the principle of the Active Filter Tuned Oscillator. The MEMS resonator functions as a high $Q-$factor bandpass filter with a center frequency of the filter, the resonant frequency f_0. A hard limiter (or called a comparator/regulator) is connected with the MEMS resonator to form a positive feedback loop. During the oscillation, the sine-wave signal v_1 is fed to the comparator, producing a square wave output v_2 with frequency f_0 and voltage levels determined by the limiting levels. The square wave v_2 in turn is fed to the bandpass filter which filters out the harmonics and leaves only the fundamental output v_1 the sinusoidal wave with frequency f_0. The merits of this specific oscillator configu-

ration are:

- Simply structure and principle.
- Independent control of frequency, amplitude and distortion of the output sinusoid.
- Obviously, the Q factor of the MEMS resonator, rather than the other circuitry, determines the purity of the output sine wave. Therefore, high Q factor will lead to a low distortion of output sine wave.
- The frequency stability of the MEMS resonator, rather than the other circuitry, determines the frequency stability of the oscillator.

The phase of the square wave always jumps from 180° to −180°(fall edge) or reverse (rise edge), therefore, there is always a point in between which meets the Barkhausen zero phase criterion. As long as loop gain of the circuitry is larger than 1, it can oscillate. A pre-amplifier is included in this circuitry, since the MEMS resonator has a negative gain at resonant frequency. The power supply we are using it from zero to $+V = 1.8V$, so the phase of the square wave jumps from 0° to 180°. The phase delay from the amplifier,the comparator and the loading contact pad capacitor will supplement the other 180°. The detailed analysis will be explained below. The $0.18\mu m$ $CMOS$ technology is utilized in our design for high speed implementation.

5.3 Parallel Capacitor Compensation

In the active-filter tuned oscillator, the bandpass filter should have a single peak at central frequency. However, in MEMS resonator case, the parallel capacitor introduces an extra anti peak. Therefore, parallel capacitor compensation is required in the oscillator structure. As is illustrated in Chapter 3, we can either use two identical MEMS resonator device or a tunable capacitor to achieve the compensation. We would like to try both of the structure in our design. The first structure is simple while the tunable capacitor method is a little bit complicated

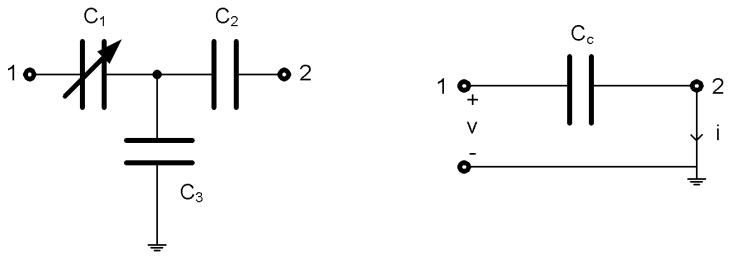

Figure 5.3: Capacitor down scale with a $T-$ structure.

since we would like the resolution down to 1 fF, otherwise, the influence of parallel capacitor is still considerable (detailed analysis with be demonstrated in the simulation results).

5.3.1 Capacitor Down Scale

The smallest size of commercially available capacitors is 100 fF, therefore a down scale structure is necessary as shown in Fig. (5.3).

A $T-$ structure with three capacitors are utilized. The equivalent capacitor C_c between port 1 and port 2 is calculated by applying a voltage source v across the two ports, and deducing the short circuit current i.

$$i = v \frac{\frac{1}{j\omega(C_2+C_3)}}{\frac{1}{j\omega C_1} + \frac{1}{j\omega(C_2+C_3)}} j\omega C_2 \tag{5.5}$$

therefore,

$$C_c = C_1 \frac{C_2}{C_1 + C_2 + C_3} \tag{5.6}$$

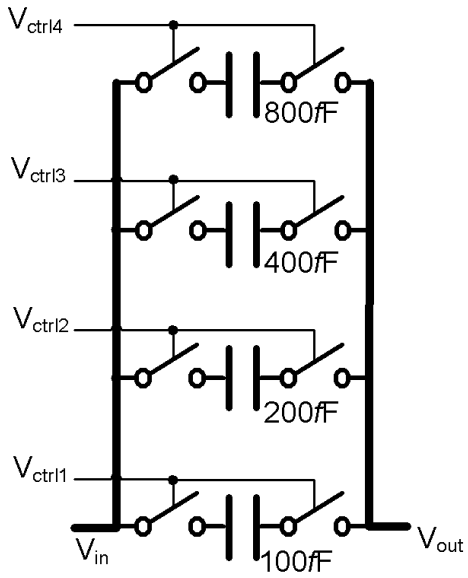

Figure 5.4: Variable capacitor array controlled by digital switch.

when $C_3 \gg C_{1,2}$

$$C_c \approx C_1 \frac{C_2}{C_3} \tag{5.7}$$

When C_1 is the smallest value 100 fF and $C_2/C_3 = 1/100$, the equivalent compensation capacitor is then 1 fF.

5.3.2 Capacitor Array

The variable capacitor C_1 can be achieved by an array of capacitors as shown in Fig.(5.4)

The switch array is utilized to control the selection of capacitors. When

V_{ctrli} is high, the corresponding capacitor is connected between input and output ports, otherwise, it is open circuited. The tunable range is from $100fF$ to $1500fF$ with a resolution 100 fF, corespondent to a $4-bit$ digital sequence of $[V_{ctrl4}, V_{ctrl3}, V_{ctrl2}, V_{ctrl1}]$ from [0001] to [1111]. As a result, the equivalent compensation capacitor C_c is from 1 fF to 15 fF with resolution 1 fF. In principle higher range can be achieved by increasing the control bits. However, at this time C_1 is large, and is comparable to C_3, the denominator of Eqn.(5.6) is larger and hence C_c is decreased. Therefore, we only use $4-bit$. 15 fF is sufficient for two port configuration (up to 10 fF) while for one port configuration (up to 30 fF) it is better to use identical resonator pair for compensation.

5.4 Differential Amplifier

As is illustrate in Chapter 3 Fig.(3.10), a differential amplifier is necessary for two aim:

- Pre-amplify the weak output signal from the MEMS resonator.
- Implement the subtraction of the parallel effect.

In order to design and simulate the circuit, equivalent circuit model, based on theoretical calculation and measurement fitting, is used with parameters:

$$C_x = 1.8\,\mathrm{a}F \tag{5.8}$$

$$L_x = 3.23H \tag{5.9}$$

$$R_x = 1M\Omega \tag{5.10}$$

The value of motional resistance used in simulation is little bit larger than in the real device (hundreds of $k\Omega$ depend on different Q factor value).By setting that, we can make sure the real output current is always larger than the simulation result and the designed circuit can work anyway.

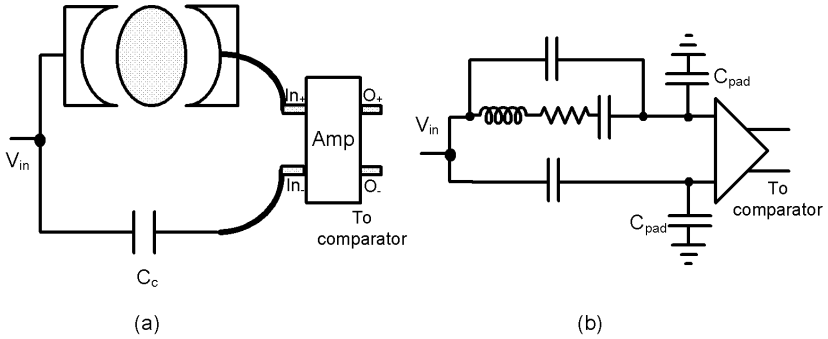

Figure 5.5: (a)Differential amplifier connected with MEMS and compensation capacitor (b)Equivalent circuitry model with load pad capacitor.

5.4.1 Contacting Pad Capacitance

Fig.(5.5(a)) shows the connection of the MEMS resonator and the compensation capacitor circuitry to the amplifier pads with wire bonding. Fig.(5.5(b)) demonstrates the equivalent circuitry while the two C_{pad} represent the contacting pad capacitance. The estimated value of C_{pad} is around $1pF$.The requirement of the amplifier could be summarized as follow points:

- High gain. According to the circuit structure in Fig.(5.5(b)),and assuming the parallel capacitor is totally compensated which means C_c is exactly equal to C_p, at resonant frequency, the differential input voltage between the input ports of amplifier will be:

$$V_{ind} = V_{in+} - V_{in-} = V_{in}\frac{\frac{1}{j\omega C_{pad}}}{\frac{1}{j\omega C_{pad}+R_x}} \approx V_{in}\frac{\frac{1}{j\omega C_{pad}}}{\frac{1}{R_x}} \tag{5.11}$$

  since $1/j\omega C_{pad} \approx 2.5k\Omega \ll R_x = 1M\Omega$.Therefore, for the unity input V_{in},

the differential input voltage of amplifier is:

$$V_{ind} = V_{in}\frac{2.5k}{1M} = 2.5mV \tag{5.12}$$

The minimal stimulate voltage for comparator is around hundreds of millivolt.This means the minimal differential gain of the amplifier should be around 100.

- High speed. It should be able to work at 66 MHz without to much phase delay. Normally, the oscillator circuit should totally have about 30° phase margin. According to the Eqn.(5.11), the pad capacitor C_{pad} performs as the load for MEMS, therefore, contributes 90° phase delay. As a result, the phase delay from amplifier and comparator will be in total $180° - 90° - 30° = 60°$. Let's split evenly, then the amplifier and the comparator could have 30° phase shift each.

- In summary, we need an amplifier with at least $40dB$ gain and at most 30° phase delay at 66 MHz.

5.4.2 Active Load

Fig.(5.6) shows the standard single stage differential amplifier configuration. The current source I_b is used to bias the amplifier. The gain stage is a common source topology differential $n-$MOS pair $M_{1\pm}$. $V_{in\pm}$ and $V_{o\pm}$ are input and output, respectively. The parallel R_L and C_L represent the load impedance. Using small signal analysis, the differential gain of this configuration is therefore:

$$A_d = \frac{V_{o+} - V_{o-}}{V_{in+} - V_{in-}} = \frac{2g_{m1}}{1/R + j\omega C_L} \tag{5.13}$$

The load impedance can be commonly achieved either by current mirror active loads as in Fig.(5.7(a)) or diode connected active loads as in Fig.(5.7(b)). With current mirror active loads, the corresponding loading resistance and capacitance are drain-source resistance and capacitance of $p-$MOS M_2:

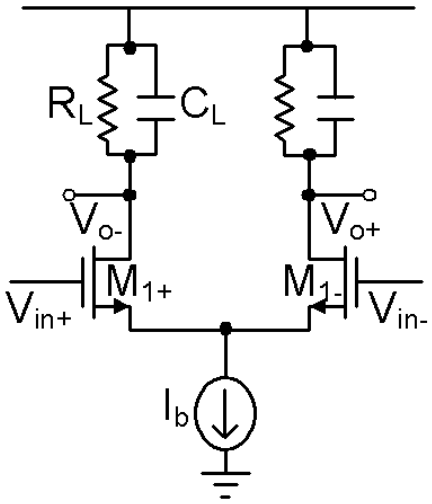

Figure 5.6: Standard single stage differential amplifier configuration with bias current I_b,differential input $V_{in\pm}$ and differential output $V_{o\pm}$

$$R_{Lmirror} = r_{ds2} \tag{5.14}$$

$$C_{Lmirror} = C_{ds2} \tag{5.15}$$

Both the resistance and capacitance in this case are high, therefore, contribute a high gain but a low speed.On the other hand, with diode connected active loads, since the drain and gate are connected together,the corresponding loading resistance and capacitance are the inverse of transconductance and gate-source capacitor of $p-$MOS M_3 :

$$R_{Ldiode} = 1/g_{m3} \tag{5.16}$$

$$C_{Ldiode} = C_{gs} \tag{5.17}$$

Both the resistance and capacitance in diode connected active loads are smaller than those in current mirror topology,therefore lead to a lower gain but a higher speed. What we are pursuing is high gain and high speed. The problem is how

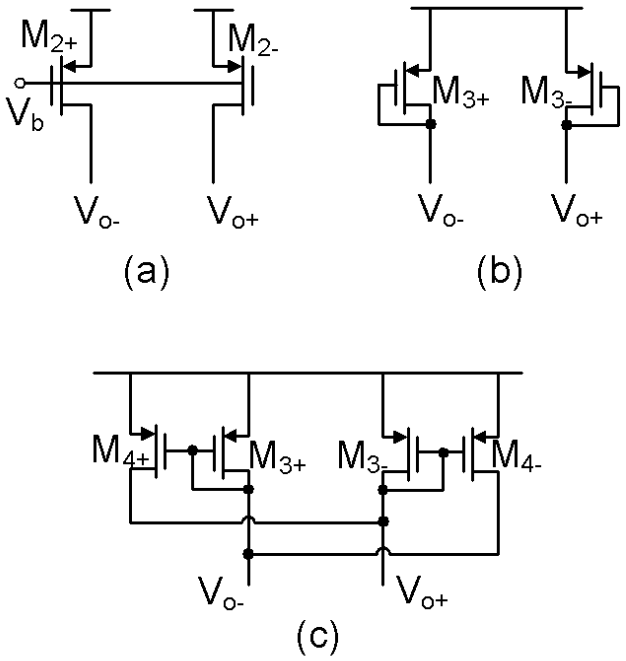

Figure 5.7: (a) current mirror active loads (b) diode connected active loads (c) cross coupling diode connected active loads.

to compromise between these two features. In our case, speed is the first consideration, and diode connected loads are selected. Fig.(5.7(c)) shows an improved cross coupling diode connected loads instead the single diode connected loads. The used of cross-coupled transistors allows us to precisely increase the loading resistance, without changing the over-drive voltage. The equivalent loading resistance is now:

$$R_{Lcross} = 1/(g_{m3} - g_{m4}) \tag{5.18}$$

while

$$g_{mi} = k_i(V_{GSi} - |V_{th}|) \tag{5.19}$$

while

$$k_i = \mu_p C_{op} W_i / L_i \tag{5.20}$$

V_{thp} is the threshold voltage of $p-$MOS and $V_{SGi} - |V_{thp}|$ is the overdrive voltage of transistor M_i. W_i and L_i are the width and length of the transistor M_i, respectively. For the sake of high speed, the length L_i of the loading transistors normally all uses the smallest number of the technology $L_4 = L_3$. In the cross coupling configuration, $M_{4\pm}$ and $M_{3\pm}$ has the same bias voltage V_G therefore,the cross coupling effect increases the resistance by a factor of

$$\frac{R_{Lcross}}{R_{Ldiode}} = \frac{W_3}{W_3 - W_4} \tag{5.21}$$

In principle, the larger the W_4, the smaller the $W_3 - W_4$, and the larger the gain. However, increase of W_4 also introduces a larger C_{ds4} as a loading capacitor, since $C_{ds} \propto W$.Therefore, usually W_4 is set to be half or two third of W_3, and the gain can be double or triple.In stead of the simple single stage differential amplifier, either using a cascode or multi stages configuration can achieve higher gain.

5.4.3 Cascode Configuration

Fig.(5.8(a)) shows the commonly used configuration for a single stage amplifier, a cascode configuration. Based on the simple differential amplifier in Fig.(5.6),

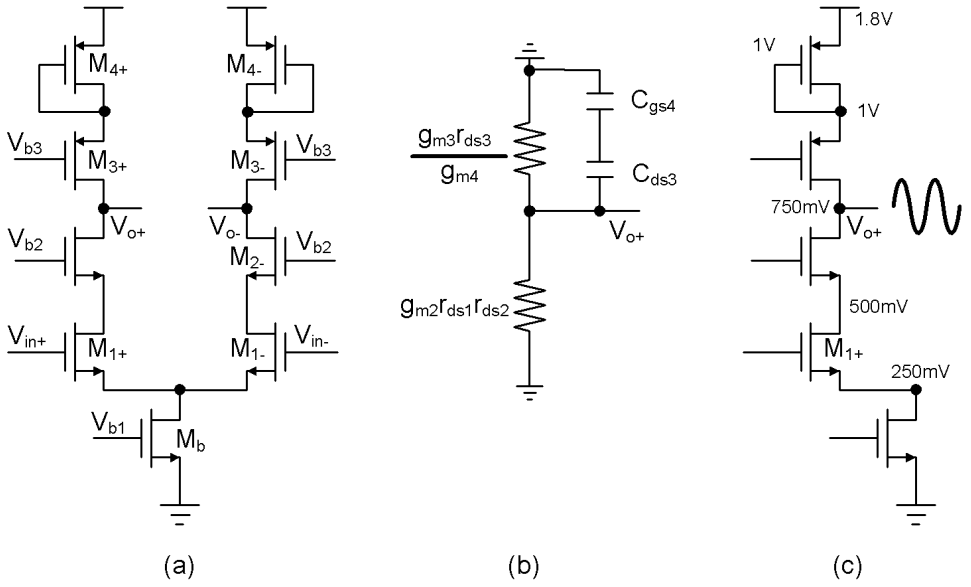

Figure 5.8: (a)single stage cascode configuration (b) Single side equivalent small signal resistance and capacitance model looking into the output node (c) voltage swing range available.

common-gate-connected transistor pairs M_2 and M_3 are inserted as cascade stages upon the gain M_1 and load M_4 transistor pairs. M_b is the bias stage which provide the bias current I_b. Fig.(5.8(b)) shows the single side equivalent small signal model at the positive output node. The output resistance looking into the drain of cascode transistors M_{2+} and M_{3+} are respectively given by:

$$r_{d2} \cong g_{m2} r_{ds2} r_{ds1} \tag{5.22}$$

$$r_{d3} \cong g_{m3} r_{ds3} / g_{m4} \tag{5.23}$$

since $1/g_{m4} << r_{ds1}$, the equivalent loading resistance is r_{d3}. Meanwhile both g_{m3} and g_{m4} are transconductance of $pMOS$ transistor, with similar dimension and saturation condition,

$$g_{m3} \approx g_{m4} \tag{5.24}$$

therefore,

$$R_L \approx r_{d3} = \frac{g_{m3}}{g_{m4}} r_{ds3} \approx r_{ds3} \tag{5.25}$$

is much larger than the load resistance $1/g_m$ with simple differential amplifier structure in Eqn.(5.16).At the same time, the cascode structure doesn't change the load capacitance, since the extra cascode capacitor C_{ds3} is connected in series with the original loading capacitance C_{gs4}.

$$C_L = \frac{C_{ds} C_{gs}}{C_{ds} + C_{gs}} |_{C_{gs} << C_{ds}} \approx C_{gs} \tag{5.26}$$

Therefore, the cascode configuration can provide a much higher gain without sacrificing the speed. It seems to meet our requirement,however, when we check the voltage swing range of the transistors as shown in Fig.(5.8(c)). In order to ensure that the transistors are operating in deep saturation, so that transconductance and speed of the transistors can sit in their highest region. The over drive voltage:

$$V_{dsat} = V_{GS} - |V_{th}| \tag{5.27}$$

should be larger enough. Normally, the value of V_{dsat} is set above $250mV$. Therefore, the saturation criterion $V_{ds} > V_{dsat}$ is applied for M_b, M_{1-3}. The output

voltage should be above $750mV$ from the $nMOS$ point of view. At the same time,the gate and drain of M_4 are connected together, so it is for sure working in saturation. The threshold voltage of $pMOS$ $|V_{thp}|$ is around $550mV$, therefore

$$V_{SG4} > V_{thp} + 250\,\text{mV} = 800\,\text{mV} \tag{5.28}$$

which makes $V_{G4} = V_{D4} < 1V$ and from $pMOS$ point of view output voltage should be below $750mV$. Evaluating from both $pMOS$ and $nMOS$, the voltage swing at output node is zero. As is demonstrated at the beginning of this chapter, the voltage swing we need is around 200 mV, therefore, the cascode configuration is not applicable for its small voltage swing.

5.4.4 Multi Stages

The only alternative is to use multiple stages of the simple configuration with cross coupling diode connected loads.The challenge relies on how to prevent the amplification of the DC bias voltage. For example, the input node of each stage is biased at $1V$ and the output node is biased at $1.2V$. Therefore, direct connection of the output of the ith stage to the input of the $(i+1)$th stage will lead to a dislocation of the biasing states. Therefore, DC block should insert between two consequent stages and external bias for input nodes of each stage is also required as shown in Fig.(5.9(a).) $V^i_{in\pm}$ and $V^i_{o\pm}$ represent the input and output voltage of the ith stage. A single series capacitor C_s functions as the DC block.DC single is separated while AC signal can still pass by. C_{in} and C_o represent the input output capacitor of each single stage amplifier. Therefore, according to the small signal analysis:

$$V^{i+1}_{in} = V^i_o \frac{C_s}{C_s + C_{in}} \tag{5.29}$$

therefore, when $C_s >> C_{in}$, $V^{i+1}_{in} \approx V^i_o$. At this time, the transmission loss of the small signal between two stages will be negligible.

The utility of DC block capacitor brings in an extra problem, that is how to bias the input nodes of each stages. The ideal way is to employ a resistor R_b with infinitely big resistance. Therefore, the input nodes are biased to the voltage source V_b meanwhile no small signal current leakage to voltage source. The

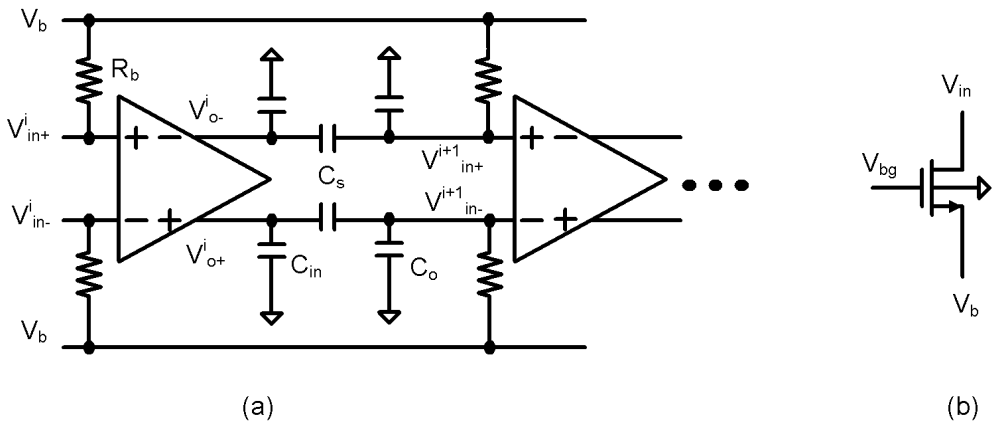

Figure 5.9: (a)DC block C_s between two neighboring stages and biasing for input nodes with infinite impedance R_b which is implemented by (b) weak inversion transistor configuration.

implementation of R_b could take use of transistors operating in weak inversion as shown in Fig.(5.9(b)). The source and gate nodes are biased with voltage source V_b and V_{bg}:

$$V_{GS} = V_{bg} - V_b \tag{5.30}$$

By setting the gate-source voltage very close to the threshold voltage V_{th}, the transistor is operating in weak inversion region.In addition, large length and smaller width are selected in order to minimize the leaking current:

$$I_d = \frac{1}{2}\frac{W}{L}\mu_n C_{ox}(V_{GS} - V_{thn})^2 \tag{5.31}$$

which induces a sub-pA drain current and almost zero drain-source voltage drop V_{DS}. Therefore, the drain voltage which is the input node of each single stage amplifier, follows the source voltage which is the bias voltage source.

5.4.5 Design Parameter and Simulation Results

Fig.(5.10) shows the width of the transistors for the single stage and operational DC voltage at bias nodes. For the sake of high speed and high gain, all the transistor working in strong inversion region have a minimal length of $260nm$. The cross coupling subtraction factor is two, which leads to widths of two identical pairs are $40\mu m$ and $20\mu m$,respectively. Biasing transistor pairs working in the weak inversion have a larger length of $960nm$ and smaller width of $5\mu m$.Four stages are utilized.

Fig.(5.11)shows differential gain and phase at the 4th stage amplifier, under the condition the parallel capacitor of the MEMS electrical model is totally compensated. At the resonant frequency, the differential gain is $-15\,\mathrm{dB}$. Therefore, a small signal input of magnitude $1\,\mathrm{V}$ applied on the MEMS resonator will generate a differential output magnitude of $178\,\mathrm{mV}$ which is sufficient to boost the comparator. Meanwhile, the phase shift at resonant frequency is 120° in which 90° is from the contacting pad capacitor C_pad and the rest 30° is the phase delay of the four stages amplifier. In conclusion, the amplification and the speed are appropriate for our MEMS resonator application. The total power consumption for amplifier is around $9\,\mathrm{mW}$.

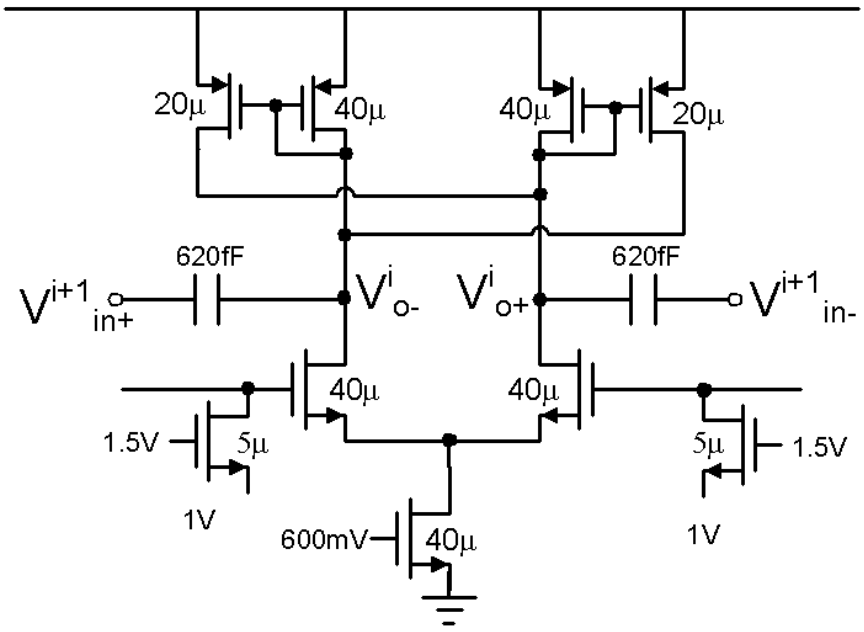

Figure 5.10: Width of the transistors for single stage and operational DC voltage at bias nodes.

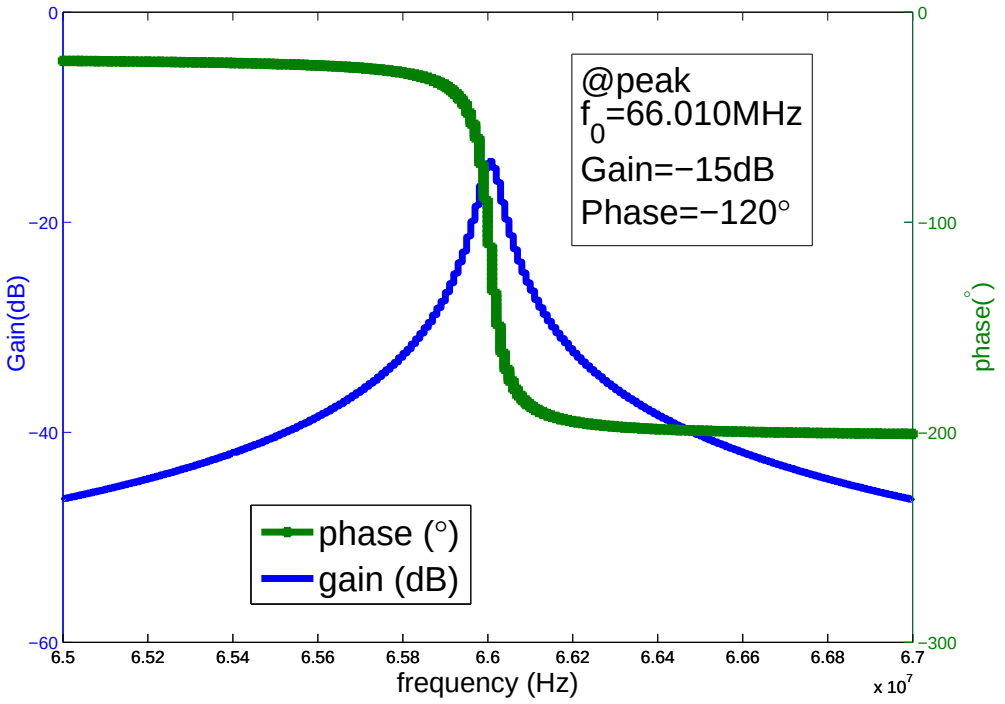

Figure 5.11: Differential gain and phase at the 4th stage amplifier, under the condition the parallel capacitor of the MEMS electrical model is totally compensated.

5.5 Hysteresis Comparator

Fig.(5.12) shows the function of the comparator. Black curve represents the ideal sinu wave, and blue one is the real signal with random noise such as thermal noise. Purple curve shows the square wave after a normal comparator which transfer all the positive signal to $+V$ and negative signal to $-V$. Because the real sinu wave with noise has some jitter around zero as shown with the green circles, there are extra noise peaks appearing in the purple curve. In order to remove this noise, we would like to utilize the special comparator called hysteresis comparator or called Schmitt Trigger(ST) comparator which act as a bistable circuit. In this case, the comparator no longer has a single threshold–zero, instead it has two thresholds $+V_s$ and $-V_s$ as illustrate as the red curves. In this case the comparator has memory. Not only the sinu wave but also the current state of the square wave determine the next state of the square wave. Therefore,

- Only when the square wave is positive, and when the sinu wave is smaller than $-V_s$,the square wave will drop to negative level.
- Only when the square wave is negative, and when the sinu wave is bigger than V_s, the square wave will jump to positive level.

Small changes between $[-V_s : V_s]$ will not induce the level change. The dark green curve shows the square wave after the hysteresis comparator and it is seen that the noise introduced by the jitter is totally removed.

5.5.1 Implementation of CMOS Differential Schmitt Trigger

Traditional Schmitt trigger [43] based on op-amps and resistive feedback suffer from limited speed and large power consumption. Such drawbacks are avoided in the CMOS based Schmitt trigger proposed by Dokic [76]. The topology was modified to accommodate different applications [77][78][79]. However, the afore mentioned Schmitt triggers are all single ended and have a hysteresis that is set by device dimensions, process parameters, supply voltage and varies with process conditions which makes them not particularly suitable for precision applications.

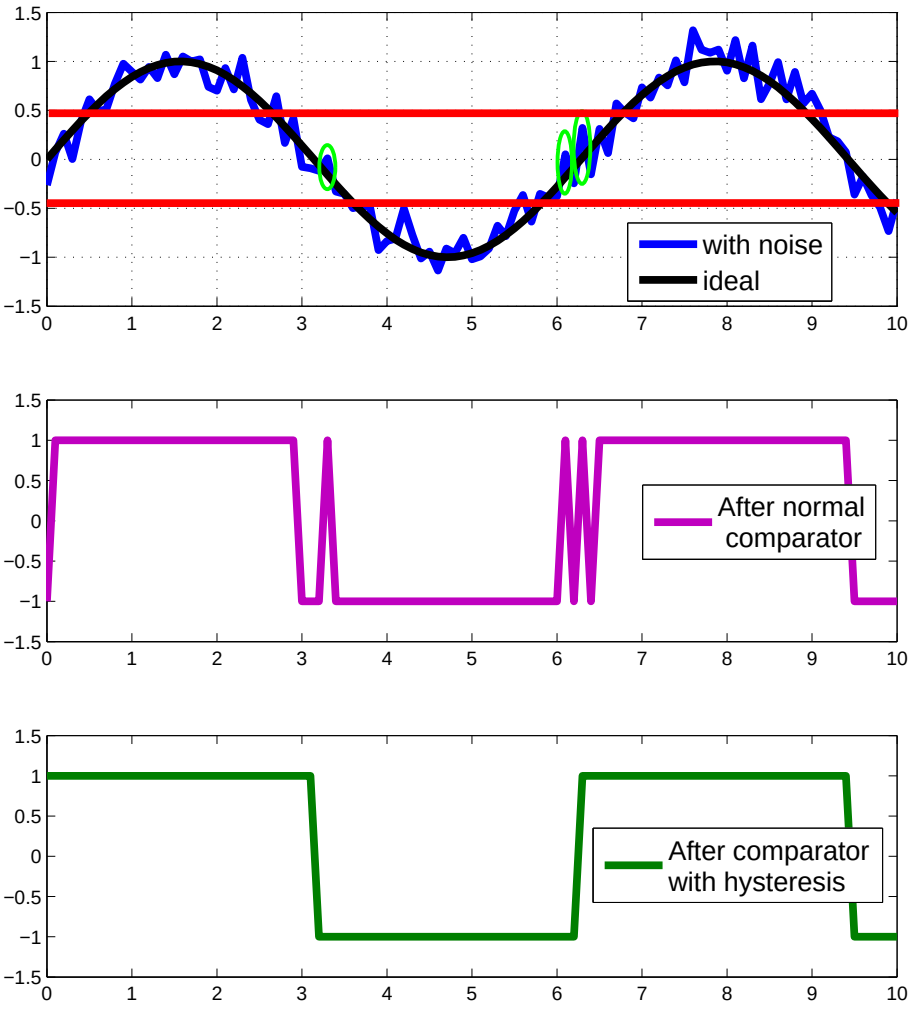

Figure 5.12: Function of the normal comparator and hysteresis comparator

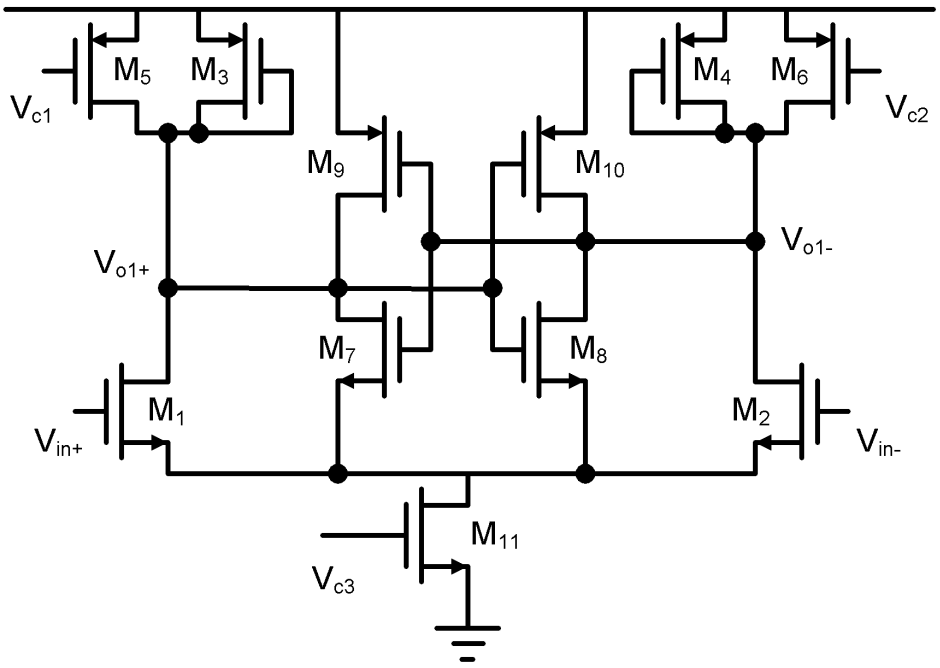

Figure 5.13: Yuan's fully differential Schmitt trigger with cross coupled static inverter.

Different Schmitt triggers offers better supply rejection and is more robust to process variations [80]. F. Yuan [81] added a cross-coupled static inverter pair to the conventional differential pair to make a differential Schmitt trigger, as is shown in Fig.(5.13) . This structure has an advantage of tunable hysteresis by the component ratio and over-drive voltage. However, to reliably turn on the inverter pair requires a voltage swing higher than $|V_{thp}| + V_{thn}$, which set a very large over-drive voltage over M_{3-4} and hence large power dissipation.

We propose a novel low-power differential Schmitt trigger design. Compared with Yuan's design, the proposed structure also features a precisely defined hysteresis, but requires a much lower overdrive voltage. As a result, the proposed structure consumes much less power, runs a higher speed and accepts input with much smaller swing.

5.5.2 Principle

We follow the main idea of Yuan to make differential Schmitt trigger, but with a modified positive feedback structure to accommodate smaller output swing as shown in Fig.(5.14). The modified feedback structure is actually a differential pair $M_{3\pm}$. To ensure $M_{3\pm}$ saturation during operation, an additional pair of cascode transistors $M_{2\pm}$ is employed to provide folded-cascode signal path. The loading network is actually a pair of diode-connected transistors $M_{4\pm}$ in combination with a pair of cross-coupled transistors $M_{5\pm}$.

The proposed structure can be modeled as a Differential-Difference Amplifier (DDA) with positive feedback, as is shown in Fig.(5.15), With this model, the transfer function of the proposed structure can be derived as:

$$\frac{V_{od}(s)}{V_{in}(s)} = \frac{G_{m1}}{sC_L + (G_L - G_{m3})} = \frac{G_{m1}}{sC_L + (G_{m4} - G_{m5} - G_{m3})} \tag{5.32}$$

where G_{mi} is the transconductance of transistor M_i, G_L is the conductance of the loading network, C_L is capacitive at the output node. The transfer function has a single pole located at:

$$s_p = (G_{m3} + G_{m5} - G_{m4})/C_L \tag{5.33}$$

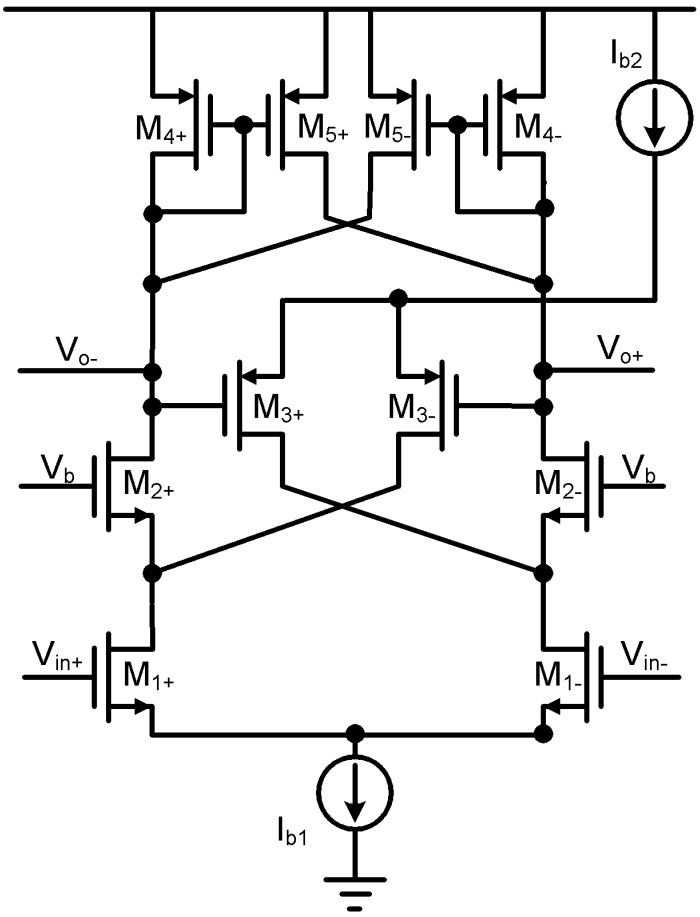

Figure 5.14: Schematic of proposed low power differential Schmitt trigger

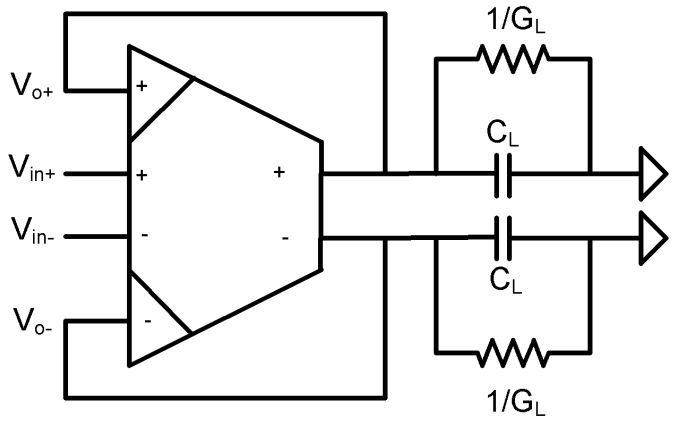

Figure 5.15: Analytical model of the proposed low power differential Schmitt trigger

.

- If $G_{m3} + G_{m5} < G_{m4}$, the pole lies in the left half plane, and the output shows a typical low pass behavior.
- If $G_{m3} + G_{m5} > G_{m4}$, the pole lies in the right half plane, leading to an exponential growing output with time constant $C_L/(G_{m3} + G_{m5} - G_{m4})$.

Based on the above observation, the detailed dynamics of the proposed Schmitt trigger can be revealed using the transconductance curve given in Fig.(5.16(a)). The transconductances of differential pair M_3 and loading transistors M_4 ,M_5 are functions of differential output:

$$V_{od} = V_{o+} - V_{o-} \tag{5.34}$$

They reach the peak values when V_{od} reaches zero, and slowly drop when V_{od} departs from zero.

- $G_{m4} - G_{m5}$ crosses $x-$ axis at $\pm V_{odL}$ and with $y-$ axis at G_{L-0}.

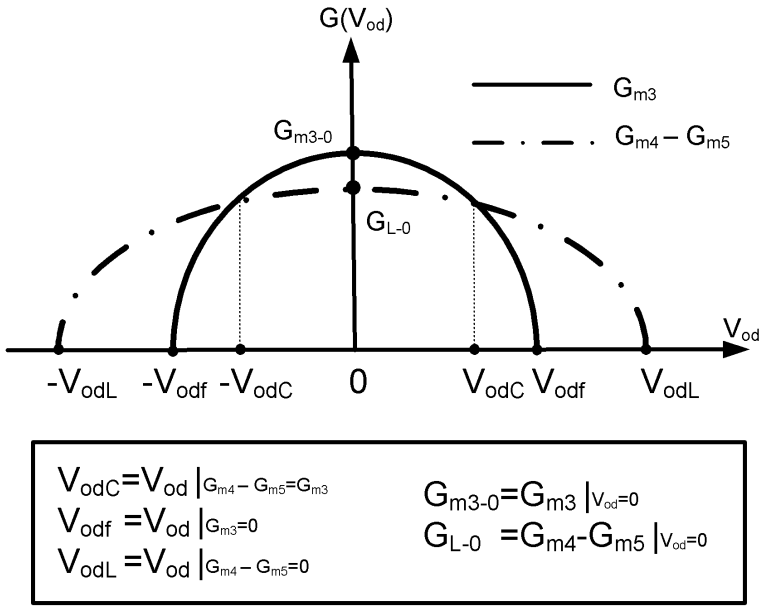

(a)

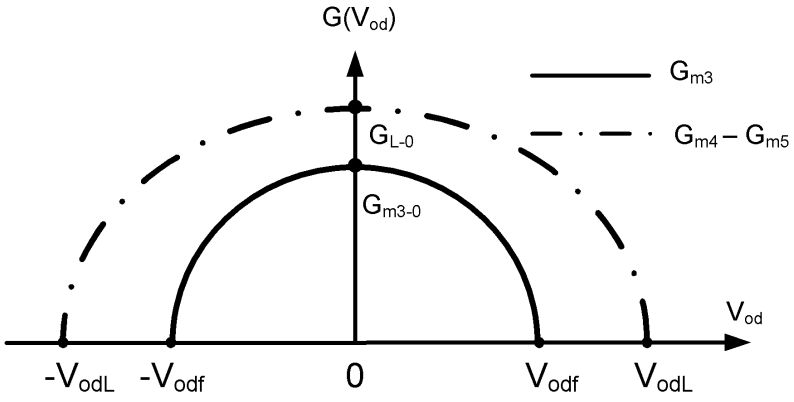

(b)

Figure 5.16: Differential transconductance curves G_{m3} and $G_{m4} - Gm5$ with output voltage change.(a)with cross nodes at $\pm V_{odC}$ (b)without cross nodes

- G_{m3} crosses $x-$ axis at $\pm V_{odf}$ and with $y-$axit at G_{m3-0}.
- The two curves have cross nodes at $\pm V_{odC}$.

When

$$-V_{odC} < V_{od} < V_{odC} \tag{5.35}$$

$$G_{m3} > G_{m4} - G_{m5} \tag{5.36}$$

turning on the positive feedback.Detailed calculation for the transconductance is given as follow:

$$I_{d3}^{+} = \frac{1}{2}k_3(V_{SG3} - |V_{thp}| + \frac{1}{2}V_{od})^2 \tag{5.37}$$

$$I_{d3}^{-} = \frac{1}{2}k_3(V_{SG3} - |V_{thp}| - \frac{1}{2}V_{od})^2 \tag{5.38}$$

The sum of the two feedback current should be constant:

$$I_{d3}^{+} + I_{d3}^{-} = I_{b2} \tag{5.39}$$

where I_{b2} is the bias current for M_3. The solution is

$$G_{m3} = \frac{I_{d3}^{+} - I_{d3}^{-}}{V_o^{+} - V_o^{+}} = k_3\sqrt{I_{b2}/k_3 - V_{od}^2/4} \tag{5.40}$$

while $G_{m4} - G_{m5}$ cam be calculated in the similar way:

$$G_{m4} - G_{m5} = (k_4 - k_5)\sqrt{\frac{I_{b1} - I_{b2}}{k_4 - k_5} - V_{od}^2/4} \tag{5.41}$$

where I_{b1} is the total bias current. Therefore the two curves cross $x-$ axis respectively at:

$$\pm V_{odf} = \pm 2\sqrt{I_{b2}/k_3} = \pm(V_{SG3} - |V_{thp}|) \tag{5.42}$$

$$\pm V_{odL} = \pm 2\sqrt{(I_{b1} - I_{b2})/(k_4 + k_5} = \pm(V_{SG4,5} - |V_{thp}|) \tag{5.43}$$

Due to the voltage drop on current source I_{b2}, V_{SG3} is always smaller than $V_{SG4,5}$, therefore V_{odf} is always smaller than V_{odL}. While the two curves also cross the

$y-$axis respectively at:

$$G_{m3-0} = k_3\sqrt{I_{b2}/k_3} = k_3(V_{SG3} - |V_{thp}|) \quad (5.44)$$

$$G_{L-0} = (k_4 - k_5)\sqrt{(I_{b1} - I_{b2})/(k_4 + k_5)} \quad (5.45)$$

$$= (k_4 - k_5)(V_{SG4,5} - |V_{thp}|) \quad (5.46)$$

when $G_{m3-0} \geq G_{L-0}$, the two curves G_{m3} and $G_{m4} - G_{m5}$ are able to cross each other and to turn on the positive feedback. Otherwise, when $G_{m3-0} < G_{L-0}$ which means curve $G_{m4} - G_{m5}$ will be always above curve G_{m3}, the positive feedback will never happen as shown in Fig.(5.16(b)).

As a result, the criterion for the circuit design should be able to ensure that:

$$k_3\sqrt{I_{b2}/k_3} > (k_4 - k_5)\sqrt{(I_{b1} - I_{b2})/(k_4 + k_5)} \quad (5.47)$$

The solution for cross points are:

$$V_{od} = \pm V_{odC} = \pm 2\sqrt{\frac{k_3 I_{b2} - (k_4 - k_5)^2(I_{b1} - I_{b2})/(k_4 + k_5)}{k_3^2 - (k_4 - k_5)^2}} \quad (5.48)$$

5.5.3 Derive Hysteresis $\pm V_{inC}$

When the differential output passes $\pm V_{odC}$ and enters the positive feedback region, the corresponding differential input voltage, names as $\pm V_{inC}$ is the hysteresis threshold. In order to derive $\pm V_{inC}$, the transfer function could be rewritten in its differential format as:

$$(G_{m4} - G_{m5} - G_{m3})dV_{od} = G_{m1}dV_{in} \quad (5.49)$$

$\pm V_{inC}$ then can be solved from the integral equation:

$$\int_{V_{odC}}^{V_{odL}} (G_{m4} - G_{m5} - G_{m3})dV_{od} = \int_0^{V_{inC}} G_{m1}dV_{in} \quad (5.50)$$

W_{M_1}	W_{M_2}	W_{M_3}	W_{M_4}	W_{M_5}
40 μm	40 μm	4 μm	3 μm	5 μm
V_b	I_{b1}	I_{b2}	I_{total}	Power
1.25 V	1 mA	75 μA	2.5 mA	4.5 mW

Table 5.1: Parameters of the comparator circuit in Fig.(5.14)

where in the similar as calculate G_{m3} and $G_{m4} - G_{m5}$:

$$G_{m1} = k_1\sqrt{I_{b1}/k_1 - V_{in}^2/4} \tag{5.51}$$

Therefore, the threshold $\pm V_{inC}$ then equals to:

$$\begin{aligned} & 2I_{b1}\arcsin\frac{V_{inC}}{2\sqrt{I_{b1}/k_1}} + \frac{1}{4}V_{inC}\sqrt{I_{b1}k_1(1-\frac{V_{inC}^2}{4I_{b1}/k_1})} \\ = \; & 2I_{b2}\arcsin\frac{V_{odC}}{2\sqrt{I_{b2}/k_3}} + \frac{1}{4}V_{odC}\sqrt{I_{b2}k_3(1-\frac{V_{odC}^2}{4I_{b2}/k_3})} \\ - \; & [(I_{b1}-I_{b2})(k_4-k_5)/(k_4+k_5)\arcsin\frac{V_{odC}}{2\sqrt{(I_{b1}-I_{b2})/(k_4+k_5)}} \\ + \; & \frac{1}{4}V_{odC}\sqrt{\frac{(I_{b1}-I_{b2})(k_4-k_5)^2}{k_4+k_5}(1-\frac{V_{odC}^2}{4(I_{b1}-I_{b2})/(k_4+k_5)})}] \end{aligned} \tag{5.52}$$

The analytical equation is complicated therefore, the precise design has to resort to the simulation software. The lengths of all the transistors are $260nm$ while the widths of the transistors, the bias current and comparator total power consumption are listed in Table.(5.1).

5.5.4 Latch

In order to stabilize the output signal, the comparator is followed by a latch circuit, which is capable of temporary storage of the output for use at a later time in the operation. Fig.(5.17)shows the commonly used latch circuit with cross coupling two NAND gates. $V_{oC\pm}$ and $V_{oL\pm}$ represent the output of comparator (also the input of latch circuit) and the output of the latch circuit. The cross coupling constructs the positive loop, and brings the memory into the circuit.

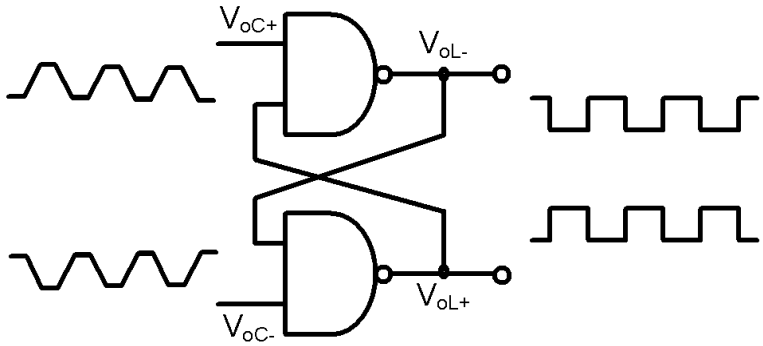

Figure 5.17: Latch circuit with cross coupling two NAND gates.

It means the output signal is no longer only dependent on the input but also dependent on the output of the last state. Besides, when the gain of the NAND gate is larger than unity, the positive loop also contributes a faster rising/falling speed at the edge of digital signal.

Fig.(5.18) shows the CMOS implementation of the latch circuit with cross coupling two NAND gates in Fig.(5.17). The width of the transistors are labeled aside. In order to minimize the power consumption and maximize the speed, all the transistors are using small size. The lengths are all $260nm$, and widths are all $1\mu m$ except the two $p-$MOS determining the gain of latch input.They are using slightly larger widths of $3\mu m$ to ensure the overall gain of each $NAND$ gate is more than unity. Even Larger value of the dimension will decrease the speed since larger capacitor of the transistor are introduced. Fig.(5.19) shows the time transient differential output voltage after the four stages amplifier $V_{oA+}-V_{oA-}$ and afterward through the comparator and latch $V_{oL+}-V_{oL-}$, under the condition that parallel capacitor of MEMS resonator is totally compensated.As can be calculated from the figure,the over all phase shift of comparator and latch in total is 30°

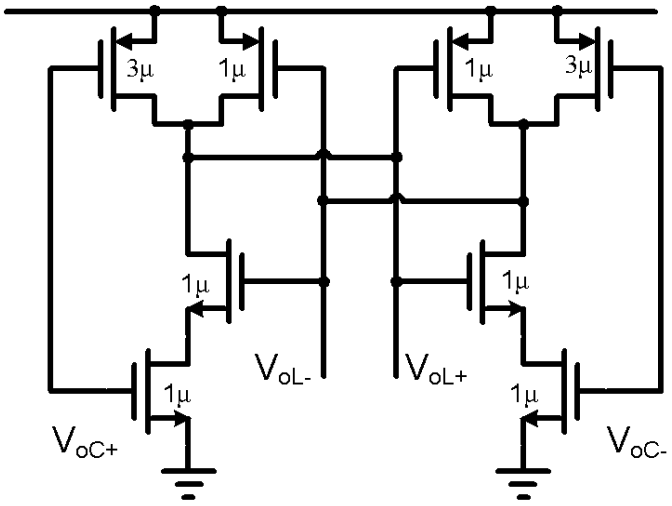

Figure 5.18: CMOS implementation of latch circuit with cross coupling two NAND gates.

which is within our estimation.

5.6 Initial Control

The oscillation close loop can achieve by simply connecting the negative output of latch to the input of MEMS resonator and the compensation capacitor array. The positive output node of latch can be the measurement port, therefore, the oscillator circuit is separated from the measurement load. However,normally an oscillator circuit requires an initial input as a start up. Fig.(5.20) shows the initial control of the oscillator. When $CLK1$ is on, the initial sinusoidal excitation is applied on the MEMS resonator, while the output of latch is left open. After a short while, $CLK1$ is off and $CLK2$ is on simultaneously, which means the initial excitation is switched off and the close loop is linked. $CLK3$ is implemented to control the on and off of the loop to perform the pulse excitation mode.

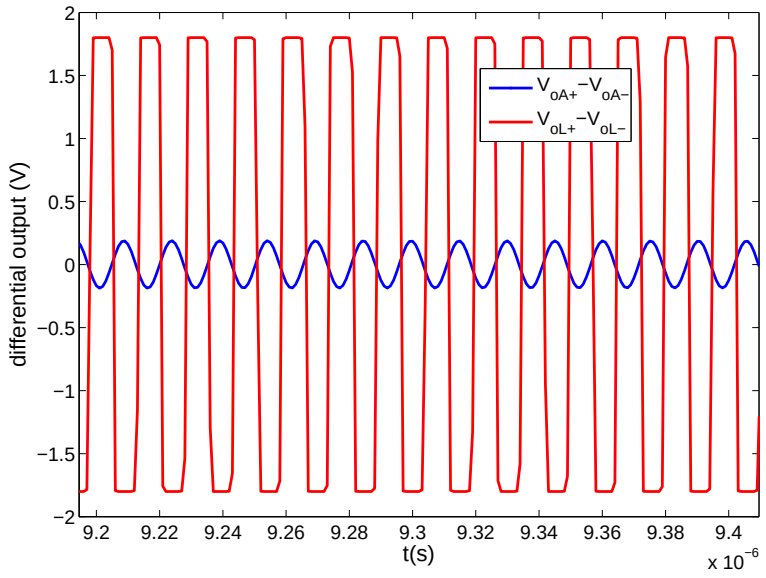

Figure 5.19: Time transient differential output voltage after the four stages amplifier $V_{oA+} - V_{oA-}$ and afterward through the comparator and latch $V_{oL+} - V_{oL-}$, under the condition that parallel capacitor of MEMS resonator is totally compensated.

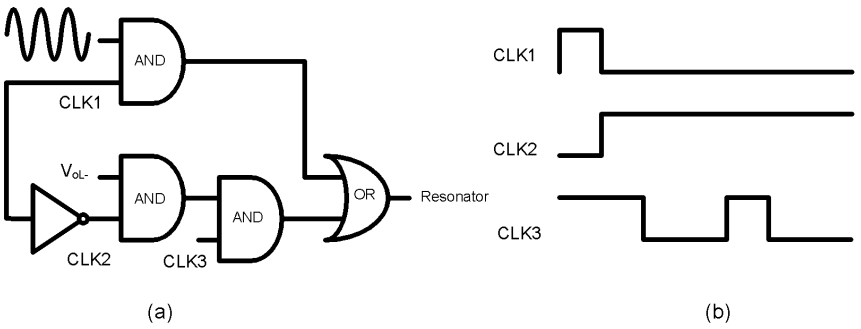

Figure 5.20: Initial excitation control with AND , INV and OR gates.

5.7 Simulink Verification

Fig.(5.21) demonstrates the simulink behavior model of the whole oscillator loop. The black area represents the initial control with a initial rectangular excitation and a switch between initial excitation and the close loop. The blue area represent the real device model in which the C_p is gain of the parallel capacitor remaining in the system after compensation:

$$K_{C_p} = C_p/C_{pad} \tag{5.53}$$

transfer function MEMS is the model of the pure motional part:

$$\begin{aligned} H(s)_{MEMS} &= \frac{1/sC_{pad}}{R_x + 1/sC_x + sL_x + 1/sC_{pad}} \\ &= \frac{C_{pad}}{s^2 L_x C_x C_{pad} + sR_x C_x C_{pad} + C_x C_{pad}} \end{aligned} \tag{5.54}$$

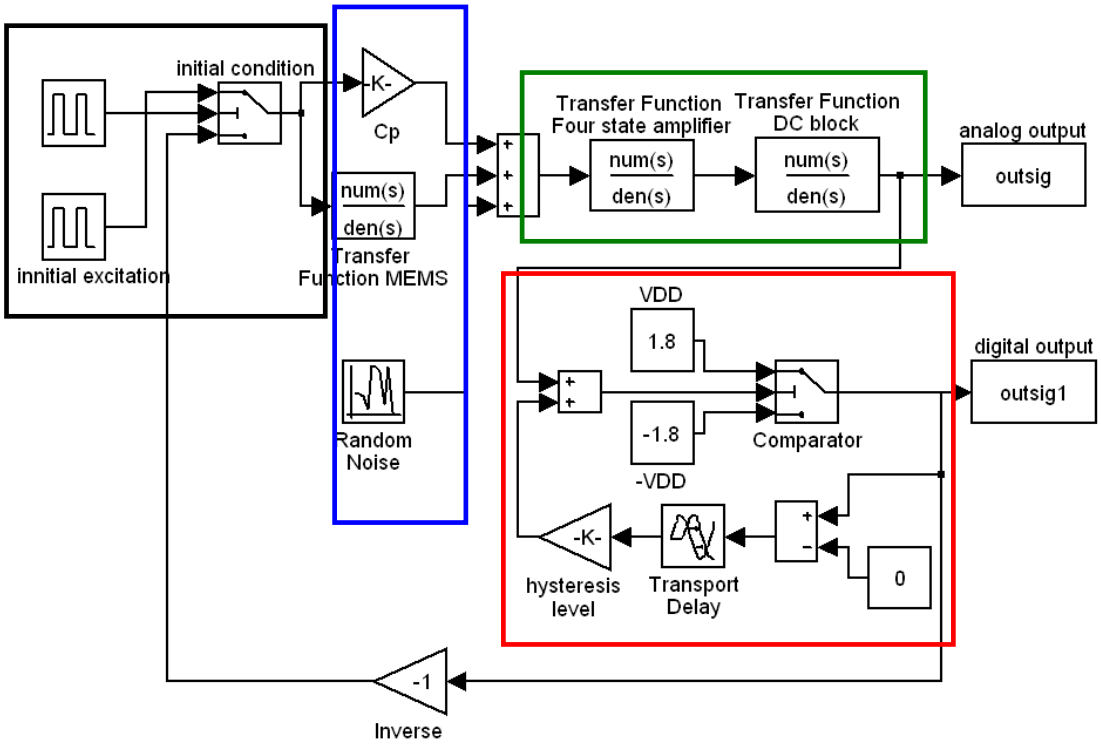

Figure 5.21: The behavior model with simulink for oscillator circuitry including the initial control (black), the MEMS device model (blue), the amplifier model (green) and the comparator (red). The analog output from the amplifier and the digital output from the comparator are indicated.

and the other block simulates the random noise of the resonator device.The green area represents the transfer function of the four-stage amplifier and the capacitive DC block in between every two stages. The values of the transfer functions are from the simulation results of Cadence. The low pass amplifier cut off frequency is $f_1 = 577MHz$ while the high pass block cut off frequency is $f_2 = 3kHz$. Both of the two frequencies are far away from the central frequency $f_0 = 66MHz$, therefore their influences on phase change are very trivial. The red area represents the model of comparator. The transport delay is to save the comparator previous output for comparison usage of current state. It is set to be a extremely short time (for example 1 ns). The hysteresis level is set by the hysteresis gain block:

$$K_{hysteresis} = V_{edge}/VDD \tag{5.55}$$

where V_{edge} is the voltage where the positive feedback starts.

Fig.(5.22) shows simulated output response when the parallel capacitor is totally compensated. Fig.(5.22(a)) shows the analog output after the amplifier for pure motional response, while Fig.(5.22(b)) is the analog output including random noise. The digital outputs of both no noise and device noise of 1 mV corresponding to 40 percent of the signal in Fig.(5.22(c)). The two digital outputs in this case overlap each other, since the comparator has a hysteresis of 30 degree which is able to tolerate up to $sin30° = 1/2$ noise/signal ratio. However in Fig.(5.22(d)) device noise is as high as 2 mV corresponding to 80 percent of the signal, the digital output has a great phase offset and in addition it appears the spark as shown with the arrow. This is because the hysteresis is not big enough to illuminate the error as stated in Fig.(5.12). Noise of the devices mainly come from the thermal noise, variation of DC supply and so on. The noise value $1mV$ is beyond the up limit of the device under room temperature and normal pressure, therefore the oscillator circuitry is reliable in this case.

When the parallel capacitor is not totally compensated, instead, there is a remaining parallel capacitor. Fig.(5.23) shows the analog (a) and digital (b) output signal for different remaining parallel capacitor 0 fF, 1 fF and 5 fF. As we can see, when the remaining parallel capacitor increases to 1 fF, some deformation appears upon the motional output due to the parallel capacitor charge

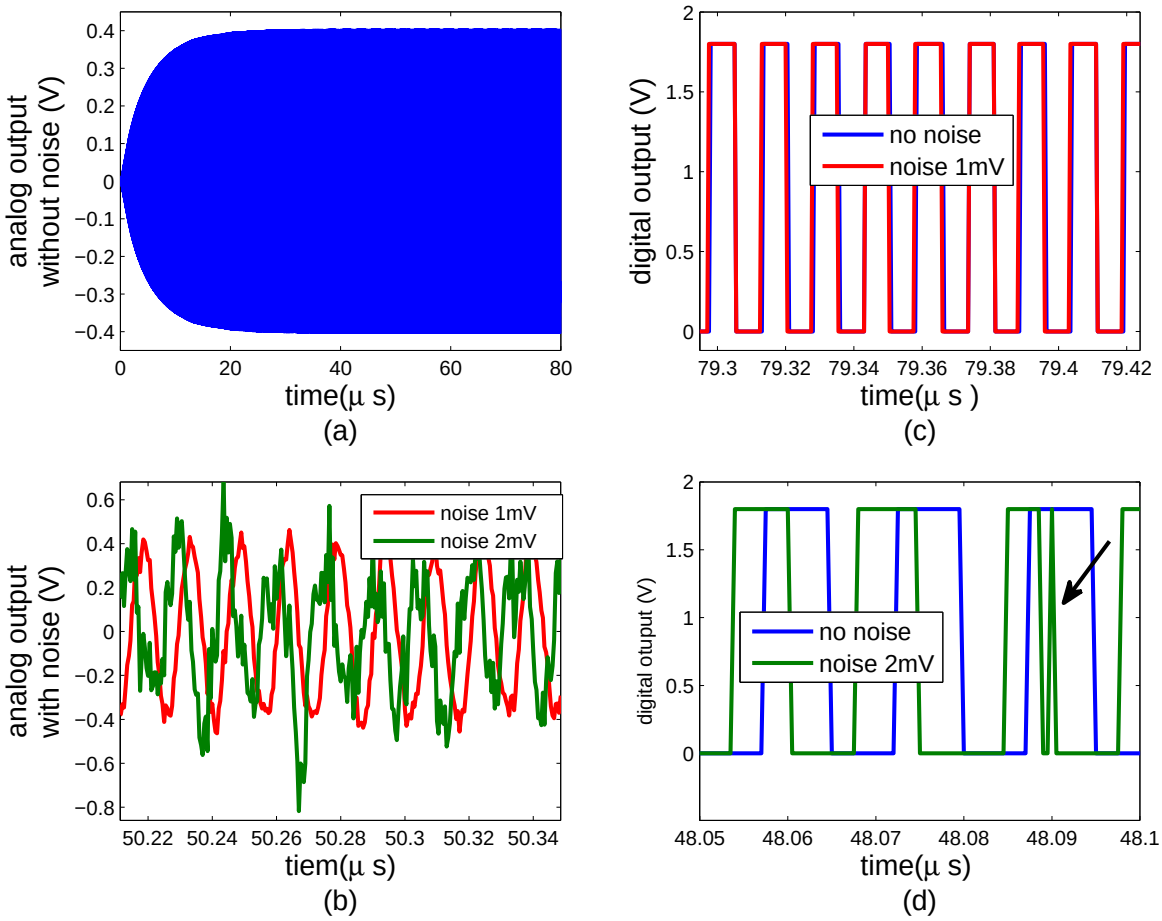

Figure 5.22: Simulated time transient voltage of the simulink behavior model with parallel capacitor total compensated ($K_{C_p} = 0$). The initial excitation lasts for 1 μs and afterward the loop is closed and starts oscillating. (a) analog output without noise (b) analog output with noise (c) digital outputs with noise less than 50 percent (d) digital outputs with noise larger than 50 percent.

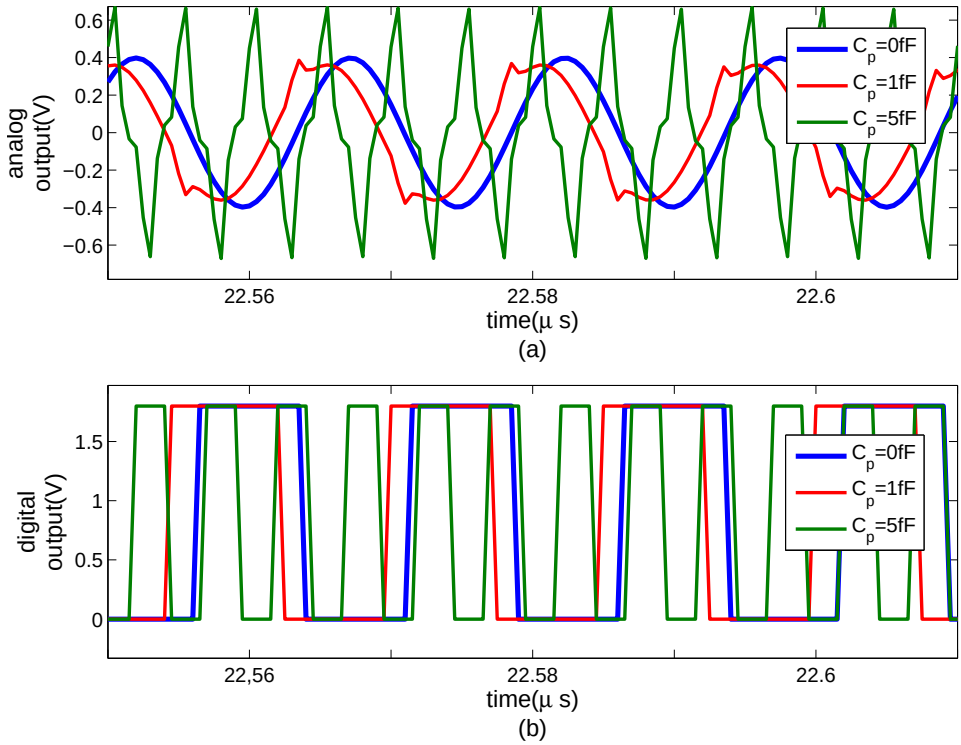

Figure 5.23: Simulated time transient voltage of the simulink behavior model with parallel capacitor compensated at different level(for remaining C_p equals to 0 fF, 1 fF and 5 fF respectively). (a) The analog output and (b) digital output output for different remaining parallel capacitor.

and discharge. At this time, this influence is not big enough to alter the resonant frequency. The small spark at the analog output can be illuminated by the hysteresis filter, therefore, the digital output only displays a phase shift but no frequency change (red line). However when the remaining capacitor continues to increase, it more and more influences the output of the disk device, changing the amplitude and phase response as stated in Chapter 3 Fig.(7) by introduce anti resonance. The amplitude and phase don't have a monotone change with frequency anymore. Therefore, the oscillator Barkhausen criterion can be met for twice while the oscillator output frequency can differ far away from the resonant frequency of MEMS resonator as shown in Fig. (5.23) green line. In our

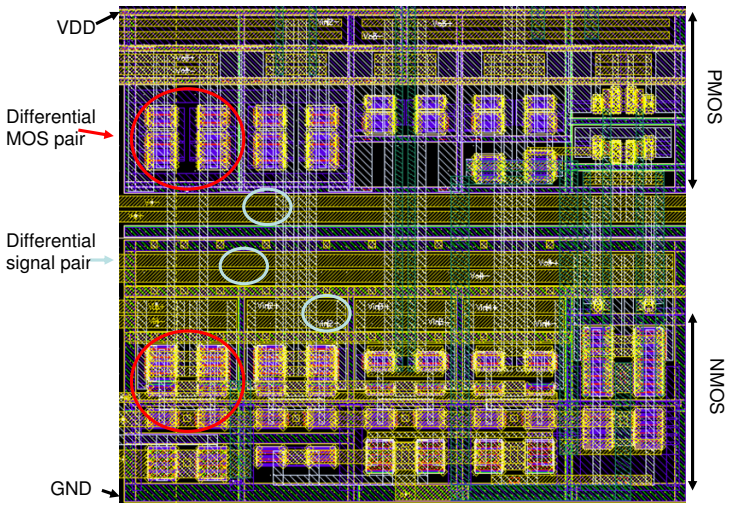

Figure 5.24: Physical layout of core circuitry of the oscillator the CMOS part including the four stage amplifier, the comparator and the DC bias circuitry.

case, according to the measurement results in Chapter 4 Fig.(5) with identical resonator pair or the theoretical prediction of the tunable capacitor at the start of this chapter, we are able to control the remaining parallel capacitor under 1 fF, thus in principle the oscillator circuitry can work properly.

5.8 Layout

Fig. (5.25) shows the physical layout of the core circuitry of oscillation mainly the CMOS part, indicating the four stage amplifier, the comparator and the bias circuitry. The most important technique necessary to highlight here is the layout of the deferential MOS pair as shown in Fig. (**??**) requires absolute symmetry so that the noise on each of the transistor is the same thus producing as low as possible noise differential output.

The whole work on oscillator circuitry is cooperated with the Shanghai Institute of Microsystem and Information Technology (SIMIT), Chinese Academy of Science (CAS). The remaining work on the whole layout and package is followed

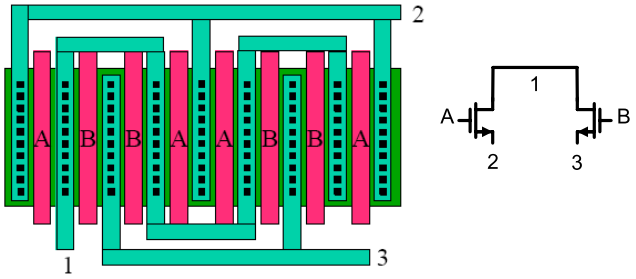

Figure 5.25: Physical layout of differential MOS pair with cross figure configuration to ensure the symmetry of the structure.

up by colleagues there. Unfortunately, during this Ph.D work, I have not enough time to tape out.

5.9 Summary

An oscillator circuitry with CMOS 0.18 μm technology is designed and simulated. It contains a tunable capacitor array for parallel capacitor compensation followed with a four stage amplifier with 45 dB gain 30° at 66 MHz and a hysteresis comparator with phase delay of 30°. The performance of the total oscillator circuitry is verified by the simulink behavior modeling where the device noise influence and remaining capacitor are included as an important consideration. The simulated results predict the proper performance of the circuit with a noise level under 1 mV and a remaining parallel capacitor under 1 fF which can be achieve in real device.

Chapter 6

Conclusion and Outlook

This Ph.D project is one part of the project 'High frequency resonators for liquid based bio/chemical diagnostics and monitoring application'. The goal of the whole project is to develop bulk mode high frequency mechanical resonators with respect to mass sensing application. To facilitate the ultimate goal of biochemical sensing, the mechanical resonator will eventually have to operate in liquid. The main object of the Ph.D project described in this thesis is to investigate the readout circuitry for this mechanical resonator.

In the introduction, the development of MEMS devices for mass sensing application was introduced. After comparing the resolution and areal resolution for different mass sensors, including QCM, FBAR, BRR, BDR and LBAR, bulk mode disk resonators supplying both a small resolution and areal resolution are the most interested device. The principle of the in plane bulk disk resonator is that any mass load on the surface of the resonator will induce a total mass change and therefore the change of the resonant frequency. The readout system is therefore required for tracing the resonant frequency. Three commonly used readout technology were discussed, the capacitive, piezoelectric and piezoresisitive readout. All the them are suitable for bulk disk resonator application. Capacitive readout was utilized in this thesis work since it has been studied for years in out group and therefore is mature.

The three types of candidate readout circuitry for capacitive readout of the resonator were also demonstrated. First is the oscillator configuration. It is simple compared to the second one the phase locked loop which however supplies

a better frequency performance. The third one is the pulse mode readout which excites the resonator for a short time and detect the free vibration after the shut down of the input. The last technique is able to measure simultaneously the resonant frequency, the Q factor and the parallel capacitor therefore is also able to characterize the medium and thus a huge benefit for liquid application in the future.

In order to understand the mechanism of the resonator and facilitate the simulation and design of readout, its equivalent mechanical and electrical models were discussed in detail. The equivalent mechanical model of the bulk resonator is a traditional mass spring damper system, where the resonant frequency, the effective mass and the spring constant can be calculated from the material properties and the geometry of the device. They are also determined by the vibration mode of the resonators such as breathing mode, wine glass mode. The equivalent electrical feedthrough capacitor, motional capacitor, inductor and resistor can be deduced from both the mechanical model and the electromechanical coupling coefficient defined by the capacitive gap.

The coupling effect depends on the different measurement setup. In the measurement theory chapter, the four main measurement configurations, the one port, two port, mixing, and the differential measurement, were discussed and thus the full electrical model of the devices were fixed. The parallel capacitor up on the mechanical motional series RLC model has an important influence on the amplitude and phase of the frequency response. Therefore, compensation techniques are analyzed accordingly.

The principles of the theory was verified by measurement. The frequency sweep measurement was first conducted on one port, tow port measurement, and furthermore was also conducted with tunable capacitor and identical resonator pair compensation. The phase gradient after compensation was largely increased and thus the frequency noise was minimized efficiently. Afterwards, the pulse mode measurement was also conducted on both LBAR and disk resonators. The measured resonant frequency, the Q factor and the parallel capacitor were consistent to the measured frequency response from frequency sweep setup and also close to the theoretical predication.Labview programmes were used to realize the real time measurement. In addition, a gas setup was built for humidity sensing

application with the resonator in pulse mode. The measured results demonstrated a fast sensing of water vapor loading. Especially, the disk resonator showed a huge frequency change with humidity thus a high sensitivity, therefore could be a perfect candidate but requires a a further investigation in the future. For example, polymer coating on the surface of the resonator is able to increase the absorption of water and thus increases the sensitivity.

Finally, in order to integrate the whole system, both the MEMS resonator device and the readout electronics, an integrated oscillator circuitry was designed and simulated as an initial start. It was using the CMOS 0.18 μm technology with a active filter tuned oscillator configuration, including a parallel capacitor compensation structure, a high gain high frequency amplifier and a comparator with Schmitt trigger. The circuitry was verified at a behavior lever with Matlab simulink. The simulated results demonstrated the feasibility of the circuitry. However, this Ph.D work didn't have enough time for tape out. The work will be followed by the cooperative partner.

Nomenclature

BAW	Bulk Acoustic Wave
BDR	Bulk Disk Resonator
BRR	Bulk Rectangular Resonator
DDA	Differential Difference Amplifier
FBAR	Thin-Film Acoustic Resonator
FDA	Fully Differential Amplifier
FEM	Finite Element Modeling
IC	Integrated Circuitry
LBAR	Longitudinal Bulk Acoustic Resonator
LNA	Low Noise Amplifier
MEMS	Micro Electro Mechanical Systems
NMES	Nano Electro Mechanical Systems
PECVD	Plasma Enhanced Chemical Vapor Deposition
PLL	Phase Locked Loop
Poly-Si	Polycrystaline Silicon
Q	Quality
QCM	Quartz Crystal Microbalance
RLC	Resistor Inductor Capacitor
SAW	Surface Acoustic Wave
SEM	Scanning Electron Microscopy
ST	Schmitt trigger
VCO	Voltage Control Oscillator

Appendix A:

Measurement Facilities

Figure 1: Photograph showing the experimental facilities at DTU Nanotech DyNEMS group.

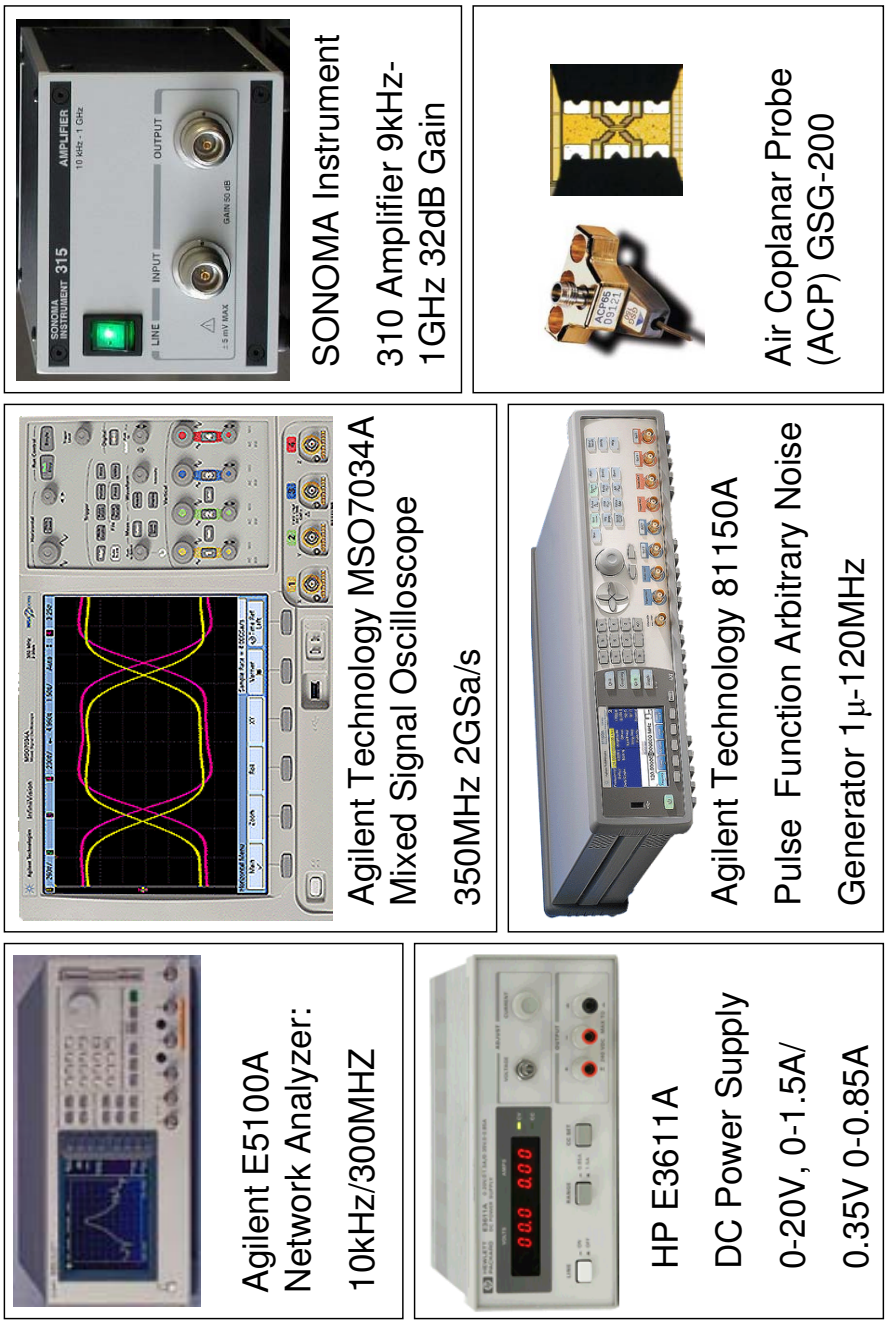

Appendix B:

Labview Data Acquisition

Figure 2: Labview programme of data acquisition, showing the function of every block.

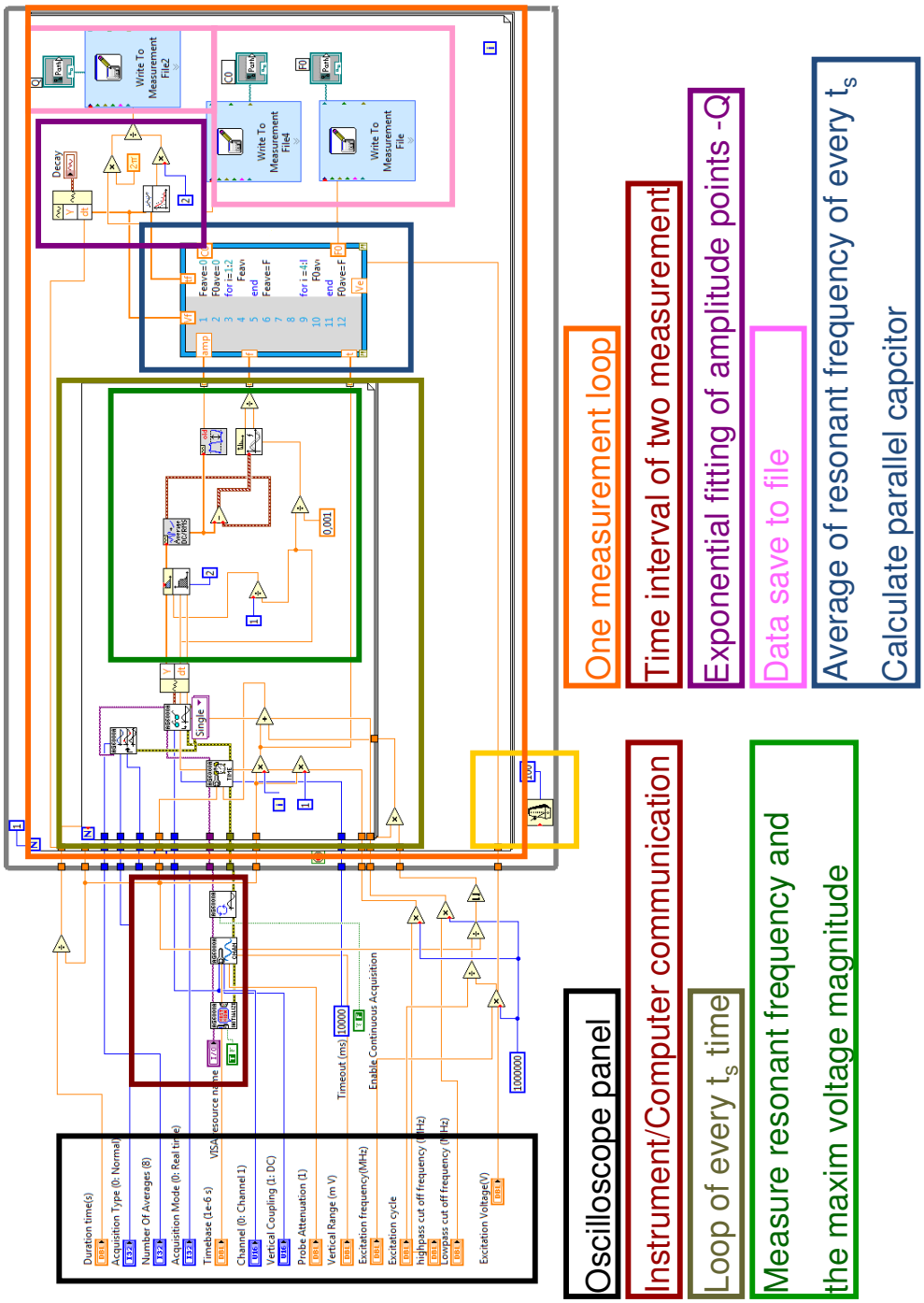

Appendix C:

List of Publications

1.M.Tang, A.Cagliani and Z.J.Davis. Pulse mode readout on MEMS bulk disk resonator based mass sensor. *Submitted to Sensors and Actuators A.*

2.L.He, M.Tang, G.Li, G.Wang and Z.J.Davis. A CMOS differential Schmitt trigger with PTAT hysteresis for precise reference oscillator in wireless sensor node. *Submitted to IEEE Transactions on Circuits and Systems.*

3.L.Yan, M.Tang, V.Krozer, V.Zhurbenko, T.Jensen, C.Jiang, T.K.Johansen. Transmission line model for coupled rectangular split ring resonators. *Submitted to Microwave and Optical Technology Letters.*

4.M.Tang, A.Cagliani, Z.J.Davis. Noise depression of parasitic capacitance for frequency detection of micromechanical bulk disk resonator. *Proceeding of the 5th IEEE International Conference on Nano/Micro Engineered and Molecular Systems (NEMS)*, 2010.

5.A.Cagliani, M.Tang and Z.J.Davis. Novel pulse actuation readout scheme for bulk disk resonator based ultrsensitive mass sensor.*Proceeding of the 9th IEEE Conference on Sensors*, 2010.

6.Z.J.Davis, M.Tang, J.H.Hales, C.Bradley, N.Jalili, A.Boisen. Au nanoparticle detection using silicon nitride micro/nano mechanical devices with integrated strain gauge readout. *Proceeding of the 3nd IEEE International Conference on Nano/Micro Engineered and Molecular Systems (NEMS)*, 2008.

References

[1] R.P.Feynman. There's plenty of room at the bottom. *Talk given at the Ammerican Physical Society at the California Institute of Technology*, 1959.

[2] K.L.Ekinci and M.L.Roukes. Nanoelectromechanical systems. *Review of Scientific Instruments*,76(6): pp.1-12,2005

[3] R.Bogue. MEMS sensors: past, present and future.*Sensor Review*, pp.7-13,2007.

[4] D.J.Bell, T.L.Lu, N.A.Fleck and S.M.Spearing. MEMS actuators and sensors:observations on their performance and selection for purpose.*Journal of Micromechanics and Microengineering*, Vol.15, No.7, 2005

[5] J.M.Stauffer and P.Salomon. Advanced MEMS accelerometers.*OnBoard Technology*. pp.48, 2005.

[6] G.M.Rebeiz. RF MEMS switches:status of the technology. *12th International Conference on solid State Sensors, Acutators and Microsystems*, pp.1726-1729, 2003.

[7] M.M.Elrick, J.L.Walgren, M.D.Mitchell and D.C.Thompson. Proteomics:Recent applications ans new technologies. *Basic and clinical Pharmacology and Toxicolog* Vol.98 pp.432-441, 2006

[8] J.Fritz, M.K.Baller, H.P.Lang,H.Rothuizen, P.Vettiger, E.Meyer, H.J.Guntherodt, C.Gerber and J.K.Gimzewski. Translating biomolecular recognition into nanomechanics. *Science*, 288 pp.316-318, 2000.

[9] P.S.Saggoner and H.G.Craighead. Micro- and nanomechanical sensors for environmental, chemical, and biological detection. *Lab on a chip* 7, pp.1238-1255, 2007.

[10] Z.J.Davis, W.Svendsen and A.Boisen. Design, fabrication and testing of a novel MEMS resonator for mass sensing applications. *Microelectron Engineering*,84 pp.1601-1605, 2007.

[11] G.Sauerbrey. Use of quart vibrator for weighing thin layers and as a microbalance. *Seitschrift furPhysik*,150(2): pp.206-222, 1959.

[12] S.S.Narine and A.J.Slavin. Use of the quartz crystal microbalance to measure the mass of submonolayer deposits: Measuring the stoichiometry of surface oxides. *Journal of Vacuum Scientce and Technology A(Vacuum, Surfaces and Films)*, 16(3): pp.1857-1862, 1998.

[13] A.Dolatshahi-Pirouz, K.Rechendorff, M.B.Hovgaard, M.Foss, J.Chevallier and F.Besenbacher. Bovine serum albumin absorption on nano-rough platinum surfaces studied by QCM-D. *Colloids and Surfaces B: Biointerfaces*, 66(1): pp.53-59, 2008.

[14] J.J.Royer. Rectangular AT-cut resonators. *27th Annual Symposium on Frequency Control*, pp.30-34, 1973.

[15] V.M.Mecea. Is quartz crystal microbalance really a mass sensor? *Sensors and Actuators: A.Physical*,128(2): pp.270-277, 2006.

[16] C.K.O'Sullivan and G.G.Guilbaut. Commercial quartz crystal microbalances-theory and applications. *Biosensors and Bioelectronics*, vol.14, pp.663-670,1996.

[17] H.Campanella, A.Uranga, A.Romano-Rodrigues, J.Montserrat, G.Abadal, N.Barniol, and J.Esteve. Localized-mass detection based on thin-film bulk acoustic wave resonators (FBARs), area and mass location aspects. *Sensors and Actuators A: Physical*, 142(1): pp.322-328, 2007.

[18] J.Weber, W.M.Albers, J.Tuppurainen, M.Link, R.Gabl, W.Wersing and M.Schreiter. Shere mode FBARs as highly sensitive liquid biosensors. *Sensors and Actuators:A.Physics*, 128: pp.84-88, 2006.

[19] S.Dohn, R.Sandberg, W.Svendsen and A.Boisen. Enhanced functionality of cantilever based mass sensors using higher modes. *Applied Physics Letter*, 86, 233501, 2005.

[20] Z.Davis and A.Boisen. Aluminum nanocantilevers for high sensitivity mass sensors. *Applied Physics Letters*, 87, 013102, 2005.

[21] M.Calleja and J.Tamayo. Low noise polymeric nanomechanical biosensors. *applied Physics Letters*, 88, 113901, 2006.

[22] L.Mo, H.X. Tang and M.L.Roukes. Ultra-sensitive NEMS-based cantilevers for sensing, scanned probe and very high frequency application. *Nature Nanotechnology*, 2(2): pp.114-120, 2007.

[23] B.Illic, H.C.craighead, S.Krylov, W.Senaratne, C.Ober and P.Neuzil. Attogram detection using nanoelectromechanical oscillators. *Journal of Applied Physics*, Vol. 95, pp. 3694-3703, 2004.

[24] T.P.Burg, M Godin, S.M.Knudsen, W.Shen, G. Carlson, J.S.Foster, K.Babcock and S.R.Manalis. Weighing of biomolecules, single cells and single nanoparticles in fluid. *Nature*, 446(7139): pp.1066-1069, 2007.

[25] J.Verd, A.Uranga, G.Abadal, J.L.Teva, F.Torres, J.L.Lopez, E.P.Murano, J.Esteve and N.Barniol. Monolithis CMOS MEMS oscillator circuit for sensing in the attogram range. *IEEE Electron Device Letters*, 29(2): pp.146-148, 2008

[26] Y.T.Yang, C.Callegari, X.L.Feng, K.L.Ekinci and M.L.Roukes Zeptogram-Scale Nanomechanical Mass Sensing. *Nanoletters*, Vol. 6, No. 4, 2006.

[27] B.Ilic, D.Czaplewski, M.Zalalutdinov, H.G.Craighead, P.Neuzil, C.Campagnolo and C.Batt. Single cell detection with micromechanical oscillators. *Journal of Vaccum Scientce and Technology B*, 19, 2825,2001.

[28] K.Park and R.Bashir. MEMS-based resonant sensor with uniform mass sensitivity. *The 15th International Conference on Solid-State Sensors, Actuators and Microsystems*, pp.1956-1958, 2009.

[29] A. Cagliani and Z.J. Davis, Bulk Disk Resonator Based Ultrasensitive Mass Sensor. *IEEE Sensors*, 1-3 pp.1254-1257, 2009.

[30] J.E.-Y. Lee, B. Bahreyni, Y. Zhu and A.A.Seshia. Ultrasensitive mass balance based on a bulk acoustic mode silicon crystal silicon resonator. *Applied Physics Letters*, 91 234103, 2007.

[31] J.H. Hales, J. Teva, A. Boisen and Z.J. Davis, Longitudinal bulk acoustic mass sensor, *Applled Physics Letters*, 95 033506, 2009.

[32] J.R.Clark, W.T.Hsu and C.T.C.Nguyen. High Q VHF micromechanical contour mode disk resonators. *Technical Digest - International Electron Devices Meeting*, pp.493-496, 2000.

[33] J.Wang, Z.Ren and C.T.C.Nguyen. 1.156-GHz self-aligned vibrating micromechanical disk resonator. *IEEE Transactions on Ultrasonics, Ferroelectrics and Frequency Control*, 51(12): pp.1607-1628, 2004.

[34] M.A.Abdelmoneum, M.U.Demircim and C.T.C.Nguyen. Stemless wine galss mode disk micromechanical resonators. *The 6th Annual International Conference on Micro Electro Mechanical Systems*, pp.698-701, 2003.

[35] J.H.Hales. High frequency resonators for liquid based Bio/chemical diagnostics and monitoring applications. *PhD thesis, Technical University of Denmark, Department of Nanotechnology*,2009.

[36] P.A.Rasmussen, O.Hansen and A.Boisen. Cantilever surface stress sensors with single crystalline silicon piezoresisitors. *Applied Physics Letters*, 86, 203502, 2005.

[37] J.T.M.Van Beek, P.G.Steeneken and B.Giesbers. A 10 MHz piezoresisitive MEMS resonator with high Q. *Proceedings of the IEEE Frequency Control Symposium and Exposition*, Vol.1 2 pp. 475-480, 2006.

[38] D.Weinstein and S.A.Bhave. Piezoresistive sensing of a dielectrically actuated silicon bar resonator. *Solid State Sensors, Actuators and Microsystems Workshop*, pp.368-371, 2008

[39] A.T.-H.Lin, J.E-Y.Lee, J.Yan and A.A.Seshia. Methods for enhanced electrical transducation and characterization of micromechanical resonators. *Sensors and Actuators A: Physical*, pp. 263-272, 2010.

[40] A.Johansson. PhD thesis. SU-8 cantilever sensor with integrated readout.*DTU Nanotech*, 2006.

[41] J.Lu, T. Suga, Y.zhang, T.Itoh,R.Maeda and T.Mihara. Micromachined silicon disk resonator transduced by piezoelectric lead zirconate titanate thin films.*Japanese Journal of Applied Physics*, 49 0GH17, 2010.

[42] K.L.Ekini, Y.T.Yang and M.L.Roukes. Ultimate limits to inertial mass sensing based upon nanoelectromechanical systems. *Journal of Applied Physics*, Vol.95 No.5, 2004.

[43] A.S.Sedra and K.C.Smith. Microelectronic Circuit. *oxford university press*, 1998

[44] W.Hsu. Recent progress in silicon MEMS oscillators. *The 40th Annual Precise Time and Time Interval (PTTI) Meeting*, 2008.

[45] X.L.Feng, C.J.White, A.Hajimiri and M.L.Roukes. A sel-sustaining ultrahigh frequency nanoelectromechanical oscillator. *Nature Nanotechnology*, Vol 3, pp.342-346, 2008.

[46] C.T.-C. Nguyen and R.T.Howe. An integrated CMOS micromechanical resonator high Q oscilaltor. *IEEE Journal of Solid Circuits*, Vol. 34, No. 4, 1999

[47] S.Lee, M.U.Demirci and C.T.-C.Nguyen. A 10-MHz micromechanical resonator pierce reference oscilaltor for communications. *The 11th International Conference on Solid State Sensors and Actuators*, pp.1094-1097, 2001.

[48] Y.Lin, S.Lee, S.Li, Y.Xie, Z.Ren, C.T.-C Nguyen. Series resonant VHF micromechanical resoantor reference oscillators. *IEEE Journal of Solid State Circuits*, Cil.39, No. 12, 2004

[49] Y.Lin, S.Li, Z.Ren and C.T.-C. Nguyen. Low phase noise array composite micromechanical wine glass disk oscillator. *Technical Digest, IEEE International Electron Devices Meeting*, pp.287-290, 2005

[50] S.Lee and C.T.-C.Nguyen. Influence of automatic level control on micromechanical resonator oscillator phase noise. *Proceedings of IEEE International Frequency Control Symposium*, pp.341-349, 2003

[51] D.A.Johns and K.Martin. Analog integrated circuit design. *John Wiley and Sons.Inc.*, 1997.

[52] M. Rodahl and B. Kasemo. A Simple Setup to Simultaneously Measure the Resonant Frequency and the Absolute Dissipation Factor of a Quarts Crystal Microbalanc. *Review of Scientfic Instrumation*, 67 pp.3238-3241, 1996.

[53] G. Wang, M. Rodahl, M. Edvardsson, S. Svedhem, G. Ohlsson, F. Hook and B. Kasemo. A Combined Reflectometry and Quartz Crystal Microbalance with Dissipation Setup for Surface Interaction Studies. *Review of Scientific Instrumentation*, 79 075107, 2008.

[54] W.-T Hsu, J.R.Clark and C.T.-C Nguyen. A sub-micron capacitive gap process for multiple-metal-electrode lateral micromechanical resonators. *Technical digest of the 14th IEEE international MEMS Conference* pp.349-352, 2001.

[55] J.Teva. PhD thesis 'Integration of CMOS-MEMS resonators for radiofrequency applications in the VHF and UHF bands'. Universitat Autonoma de Barcelona, 2007

[56] T.Mattila, J.Kiihanaki, T.Lamminmaaki, O. Jaakkola, P.Rantakari, A.Oja, H.Steppa, H.Kattelus, and Tittonen. A 12MHz micromechanical bulk acoustic mode oscillator. *Sensors and Actuators A: Physical*, Vol.101, pp.1-9, 2002.

[57] M.R.Spiegel. Schaum's Mathematical Handbook of Formulas and Tables. *McGraw-Hill Edition*, 1999.

[58] M.Onoe. Contour vibrations of isotropic circular plates. *Journal of Acoustical Society of America*, Vol.28, No.6 pp.1158-11662, 1954.

[59] J.E.-Y.Lee and A.A.Seshia. 5.4MHz single crystal silicon wine glass mode disk resonator with quality factor of 2 million. *Sensors and Actuators A: Physical*,156 pp.28-35, 2009.

[60] F.D.Bannon III, J.R.Clark and C.T.-C. Nguyen. High-Q HF microelectromechanical filters. *IEEE Journal of Solid-State Circuits*, Vol.35, No.4, pp.512-526, 2000.

[61] W.W.JR, S.P.Timoshenko and D.H.Young. Vibration problems in engineering. *John Wiley and Sons*, 1990.

[62] Daniel Zwillinger. Handbook of Different Equations. *Academic Press*, 1989.

[63] J. Cross. Electrostatics: Principles, problems and applications. *Bristol Hilger*, 1987.

[64] A.-C. Wong, H.Ding, and C.T.-C Nguyen. Micromechanical mixer and Filters. *Technical Digest, IEEE International Electro Devices Meeting*, pp.471-474, 1998.

[65] J.Arcamone, E.Colinet, A.Niel and E.Ollier. Efficient capacitive transduction of high frequency micromechanical resonators by intrinsic cancelation of parasitic feedthrough capacitances. *Applied Physics Letters*, 97 043505, 2010.

[66] M.Tang, A.Cagliani, M.Escouflaire, S.Mouisel, Z.J.Davis. Noise depression of parasitic capacitance for frequency detection of micromechanical bulk disk resonator. *The 5th annual IEEE NEMS International conference on NANO/Micro Engineered and Molecular Systems*, pp. 726-729, 2010

[67] B.P.Otis and J.M.Rabaey. A $300-\mu$W $1.9-GHz$ $CMOS$ oscillator utilizing micromachined resonators. *IEEE Journal of Solid State Circuits*, Vol.38, No.7, 2003.

[68] J.E-Y Lee, Y Zhu and A.A.Seshia. A bulk acoustic mode single crystal silicon microresonator with a high quality factor. *Journal of Micromechanics and Microengineering*, 064001, 2008.

[69] R.Hidayat, J.Dejhan, P.Moungnoul, and Y.Miyanaga. A $0.18\mu m$ $CMOS$ Gaussian Monocycle pulse circuit design for UWB. *Asia Pacific Conference on Circuits and systems IEEE*, 2006.

[70] J.G.Proakis and D.G.Manolakis. Digital signal processing:principle, algorithms and applications. *Pearson*, 2007

[71] J E-Y Lee,Y Zhu and A A Seshia. A Bulk Acoustic Mode Single-crystal Silicon Microresonator with a High-quality Factor. *Journal of Micromechanicals and Microengineering*, 18 064001, 2008.

[72] Z.J. Davis, G. Abadal, O. Kuhn, O. Hansen, F. Grey and A. Boisen. Fabrication and Characterization of Nanoresonating Devices for Mass Detection. *Journal of Vacumm Science and Technology B*, 18 pp.612-616, 2000.

[73] C.T.-C. Nguyen and R.T. Howe. An Integrated CMOS Micromechanical Resonator High-Q Oscillator. *IEEE Journal of Solid-State Circuits* 34 pp.440-455, 1999.

[74] D.M.Pozar. Microwave engineering. *John Wiley*, 2005

[75] P.Andreani, A.Bonfanti, L.Romano and C.Samori. Analysis and Design of a 1.8-GHz CMOS LC quadrature VCO. *IEEE Journal of Solid State Circuits*, Vol.37, No.12, 2002.

[76] B.L.Dokic. CMOS Schmitt trigger with wide hysteresis.*Journal of Microelectronics*, Vol. 15, No.2, pp.24-29, 1984

[77] C.Zhang, A.Srivastava and P.Ajmera. Low voltage CMOS Schmitt trigger circuits. *Electronics Letter*, Vol. 39, no.24, pp.1696-1698, 2003

[78] J.Kiang and C.-T.Chuang. Restoration of controllable hysteresis in partially depleted SOI CMOS Schmitt trigger circuits. *IEEE Transaction of Circuits Systems II*, Vol.51, No.7, pp. 349-353, 2004.

[79] S.-L.Chen abd M.-D.Ker. A new Schimitt trigger circuit in a 0.13-μs 1/2.5-V CMOS process to receive 3.3-V input signals. *IEEE Transcation of Circuits Systems II*,vol.52, no.7, pp.361-365, 2005.

[80] D. Allstot. A precision variable supply CMOS comparator. *IEEE Journal of Solid State Circuits*, vol.17 No. 6, pp.1080-1087,1982.

[81] F.Yuan. A high speed differential CMOS Schmitt trigger with regenerative current feedback and adjustable hysteresis. *Analog Inegrated Circuit and Signal Process*, Vol.63, pp. 121-127, 2010.